Design of optical fibres with advanced modal control properties

Muliar, Olena

Publication date:
2018

Document Version
Publisher's PDF, also known as Version of record

Design of optical fibres with advanced modal control properties

Olena Muliar

Department of Photonics Engineering
Technical University of Denmark

This dissertation is submitted for the degree of
Doctor of Philosophy

February 2018

Abstract

Within the last decade unique properties of higher-order modes (HOMs) have been in focus of many researchers all around the world and found application in sensing, group velocity dispersion compensation and nonlinear frequency conversion among others. Development of optical communication systems has increased interest to HOMs as independent spatial data channels for mode division multiplexing (MDM). The primary aim of this thesis is the investigation, modelling and experimental evaluation of HOMs in an optical fibre of advanced design, suitable for a MDM implementation.

In order to achieve this goal, an interferometric-based fibre characterisation technique, known as a cross-correlated (C^2) imaging, was explored. An alternative modal reconstruction approach by 2D Fourier transform was presented, that allowed to extract intensity and phase distributions of the fibre mode from a single interferogram, acquired by a camera at a specific time delay. Aforementioned reconstruction technique was implemented for a flexible C^2 imaging, which was realised by an application of a tunable and highly flexible light source. Current configuration of the C^2 set-up gave an opportunity to investigate an influence of a spectral shape and bandwidth on a temporal resolution of the method and to form the input spectrum according to experimental requirements of the fibre design. A demonstration of the flexible C^2 imaging was performed by a characterisation of a step-index fibre (SMF28) and a distributed mode filtering (DMF) rod fibre over a broad

range of wavelengths. Results of the measurements are compared with numerical simulations revealing a good agreement. One of the method's advantages is an ability to identify all 3 operational regimes of the DMF rod fibre. For sensitivity verification of the flexible C^2 imaging the modal cutoff for a polarisation maintaining (PM) step-index fibre was estimated. A set of repeatable measurements for characterisation of LP_{11} close to the cutoff wavelength were performed. Based on a spread of the detected modal powers a standard deviation was calculated for the each set of measurements, revealing sensitivity of the set-up to the highly suppressed modes. In the concluding part of the imaging techniques investigation, the C^2 approach was compared with the spatially and spectrally (S^2) resolved imaging, by measuring modal properties of a hollow core anti-resonant photonic crystal fibre, designed for high power beam delivery.

In the second part of the thesis, was presented a model of a 19-cell hollow core (HC) photonic bandgap fibre (PBGF), that possesses a low transmission loss of approximately 4dB/km within 50nm of the C-band. From a numerical simulation were determined the effective refractive indices of the fibre modes, modal losses and intermodal delays. As a result, were selected two groups of the full vectorial modes, that can compose type of modes supported by the fibre for a data transmission under a MDM scenario.

To confirm the results of simulation an experimental characterisation of the modelled 19-cell HC PBGF was conducted. A modal content evaluation within a broad wavelength range was performed by a modified S^2 technique with a spectrogram approach. Results of the experimental and numerical fibre analysis were compared. It was revealed, that in 10m of the fibre within a low loss bandwidth propagated predicted LP_{01}, LP_{11} and LP_{02} modes. A characterisation of 325m of the fibre was made by a time-of-flight technique (ToF), that confirmed results obtained for the S^2 spectrogram. The methods of OAM mode excitation were investigated

and the set-up for mode multiplexing and demultiplexing was built and tested. Obtained results demonstrated an improbability of OAM modes propagation in the 19-cell HC PBGF of 325m length.

Resumé

Indenfor de sidste 20 år har højere orden bølgetyper været i fokus for mange internationale forskere, og har fundet et vælg af anvendelser verdens rund og har fundet en masser af anvendelser, bland andet i sensing, gruppehastighedsdispersionkompensering og ikke-lineær frekvens konvertering. Udvikling af optiske kommunikation systemer har også øget interessen til en anvendelse af højere orden bølgetyper, som individuelle informationskanaler indenfor felttilstand division multipleksing (MDM). Denne ph.d.-afhandling omfatter teoretiske undersøgelser, modellering og eksperimental karakterisering af højere orden bølgetyper i optiske fiber af avanceret design, som kan anvendes i MDM.

For at opnå dette mål var en interferometrisk-baseret fiberkarakteriseringsteknik, kendt som en krydskorreleret (C^2) billedliggørelse, undersøgt. En alternativ metode til felttilstand genopbygning ved 2D Fourier transformation blev præsenteret. Denne metode giver mulighed at få intensitet- og faseprofilen af felttilstanden fra et enkelt interferogram, som er taget af et kamera ved en bestemt tidsforsinkelse. Den ovennævnte genopbygningsteknik var implementeret for en fleksibel C^2 metode, som blev realiseret ved anvendelse af frekvensjusterbar og fleksibel lyskilde. Dannet konfiguration af C^2 opstillingen gav mulighed for at undersøge indflydelse af en spektrallinje og båndbredde på en

tidslig opløsning af systemet og at danne indgangsspektret ifølge et eksperimentelt krav af fiberdesignen. Demonstrationen af den fleksible C^2 metode blev udført ved en karakterisering af en step-indeks fiber (SMF28) og en distribueret bølgetype filtrering (DMF) rod fiber over en bred vifte af bølgelængder. Resultaterne af målingerne sammenlignes med numeriske simuleringer, der viser en god overenstemmelse mellem dem. En af metodens fordele er en evne til at identificere alle 3 driftsregimer af DMF fiber. For at verificere følsomhed af den fleksible C^2 billedliggørelse blev estimeret modal cutoff for en polariseringsvedligeholdende (PM) fiber. Et sæt af målinger blev udført til at karakterisere LP_{11} tæt på cutoff bølgelængden. For hvert sæt af målinger blev der fundet en standardafvigelse, som er beregnet ud fra en spredning af de påvist felttilstandes kræfter. De målte resultater afslører følsomheden af opstillingen til de stærkt undertrykte tilstande. Til sidst blev C^2 tilgangen sammenlignet med en anden teknik, kendt som en rumligt og spektralt (S^2) opløst billedliggørelse. Begge metoder blev anvendt til at karakterisere en hulkerne anti-resonant fotonik-krystalfiber, designet til levering af høj stråle effekt.

I anden del af afhandlingen præsenteres en model af en 19-celle hulkerne (HC) fotonisk båndgab fiber (PBGF), som har et lavt transmissionstab på ca. 4 dB / km inden for 50 nm af C-båndet. Ved numerisk simulering blev de effektive brydningsindeks, tab og tidsforsinkelser for de forskellige bølgetyper fundet. Fra resultaterne af simuleringen blev der valgt to grupper af fuldvektorielle bølgetyper, der kan danne den specifik type af felttilstande, som kan understøttes af fiberen og bruges i et MDM-scenario.

For at bekræfte simuleringsresultaterne blev en eksperimentel karakterisering af den modellerede 19-celle HC PBGF udført ved hjælp en modificeret S^2 teknik i en spektrogram tilgang. Ifølge målinger blev det afsløret, at i 10m af fiberen inden for en lav transmission båndbredde udbreder 3 bølgetyper, navnlig LP_{01}, LP_{11} og LP_{02}, ligesom det var

beregnet i modellen. En karakterisering af 325m af fiberen blev lavet ved hjælp af en flyvningstid teknik (ToF), som bekræftede resultater opnået for S^2 spektrogrammet. Af hensyn til opdagelse af de forudsagte grupper af bølgetyper og på grund af en lav transmission båndbredde blev undersøgt en excitation af OAM-tilstande i fiberen. Fremgangsmåden til OAM-bøgletyper generation blev udforsket, og opstillingen for OAM-bølgetyper multipleksing og demultipleksing blev bygget og testet. Resultater viste en usandsynlighed for at OAM-bølgetyper kan udbrede sig i en 19-celle HC PBGF af 325m længde.

Acknowledgements

I would like to thank all my supervisors for an opportunity to start my PhD studying and for the help, guidance and knowledge sharing through my research during the last four years. Particularly, to Jesper Lægsgaard for his constructing suggestions, wise advises and support in pursuing my PhD degree.

I wish to thank Mario Usuga for his enormous patience and optimism during many hours in the lab and encouragement help and support during the whole my PhD and for the proof reading. I thank Mattia Michieletto for sharing his experience of modelling HC PBGF and for his bright ideas while working together in the lab. I wish to thank also to Mette Marie Johansen for support in ROD modelling and her valuable suggestions, to Jens Kristian Lyngsøe for fruitful discussions and useful advises concerning HC PBGF and to Kasper Ingerslev for sharing his knowledge of OAM modes and the S^2 imaging.

I thank all my colleges at NKT Photonics and DTU Fotonik for the help, encouragement and support during this four years full of fun and challenges. A special thank goes to Sidsel Rubner Papior and Stine Møller Israelsen for motivation and inspiration.

Lastly, I wish to thank my husband Alex and my children for their love and for being here for me all the time, especially in the hardest moments. And to my parents and sister, that despite of being separated by distance, always supported me greatly and doubtless.

Table of contents

List of figures

List of tables

Chapter 1

Introduction

It is well-known from fundamentals of optical waveguide theory, that light coupled in an optical fibre propagates within it in different transverse spatial patterns, known as fibre modes. For a long time, higher-order modes (HOMs) were considered as an undesirable effect, especially in the optical network systems, where all data was transmitted in the fundamental fibre mode. Presence of HOMs, in this case, led to degradation of the system due to the modal dispersion in a fibre. Despite of this, HOMs have attracted a great attention due to their unique properties. Applications of HOMs comprise, not exclusively, implementation for sensing [45], non-linear frequency conversion[105] and group velocity dispersion compensation[79]. Recent advancement of communication systems with implementation of erbium-doped fibre amplifiers, coherent detection and digital signal processing had increased interest to HOMs as independent data channels in mode division multiplexing (MDM) systems [83]. However, in some distinct applications, for instance, systems of high power pulse amplification and delivery[4] a presence of HOMs is still extremely undesirable, since they can lead to pointing instability and fluctuating peak intensity, as well as reduce beam quality. In any of

the aforesaid scenarios, knowledge of the fibre modal content and modal properties are of a great interest and importance.

The primary aim of this thesis is the investigation, modelling and experimental evaluation of HOMs in an optical fibre of advanced design, suitable for a MDM implementation. In order to achieve this goal, an interferometric-based fibre characterisation technique, in particularly a cross-correlated (C^2) imaging, was investigated and implemented for characterisation of different types of fibres. As a transmission media for MDM was chosen a 19-cell hollow core (HC) photonic bandgap fibre (PBGF) with anti-resonant elements, due to its low loss transmission bandwidth within the C-band. Through theoretical modelling, the main properties of the fibre modes were derived. They were experimentally evaluated by a spectrally and spatially (S^2) resolved imaging technique with a spectrogram approach and by a time-of-flight technique. Simultaneously, an investigation of the OAM modes excitation and propagation in the fibre was carried out. A description of the thesis organisation is presented below.

Organisation of the thesis

In this section the work accomplished in the thesis "Design of optical fibres with advanced modal control properties" is presented.

Chapter 2 presents a theoretical background of the thesis. In the beginning of the chapter is described a general theory of optical waveguides and a scalar approximation for a weakly-guiding fibre. A distinct case of LP_{ml} modes, derived from the scalar wave equation, is discussed for the simplest structure of a step-index fibre. Also the chapter covers a brief description of fibre dispersion, basic properties of the photonic crystal fibres (PCFs) as well as methods of excitation and detection of HOMs in an optical fibre.

Chapter 3 introduces principles of a cross-correlated (C^2) imaging technique for a fibre modal content characterisation. After a description of the fundamentals of the method, an alternative modal reconstruction approach is following. A flexible C^2 imaging is achieved by an application of a tunable and highly flexible light source. An investigation of an influence of a spectral shape and bandwidth on a temporal resolution of the C^2 method as well as an approach to shape the input spectrum according to experimental requirements of the fibre design are described. The method is implemented for characterisation of a step-index fibre (SMF28) and a distributed mode filtering (DMF) rod fibre over a broad range of wavelengths. A model of the rod fibre is presented in the chapter and results of simulation are compared with measurements. The last section of Chapter 3 describes a verification of the sensitivity and reliability of the flexible C^2 approach. An evaluation of the modal cutoff for a polarization maintaining (PM) fibre is performed and a comparison of two imaging techniques, namely the C^2 and the spatially and spectrally (S^2) resolved imaging, is made characterising a hollow core photonic crystal fibre.

Chapter 4 presents a model of a 19-cell HC PBGF. During modelling the effective refractive indices of the fibre modes and modal losses are derived, and the intermodal delays are calculated. As a result, are selected two groups of the full vectorial modes that can be supported by the fibre for a data transmission under a mode division multiplexing (MDM) scenario.

In Chapter 5 an experimental characterization of the modelled 19-cell HC PBGF is presented. The chapter is divided into two parts. The first part presents the detection of the fibre modes within a broad wavelength range by a modified S^2 technique performed with a spectrogram approach. Results of the experimental and numerical fibre analysis are compared. In the second part of the chapter a characterisation of 325m of the 19-cell HC PBGF is presented by a time-of-flight technique (ToF),

when OAM modes are generated and coupled into the fibre. The modes are excited using spatial light modulator (SLM) and Q-plate. The set-up for OAM modes multiplexing and demultiplexing is built and tested.

The conclusion and an outlook are presented in Chapter 6.

Chapter 2

Theory of fibre

2.1 Basics of optical fibres

An optical fibre is a dielectric waveguide, where light is confined in a central core embedded in a cladding. A transverse geometry of the fibre primarily determines its guiding mechanism and optical properties, as loss, dispersion, quantity of propagating modes, etc.

Figure 2.1 (a) depicts a sketch of a fibre in its simplest form. A core, of a diameter d and a refractive index n_c, is surrounded by a cladding with a lower refractive index n_{cl}. A change of the refractive index profile from the core to the cladding is abrupt and step-like. Owign to that a fibre is known as a step-index fibre. In that type of fibres light is guided by the phenomenon of total internal reflection (TIR). The TIR can be described by a ray picture based on geometrical optics [12], depicted in Figure 2.1 (b), under an assumption that the core radius a ($a = d/2$) is much larger than the wavelength of light λ.

When light is incident on a core-cladding interface, due to the law of refraction [12] , an angle of incidence θ_i is related to an angle of refraction θ_r as

$$n_0 sin(\theta_i) = n_c sin(\theta_r), \tag{2.1}$$

where n_0 and n_c are refractive indices of the ambient medium and the core. All rays, that entered the fibre and are indecent at the core-cladding interface by an angle greater than a critical angle θ_c,

$$\theta_c = sin^{-1}(n_{cl}/n_c) \tag{2.2}$$

undergo the TIR at the core-cladding boundary and are reflected back in the core. The back reflection is maintained along the whole length, preserving light confined within the core. The maximum angle of acceptance, within which incident light is coupled and guided in a fibre, can be found as [2, 91]

$$n_0 sin(\theta_i) = n_c cos(\theta_c) = \sqrt{n_c^2 - n_{cl}^2} = NA, \tag{2.3}$$

where NA is a numerical aperture (NA) of a fibre, which determines its light-gathering capacity.

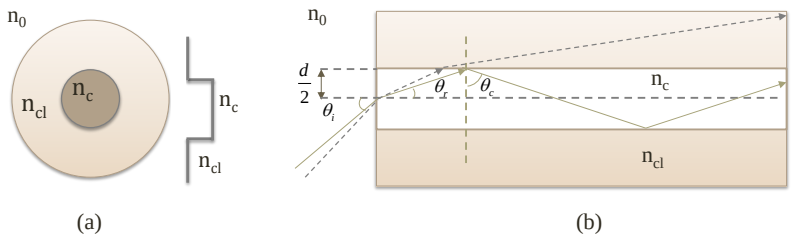

Fig. 2.1 (a) A schematic representation of a cross-section and a refractive index profile of a step-index fibre. (b) A sketch of light confinement in a fibre through the phenomenon of total internal reflection. Solid ray is confined and propagate along the core, while dashed ray refracts at the core-cladding boundary.

Each ray, coupled into a fibre at a discrete angle, can be associated with a fibre mode, that is a characteristic pattern of light in which it propagates in a fibre [69]. However, a description of light propagation by the ray-theory is limited and cannot explain many important optical phenomena, since it does not consider the wave nature of light. A better understanding gives the electromagnetic theory of optical waveguides.

2.2 Wave equation

General properties of light in optical waveguides are described by Maxwell's equations [69, 34]. Taking in consideration material properties of waveguide and applying the boundary conditions at surfaces, where the material constants changes, one can derive the vector wave equation of the electromagnetic field [69, 34]:

$$\begin{aligned} \bigtriangledown^2 E + \varepsilon(r) k_0^2 E = 0, \\ \bigtriangledown^2 H + \varepsilon(r) k_0^2 H = 0, \end{aligned} \tag{2.4}$$

where $\bigtriangledown^2$ is Laplacian operator, **E** and **H** are the electric and magnetic field vectors, k_0 is the free space wave number, which is equal to

$$k_0 = \frac{2\pi}{\lambda} = \frac{\omega}{c}, \tag{2.5}$$

and $\varepsilon(r)$ is the permittivity dependent on the radial coordinate. When a difference between the refractive indices of the core and cladding is small

$$\Delta = n_c - n_{cl} \ll 1 \tag{2.6}$$

the weak guidance approximation can be applied and the scalar wave equation in the cylindrical coordinates (r,θ,z) can be written as [69, 34]:

$$\begin{aligned}\frac{\partial^2 E_z}{\partial r^2}+\frac{1}{r}\frac{\partial E_z}{\partial r}+\frac{1}{r^2}\frac{\partial^2 E_z}{\partial \theta^2}+\varepsilon(r)k_0^2 E_z=\beta^2 E_z\\ \frac{\partial^2 H_z}{\partial r^2}+\frac{1}{r}\frac{\partial H_z}{\partial r}+\frac{1}{r^2}\frac{\partial^2 H_z}{\partial \theta^2}+\varepsilon(r)k_0^2 H_z=\beta^2 H_z\end{aligned} \tag{2.7}$$

The parameter β in the RHS of Eq.(2.7) is known as a propagation constant. Since the scalar equation is equally valid for **E** and H fields, the similar solutions can be derived for both of them. Therefore, further below is considered only the electric field. Assuming, that a solution of Eq.(2.7) can be presented in the form [69]:

$$E_z = E_0 R_m(r)\Psi_m(r,\theta)exp(-j\beta z), \tag{2.8}$$

where E_0 is a complex field amplitude, $R_m(r)$ and $\Psi_m(r,\theta)$ are the radial and azimuthal profiles, and taking into account that a fibre possesses the circular symmetry, the azimuthal function can be chosen to be trigonometric:

$$\begin{aligned}\Psi_m(r,\theta)^c = R_m(r)cos(m\theta),\\ \Psi_m(r,\theta)^s = R_m(r)sin(m\theta),\end{aligned} \tag{2.9}$$

here m is a positive integer, that denotes the azimuthal order of the mode. $\Psi_m(r,\theta)^c$ and $\Psi_m(r,\theta)^s$ indicate that each mode can exist in two polarization states. The resultant equation for the radial distribution can be rewritten as [34]:

$$\begin{aligned}\frac{\partial^2 R_m(r)}{\partial r^2}+\frac{1}{r}\frac{\partial R_m(r)}{\partial r}+\left(n_c^2k_0^2-\beta^2-\frac{m^2}{r^2}\right)R_m(r)=0\\ \frac{\partial^2 R_m(r)}{\partial r^2}+\frac{1}{r}\frac{\partial R_m(r)}{\partial r}-\left(\beta^2-n_{cl}^2k_0^2+\frac{m^2}{r^2}\right)R_m(r)=0\end{aligned} \tag{2.10}$$

The solutions of Eq.(2.10) describe the radial distribution of the filed in the fibre core and cladding, and are Bessel functions of integer order.

Since the field of guided modes decays very rapidly in the cladding and never reaches its outer boundary, can be made an assumption of an infinity thick cladding for simplification of results derivation. Beside being a common fibre widely used in optical communication systems, a step-index fibre also has the simplest mathematical treatment, therefore further insight of light propagation in a fibre is derived for step-index fibre.

2.3 Step-index fibre

The cross-section of a step-index fibre is presented in Figure 2.1 (a). To find the field distribution of the guided mode in the core and cladding of the fibre, Bessel's differential equations [Eq.(2.10)] have to be solved for the radial function $R_m(r)$. Introducing the transverse wave numbers in the core u and in the cladding υ as [69]:

$$\begin{aligned} u &= \sqrt{n_c^2 k_0^2 - \beta^2} \\ \upsilon &= \sqrt{\beta^2 - n_{cl}^2 k_0^2} \end{aligned} \tag{2.11}$$

the solutions of Eq. (2.10) are eminent and have the form of the Bessel function of the first kind $J_m(u)$ for the core region and the modified Bessel function $K_m(\upsilon)$ for the cladding region. The form of solutions demonstrate the confinement of the guided mode within the core and its exponential decay in the cladding.

$$\begin{aligned} E_z &= E_{01} J_m(ur) cos(m\theta) exp(-j\beta z) \quad r < a \\ E_z &= E_{02} K_m(\upsilon r) cos(m\theta) exp(-j\beta z) \quad r > a \end{aligned} \tag{2.12}$$

where a is the radius of the core, r and θ are radial and azimuthal coordinates, E_{01} and E_{02} are the field amplitudes in the core and cladding. Implying the boundary conditions: the radial function $R_m(r)$ is continuous and its derivative is also continuous at the core-cladding interface

($r = a$), where the value of refractive index changes, the eigenvalue equations can be derived for modes in a fibre in term of the propagation constant β for the known core radius, wavelength and refractive indices of the core and cladding[69, 34, 34]. Solutions of the eigenvalue equation, also known as the characteristic equation or dispersion relation [69], give a set of discrete values of the propagation constant β_{ml}, where m and l correspond to the radial and azimuthal order of mode. Therefore, each mode in a fibre propagates with its own propagation constant β_{ml} within an allowed range of $n_{cl}k_0 < \beta < n_c k_0$.

The parameters u and υ determine a rate of change of the radial function $R_m(r)$ in the core and cladding. The larger value of u, more oscillations present in the core region, while larger value of υ means tight mode confinement in the core due to small penetration into the cladding region of the rapidly decaying field. From Eq.(2.11) transverse wave numbers are related as

$$u^2 + \upsilon^2 = k_0^2(n_c^2 - n_{cl}^2)a^2 = V^2 \tag{2.13}$$

where k_0 is the free space wave number, a is the core radius ($a = d/2$), n_c and n_{cl} are the refractive indices of the core and cladding and V is known as the normalized frequency or V-parameter, that identifies the quantity of the guided modes in a fibre.

In general, propagating fibre modes are hybrid modes with both present electric and magnetic longitudinal components of the fields, denoted as HE_{ml} and EH_{ml}. Other two types of modes, that can also propagate in a fibre, are the pure transverse electric TE_{0l} and transverse magnetic TM_{0l} modes [34]. The exact expressions of the eigenvalue equations for the fibre guided modes were for the first time derived by Snyder in Ref.[99]. To simplify derivation of the solutions in the aforesaid reference was proposed the weak guiding approximation based on an assumption that the contrast of the refractive indeces of the core and

cladding is weak [Eq.(2.6)] and transverse fields of the fibre modes are orthogonally polarized. Modes in a weak-guiding fibre are linearly polarized and denoted as LP_{ml} modes. Worth to note, that both polarizations of the mode have the same propagation constant and the same spatial distribution. The simplified expressions for LP modes were derived by Gloge in Ref.[32]. According to it the eigenvalue equation under the weak-guiding approximation is

$$u\frac{J_{m-1}(ua)}{J_m(ua)} = -\upsilon\frac{K_{m-1}(\upsilon a)}{K_m(\upsilon a)} \tag{2.14}$$

Equation (2.14) gives a full set of solutions for the guided LP modes and allows to determine the corresponding propagation constant β_{ml} and radial distribution function $R_m(r)$ of each mode. Examples of the radial distributions of the electric field of the four first LP modes is presented in Figure 2.2. Also Eq.(2.14) is valid for the hybrid modes HE_{ml} and EH_{ml}. A correspondence between LP modes and full vectorial modes is shown in Table 2.1. As it can be seen from Table 2.1, LP modes can be obtained as superimposition of the corresponding vectorial modes. The fundamental fibre mode (FM) HE_{11} can be compared to the fundamental LP_{01}, while the first order of the higher order modes (HOMs) LP_{1l} ($l = 0$) is combined from TE_{0l}, TM_{0l}, HE_{2l} modes. The HOMs of higher order ($m > 1$) correspond to superimposition of HE_{m+l} and EH_{m-l}. The weak-guidence approximation is also known as the scalar approximation, since the fields of the propagating modes are derived from the scalar wave equation. It is worth to mention, that under the scalar approximation LP modes in subgroups have the same β-eigenvalues. Modes, that have $m = 0$, are double-degenerate, due to polarization degeneracy, and modes with $m > 0$ are four-fold generate, due to additional sine and cosine solutions [Eq.(2.9)].

Every fibre can support the limited number of modes, that is determined by the V-parameter, derived in Eq.(2.13). The same parameter

Table 2.1 The correspondence between the full vectorial modes and LP modes.

LP modes	Full vectorial modes	
LP_{0l}	HE_{1l}	$m = 0, l = 1$
LP_{1l}	TE_{0l},TM_{0l},HE_{2l}	$m = 1, l = 1$
LP_{ml}	HE_{m+l},EH_{m-l}	$m > 1, l \geqslant 1$

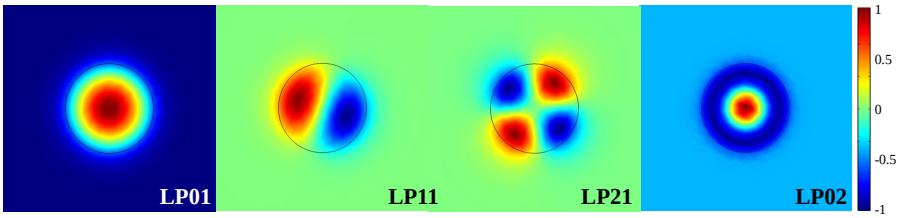

Fig. 2.2 The normalized filed distributions for the four first LP modes: $LP_{01}, LP_{11}, LP_{21}, LP_{02}$. The red and blue shading in the field distributions correspond to π phase shift.

can be also obtained from the characteristic equation Eq.(2.14). Assuming the poorly confined mode with the field exponentially decaying in the cladding and the propagation constant close to the value of $n_{cl}k_0$, the transverse wave number will be close to zero ($\upsilon \approx 0$), that brings requirement of the cutoff condition for a mode:

$$J_{m-1}(V) = 0 \tag{2.15}$$

The V-parameter proportional to the ratio between the core radius and wavelength (a/λ) and it means, that increasing V-parameter to a certain cutoff value, determined by Eq.(2.15), a special condition is reached and a mode cannot be guided by a fibre. Therefore, for a given fibre a wavelength, for which V=2.405, is known as the cutoff wavelength λ_c. For $0 < V < 2.405$, a fibre supports only the FM and operates in a

single-mode regime. For $V > 2.405$, a fibre is considered as a few-mode or multi-mode fibre.

2.4 Dispersive properties of a fibre

One of the most important parameters of the guided modes is the effective refractive index, that can be introduced from the propagation constant β as:

$$n_{eff} = \frac{\beta}{k_0} \tag{2.16}$$

A dependence of the refractive index on wavelength is known as dispersion [12] and leads to dispersive properties of the modes. Different frequency components of an optical pulse due to a wavelength dependence of the refractive index propagate in the fibre with the different velocities, which leads to the pulse broadening due to dispersion. There are four kinds of dispersion in a fibre [79, 69, 91]: modal dispersion, caused by the difference of the group velocities of propagating modes; polarization-mode dispersion, that causes the mode in two polarizations to propagate with different group velocities due to the inhomogeneities and anisotropies of the fibre core; material dispersion, arises from a dependence of the refractive index of the core and cladding on wavelength; and waveguide dispersion as result of a contribution of the waveguide structure.

Generally, for characterization of dispersion is used D-parameter that describes the variation of the time delay along the whole length of a fibre per wavelength difference[79, 61]:

$$D = \frac{1}{L}\frac{\mathrm{d}\tau}{\mathrm{d}\lambda}, \tag{2.17}$$

where L being a fibre length, τ is a propagation time difference and λ is a wavelength. It is well known, that a plane monochromatic wave propagates with a velocity governed by its phase [79]:

$$\upsilon_p = \frac{\omega}{\beta}, \tag{2.18}$$

where ω is an angular frequency of the wave, c is the speed of light. Whereas, a velocity of the wave packet or pulse, is determined by the group velocity:

$$\upsilon_g = \frac{\mathrm{d}\omega}{\mathrm{d}\beta}, \tag{2.19}$$

Then, the group propagation time along the fibre of the length L is

$$\tau = \frac{L}{\upsilon_g} = \frac{L}{c}\left(n - \lambda\frac{\mathrm{d}n}{\mathrm{d}\lambda}\right) \tag{2.20}$$

Equation (2.20) expresses the group delay as a function of the refractive index n and the wavelength λ. An expression under brackets is known as the group index. In the analogy with the phase velocity υ_p, that can be also determined by the refractive index n, the group velocity as well as the group delay is determined by the group index [79]. Taking the derivative of the group delay over the wavelength one can derive the D_m parameter as [61]

$$D_m = -\frac{\lambda}{c}\frac{\mathrm{d}^2 n}{\mathrm{d}\lambda^2}, \tag{2.21}$$

where D_m is a material contribution of dispersion to the total dispersion of a fibre. Material dispersion of silica glass can be empirically described by the Sellmeier interpolation equation [69], that reveals a relation between the refractive index of silica glass and wavelength. Material dispersion is intrinsic to all bulk materials and does not depend on the geometry of a fibre.

In the case, if one derives the dispersion parameter with respect to frequency neither to wavelength starting from a Taylor series expansion of $\beta(\omega)$ [79, 69, 61]

$$\beta(\omega) = \beta(\omega_0) + (\omega - \omega_0)\frac{\mathrm{d}\beta}{\mathrm{d}\omega} + \frac{(\omega - \omega_0)^2}{2}\frac{\mathrm{d}^2\beta}{\mathrm{d}\omega^2} + \frac{(\omega - \omega_0)^2}{6}\frac{\mathrm{d}^3\beta}{\mathrm{d}\omega^3} + \cdots \tag{2.22}$$

then the parameter D_m is

$$D_m = -\frac{2\pi c}{\lambda^2}\beta_2, \tag{2.23}$$

where β_2 is called a group velocity dispersion (GVD) parameter that equal to:

$$\beta_2 = \frac{\mathrm{d}^2\beta}{\mathrm{d}\omega^2} = \frac{1}{c}\left(2\frac{\mathrm{d}n}{\mathrm{d}\omega} + \omega\frac{\mathrm{d}^2 n}{\mathrm{d}\omega^2}\right), \tag{2.24}$$

and describes a variation of the group velocity with wavelength.

In many cases, since a change of the refractive index of the core and cladding with wavelength is small, an approximation can be made assuming the refractive index of material being constant. However, as wavelength increases, a field of mode in a fibre extends more and more into the cladding, experiencing more the cladding refractive index than just the core refractive index [91, 61]. Under aforesaid circumstances waveguide dispersion arises and for a step-index fibre it is [69, 32, 31]

$$D_w = -\frac{n_{cl}\Delta}{c\lambda}\left(V\frac{\mathrm{d}^2}{\mathrm{d}V^2}(Vb)\right), \tag{2.25}$$

where Δ is $\sim (n_c - n_{cl})/n_{cl}$, V is the normalized frequency, defined by Eq.(2.13), and b is the normalized propagation constant of the mode, that is equal to

$$b = \frac{n_{eff}^2 - n_{cl}^2}{n_c^2 - n_{cl}^2} \tag{2.26}$$

For large values of the parameter V, the normalized propagation constant b tends to 1, while at the cutoff $b = 0$. Waveguide dispersion is individual for each mode and can be tailored by a proper design of fibre profile. The total dispersion of a fibre can be represented as contribution of material D_m and waveguide D_w dispersion:

$$D \approx D_m + D_w \tag{2.27}$$

It worth to note, that under certain circumstances material and waveguide dispersion can cancel each other at a certain wavelength known as zero-dispersion wavelength.

As a conclusion, in this section were introduced and described the characteristic equation for a step-index fibre and its solutions in the core and cladding for the propagating modes, cutoff parameters and waveguide dispersion. The next section is focused on optical fibres of the advanced design, in particularly photonic crystal fibres.

2.5 Photonic crystal fibres

A photonic crystal fibre (PCF) is a fibre with a regular periodic pattern of holes in a cladding maintained along the whole length of its axis [91]. There are two main types of the PCFs: the solid-core and hollow-core. Depending on a type of the PCFs, light can be guided by one of the two mechanisms: by the total internal reflection (TIR), as in a conventional fibre (Section 2.1), or due to the photonic band gap phenomenon.

The properties of the PCF are governed by the geometry and determined by the pitch Λ, diameter d and relative diameter d/Λ of the air holes [Figure 2.3].

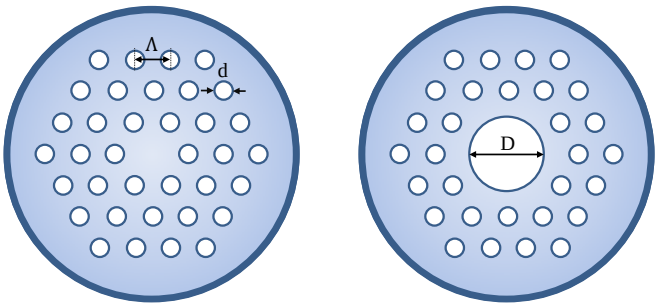

Fig. 2.3 The schematic view of the solid-core (a) and hollow-core (b) PCFs.

Solid-core PCF

Despite an unconventional design, the solid-core PCF, due to its mechanism of guiding light by the TIR, has preserved some key properties of a common fibre. They also support a FM along all wavelengths, while HOMs experience the cutoff at certain wavelengths. However, an insertion of air voids in the cladding decreases its average refractive index, leading to a vanished distinct border between the core and cladding. On the one hand, it becomes possible to overcome the limitation of a small index contrast in a common fibre, that is typically $\sim 1\%$. On the other hand, the propagation constant in this case is limited within the range [9]

$$k_0 n_{silica} > \beta > \beta_{FSM}, \tag{2.28}$$

where β_{FSM} is known as the propagation constant of the fundamental space-filling mode (FSM) and is the maximum allowed β in the cladding in the case when the core is absent. Therefore, for the solid-core PCF

a relation for the normalized frequency is changed and depends on the pitch Λ and the effective refractive index of the cladding n_{eff} as :

$$V_{eff} = \frac{2\pi\Lambda}{\lambda}\sqrt{(n_o^2 - n_{eff}^2)}, \tag{2.29}$$

where n_{eff} is determined by β_{FSM} corresponding to Eq.(2.16) as

$$n_{eff} = \frac{\beta_{FSM}}{k_0} \tag{2.30}$$

It worth to mention, that for a ratio of holes size d/Λ less than 0.5 in the short wavelengths limit ($d/\Lambda >> 1$) V_{eff} is finite and does not depend on λ or Λ, maintaining endlessly single-mode operation of a fibre. However, a decrease in a hole size reduces the contrast between the refractive indices of the core and cladding, making the fibre more susceptible to bending loss. On the other hand,an increase in a hole size leads to appearance of HOMs in a fibre.

Opportunity to vary an index contrast, hole-to-hole distance Λ, diameters of the core and holes, makes it possible to create fibres with exceptional optical properties. For example, fibres of a large mode area, that simultaneously operate in a single-mode (SM) regime over a broad range of wavelengths.

Hollow-core PCF

This type of PCFs is also known as a hollow core photonic bandgap fibre (HC PBGF), due to thier peculiar guiding mechanism based on a bandgap phenomenon. In the case of the HC PBGF, light is trapped and guided in an air hollow core of the fibre with a lower refractive index than the refractive index of the cladding due to a forbidden range of frequencies, known as a bandgap region, where electromagnetic propagation at any incident angle is impossible. The idea of HC PBGF originates from properties of a three-dimensional photonics crystal, where light is trans-

mitted within a band of forbidden frequencies as a result of destructive interference on the elements of periodic structure [91]. To guarantee a propagation of modes in the air-core region without a possibility to escape into the cladding, the effective refractive index of mode has to be less than unity ($\beta/k_0 < 1$)[87]. Aforesaid features create the main difference between the solid-core and HC PCFs.

For the HC PBGF there are two main loss mechanisms, that contribute to the total loss: the scattering loss (SL) and confinement loss (CL). A magnitude of the CL is strongly depends on the number of the air holes rings and can be reduced by designing a fibre with several rings of the air-holes [90]. A dominating contribution, that has an overwhelming impact on the total loss, comes from the scattering at the air-glass interfaces within HC PBGFs due to an intrinsic roughness on the surfaces, created by the thermally excited surface capillary waves, that are frozen into the glass during the manufacturing [25]. Measurement of the SL is not straightforward, as well as there is no distinct way of the SL simulation. The common approach is to assume, that the SL is proportional to a normalized field intensity F along the air-glass interfaces and hence, proportional to [26]:

$$\alpha_{SC} = \eta F = \eta \left(\frac{\varepsilon_0}{\mu_0}\right)^{\frac{1}{2}} \frac{\oint_{holes-perimeter} \left|\overrightarrow{E}\right|^2 dl}{\iint_{cross-section} \overrightarrow{E} \times (\overrightarrow{H^*}) \cdot d\overrightarrow{A}}, \tag{2.31}$$

where η is an empirically obtained proportionality factor, which is according to Ref.[26] equal 300, E and H are the electric and magnetic fields of the guided modes. The CL of each mode can be derived as an imaginary part of the effective refractive index [58]:

$$\alpha_{CL} = \frac{40\pi}{\lambda ln10} Im(n_{eff}), \tag{2.32}$$

where $Im(n_{eff})$ is the imaginary part of the modal effective refractive index simulated at each wavelength λ in COMSOL.

2.6 Excitation of higher order modes in fibres

A control of modal content coupled into a optical fibre and selective excitation of modes in a optical fibre are desirable in many applications, especially in fibre-based communication systems, high power pulse delivery and fibre sensing. In order to find a reliable and easy-implement solution for modal excitation were developed methods based on holographic filters [24] and holograms created by a spatial light modulator (SLM) [15, 100], phase plates [108, 102, 104], fiber Bragg gratings (FBG) [3] and long-period gratings (LPG) [81, 112]. A choice of a method depends on conditions of an experiment and required type, efficiency and purity of the excited modes.

One of the methods implemented in this thesis for a deliberate excitation of modes in a fibre is LPGs. Generally, there are two types of LPGs: photoinduced LPGs, written in a fibre by laser altering the refractive index of the core in a periodic manner [53, 92], and mechanically created LPGs by applying a pressure to a fibre [111, 11, 92]. Figure 2.4 depicts both types of LPGs. The main principle of work is similar and based on a coupling of two forward co-propagating modes due to the periodic modulation of the core index in the fibre when the phase matching condition is satisfied [106, 22]

$$\beta_1 - \beta_2 = \frac{2\pi}{\Lambda}, \tag{2.33}$$

where β_1, β_2 are the propagation constants of two modes, Λ is a pitch or a period of gratings, formed by the refractive index change, and m is an integer. When the coupling of the FM to one of the HOMs takes place, a sharp spectral resonance is occurring with corresponding drop

of power in the transmission spectrum at distinct wavelength λ_{res}, where the phase matching condition is satisfied. Equation (2.33) describes the simple case of first order diffraction. Hovewer, to take into account the higher orders of diffraction the phase-matching condition can be rewritten as [39]

$$\lambda_{res} = (n_{eff1} - n_{eff2})\frac{\Lambda}{N}, \tag{2.34}$$

where N denotes a diffraction order.

Permanent LPGs can be written into the hydrogen loaded fibre by exposing it to UV light or intense heat. In the regions, where defects are present, UV induces the distructions of the silica bonds resulting in an increase of the refractive index [41]. In the case of mechanically induced gratings, a change of the refractive index is caused by a pressure applied all over above the fibre. Induced stress creates points in the fibre where the refractive index is altered due to a photo-elastic effect. Such periodic stressing over a beat length forces the FM to couple into one of the HOMs, when a phase-matching condition is satisfied. To control the higher-order modes excitation, the fibre is placed into a V-groove of a flat metallic plate and pressed from above by a grating plate with a chosen period Λ. A depth of notch at the transmission spectrum is relevant to the conversion efficiency, that is controlled by the pressure implied to the spring-loaded clamp on the fibre. The high pressure results in a stronger modal conversion. However, after a some level of pressure the depth of notch does not change any more or decreases due to overcoupling [10]. For verification of the mode conversion, an output of the fibre is spiced with a single mode fibre, which is connected to an optical spectrum analyser (OSA).

Every type of LPGs has its own advantages and disadvantages. LPGs written in a fibre are highly reliable and small in size. However, once been written, it is impossible to change any of the LPG parameters.

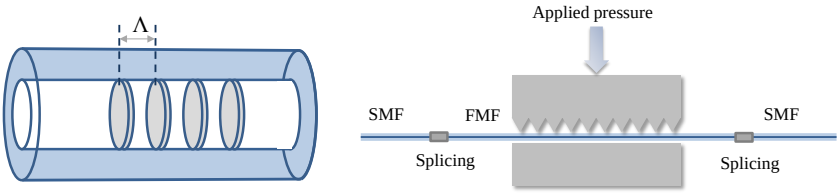

(a) (b)

Fig. 2.4 The sketch of the LPGs written in a fibre (a) and mechanically created gratings (b).

In mechanically induced LPGs the grating period can be adjust at any time by changing the period of grating at the metallic plate or an angle between the fibre and the grooves. Moreover, when the stress is released the structure of fibre recovers and its transmission spectrum returns to initial. However, since a mechanically induced grating couples light from the FM to one of the asymmetric modes, it suffers from inherent polarisation dependence [33], because the asymmetric modes, to which coupling occurs, are nearly degenerate linear combinations of the responsible group of polarised vectorial fibre modes with different propagation constants.

For experimental characterisation of excited fibre modes can be implemented one of the modal characterisation techniques, overviewed in the next section.

2.7 Overview of the imaging techniques for the fibre modes characterisation

Among developed approaches for a fibre modal content decomposition, a spatially and spectrally resolved imaging (S^2) and cross-correlated imaging (C^2) can be acknowledged as the most applicable techniques, due to their notable ability efficiently characterise propagating fibre modes and determine relative modal powers, intensity and phase distributions, and intermodal time delays. Both methods are interferometric-based approaches, that provide an information about characterised modes analysing an interference pattern, created by an interaction of the fibre modes with reference mode. In the case of the S^2 imaging, the reference mode is the dominate mode of the fibre, while for the C^2 imaging, it is the FM of the reference fibre, introduced as one of the Mach-Zehnder interferometer (MZI) arms. Originally, the S^2 technique was proposed and investigated by Nicholson *et al.* in Ref.[65]. A set-up was based on a broadband light source, launched into a large-mode-area (LMA) fibre, and an optical spectrum analyser (OSA), that measured optical spectra in each (x,y) point of the rasterised fibre output. A data analysis was performed via the Fourier transform of the all acquired optical spectra, resulting in a trace, that represents a beating amplitude of modes as a function of differential group delay (DGD). Simultaneously, the first demonstration of the C^2 imaging was reported by Schimpf *et al.* in Ref.[93]. A modal content characterisation was performed in the time domain and a set-up was based on a MZI. As a light source was used superluminescent diode. A change of intensity, due to an interference between the FM from the reference fibre and modes from the fibre under test (FUT), was captured as a stack of images at a fibre output by a camera at each position of a time delay line. Analysing a set of acquired pictures a C^2 trace is found as a function of intensity varying with time, revealing a cross-correlation between the input spectrum and interference

peaks, that occur at the corresponding to each mode in the FUT time delays.

Later several improvements for both techniques were proposed and reported. For example, the measurement time of the S^2 imaging was improved by implementing a fast image acquisition approach [66]. In this case, instead of a broadband light source in combination with an OSA, was used a tunable laser with a camera. Demonstration of a real-time S^2 measurement was reported in Ref.[35] by implementing a continuous scanning laser source with inline data processing system, characterising the modal content of 19-cell HC PBGF. The same acquisition time was also reported for the C^2 imaging in the frequency domain (fC^2) [20]. The setup was based on a tunable diode laser and a CMOS camera. A set of $LP_{0,m}$ modes was excited and coupled to a multi-mode dual-clad fibre by a spatial light modulator (SLM). The measurement was performed in a sub-second with a further post-processing analysis of the fibre modal content.

A full potential of the techniques can be demonstrated by a two dimensional spectrogram analysis of the fibre modal content, as it was reported in [35, 46, 16]. The relative modal power was represented as function of DGD and wavelength on a spectrogram revealing the entire modal dynamics.

As a modification of the cross-correlated imaging technique the white-light interferometry method reported in Ref.[51] can be considered. Here a highly resolvable time resolution is achieved by the application of the same test fibre in both arms of an interferometer, that precisely matches the residual group velocity dispersion and permits to resolve the modal group delays on the scale of few femtoseconds.

The focus of the next chapter is on an implementation of the C^2 imaging for a characterisation of the different types of fibres and on an investigation of the main effects, that have influence on its performance.

Chapter 3

C^2 imaging technique for fibre characterisation

In this Section a cross-correlated C^2 imaging technique is proposed for the characterisation of the modal content of different types of fibres. At the beginning the basic principles of the imaging technique are reviewed and the technique is implemented for the step index fibre. Afterwards, an alternative method of modal reconstruction is suggested for characterization of the solid-core and hollow-core PCFs over a broad range of wavelengths.

3.1 Principles of the C^2 imaging technique

Principles of interferometry

Real light sources can be characterised by their temporal and spatial coherence. An intensity of the randomly varying light can be defined by an average of its complex wavefunction $U(r,t)$ [91]

$$I(r,t) = \left\langle |U(r,t)|^2 \right\rangle \tag{3.1}$$

When the statistical average of the wave intensity is invariant in time, the light is considered to be statistically stationary and its intensity can be averaged not over the many of realizations of the wave, but over a long time duration T as

$$I(r) = \lim_{T\to\infty} \frac{1}{2T} \int_{-T}^{T} |U(r,t)|^2 \, dt \tag{3.2}$$

Generally, real light sources are not monochromatic and radiate at different frequencies within a finite spectral width of $\Delta\nu$. However, within the interval of time $\tau_c \ll 1/\Delta\nu$, when the complex amplitude is constant, the non-monochromatic source operates as a monochromatic, radiating light with a mean frequency of the light source. The current characteristic time τ_c is known as the coherence time of the source [12] and is characterised by a complex degree of temporal coherence $g(\tau)$ as

$$g(\tau) = \frac{\langle U^*(t)U(t+\tau)\rangle}{\langle U^*(t)U(t)\rangle} = \frac{G(\tau)}{G(0)}, \tag{3.3}$$

which shows the degree of correlation between the function $U(t)$ in the time t and the same function delayed by the time $t+\tau$. $G(\tau)$ is the autocorrelation fuction, that defines to which extent the functions $U(t)$ and $U(t+\tau)$ are correlated. The absolute value $|g(\tau)|$ extends from zero to unity. Zero values mean that light is incoherent, and for unity the light is coherent, meaning that it is highly correlated along all time delays. The coherence time τ_c can be also derived through the complex degree of temporal coherence as the time at which $|g(\tau)|$ reaches the values of $1/e$ [12, 91], also more commonly defined as

$$\tau_c = \int_{-\infty}^{\infty} |g(\tau)|^2 \, d\tau \tag{3.4}$$

Through the coherence time one can determine the coherence length l_c, which is an important parameter for describing the interference be-

tween two beams. Knowing the mean wavelength λ_0 and the bandwidth of the source $\Delta\lambda$, l_c is equal to

$$l_c = c\tau_c \approx A\frac{\lambda_0}{\Delta\lambda}, \tag{3.5}$$

where A is a coefficient, that depends on the spectral shape of the source and for the Gaussian spectral shape it is equal to $2ln(2)/\pi$.

Figure 3.1 describes a scheme of the Mach-Zehnder interferometer. Light from a partially coherent source is split into two arms of interferometer and recoupled at the second beam splitter, after propagating paths S_1 and S_2. In the case, when the difference $S_1 - S_2$ is less than the coherence length l_c of the light source ($S_1 - S_2 \leqslant l_c$), the two beams interfere creating an interference pattern, that can be captured by the camera at the output of the setup. However, when an optical path difference (OPD) is larger than the coherence length (OPD$> l_c$), for example, as for an extended optical path S_3, that is much larger than S_2, the beams do not interfere.

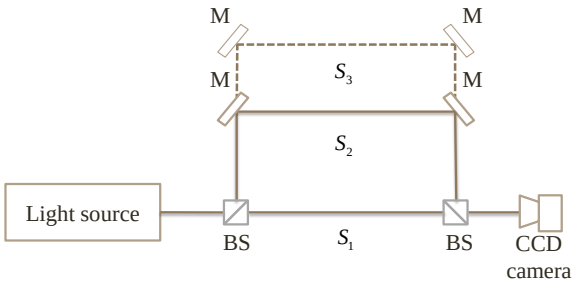

Fig. 3.1 A schematic representation of the Mach-Zehnder interferometer. Here, S_1 is an optical path of the beam in one arm, S_2 in another arm, S_3 is an extended optical path ($S_3 > S_2$) , BS is beam splitter.

At the camera, the total intensity of the two superimposed waves can be written as:

$$I(\mathbf{r},t) = I_1(\mathbf{r},t) + I_2(\mathbf{r},t) + 2\sqrt{I_1(\mathbf{r},t)}\sqrt{I_2(\mathbf{r},t)}\mathrm{Re}\,(g_{12})\left(\frac{S_1 - S_2}{c}\right), \tag{3.6}$$

where $I_1(\mathbf{r},t)$ and $I_2(\mathbf{r},t)$ are averaged intensities of the beams from each arm, which are determined by the self-coherence functions $G_1(0)$ and $G_2(0)$; g_{12} is the normalized cross-correlation function of two waves $U_1(\mathbf{r},t)$ and $U_2(\mathbf{r},t)$, that shows to which degree they are correlated and defined as

$$g_{12}(\mathbf{r},\tau) = \frac{\langle U_1(\mathbf{r},t+\tau)U_2^*(\mathbf{r},t)\rangle}{\sqrt{G_1(\mathbf{r},0)}\sqrt{G_2(\mathbf{r},0)}} = \frac{G_{12}(\tau)}{\sqrt{I_1(\mathbf{r},t)}\sqrt{I_2(\mathbf{r},t)}} \tag{3.7}$$

Equation (3.6) is known as the general interference law for the stationary optical field [12] and can be represented in another way as

$$I(\mathbf{r},t) = I_1(\mathbf{r},t) + I_2(\mathbf{r},t) + 2\sqrt{I_1(\mathbf{r},t)}\sqrt{I_2(\mathbf{r},t)}\,|g_{12}(\mathbf{r},\tau)|\cos\left(\arg\left\{g_{12}(\mathbf{r},\tau)\right\}\right), \tag{3.8}$$

where τ is the OPD, that is equal to $\tau = (S_1 - S_2)/c$.

In the case of quasi-monochromatic light, the spectral bandwidth is smaller than the mean frequency of the light source. In this case, from Eq.(3.8) can be seen, that dependence of the normalized intensity at the point, where the two beams interfere, depends on the phase $\arg\{g_{12}(\mathbf{r},\tau)\}$ in a harmonic manner with an amplitude governed by $|g_{12}(\mathbf{r},\tau)|$. From Eq.(3.8) the maximum I_{max} and minimum I_{min} intensity values are reached when cosine in Eq.(3.8) is equal to ± 1, thus:

$$\begin{aligned} I_{max} &= I_1(\mathbf{r},t) + I_2(\mathbf{r},t) + 2\sqrt{I_1(\mathbf{r},t)}\sqrt{I_2(Q)}\,|g_{12}(\mathbf{r},\tau)| \\ I_{min} &= I_1(\mathbf{r},t) + I_2(\mathbf{r},t) - 2\sqrt{I_1(\mathbf{r},t)}\sqrt{I_2(Q)}\,|g_{12}(\mathbf{r},\tau)| \end{aligned} \tag{3.9}$$

The brightness morphology of the interferogram is described by the modulation depth or the visibility V and at the vicinity of $\tau = 0$ it is equal to:

$$V(\mathbf{r},0) = \frac{I_{max} - I_{min}}{I_{max} + I_{min}} = \frac{2\sqrt{I_1(\mathbf{r},t)}\sqrt{I_2(\mathbf{r},t)}}{I_1(\mathbf{r},t) + I_2(\mathbf{r},t)}\,|g_{12}(\mathbf{r},0)| \tag{3.10}$$

where I_{max} and I_{min} are the maximum and minimum intensities of the interference fringes derived by Eq.(3.9). Equation (3.10) shows, that the complex degree of coherence $g_{12}(\mathbf{r},\tau)$ determines the strength of interference of two interfering beams $I_1(\mathbf{r},t)$ and $I_2(\mathbf{r},t)$ at the defined time delay $\tau = 0$.

Principles of a cross-correlated imaging technique

The technique of cross-correlated (C^2) imaging is based on a principle of low-coherence interferometry (LCI) or white light interferometry (WLI). Here information about physical quantities of interest is extracted with regard to the change of an OPD of two interfering beams [75]. In the case of the C^2 imaging the set-up is based on a MZI. The general scheme of the set-up is depicted in Figure 3.2. Light beams from a light source are divided into both arms of the interferometer. Light in the sample arm is coupled into the FUT, where several modes propagate. By a delay line in the reference arm an optical path length (OPL) of the reference beam is changed, until it matches the OPL of the desired mode in the FUT. After recombination on a beam splitter, beams are directed onto the camera, that takes pictures of interacting beams at each step of the

delay line displacement. An interferogram is obtained from the set of interference pictures, represented as a change of intensity recorded by the camera depending on the time delay introduced by the delay line in the reference arm. It contains information about the fibre modal content. The interference pattern consists of a set of fringes, that appear when OPDs between the specific modes in the FUT and the FM in the reference fibre are less than the coherence length l_c of the source. The interference intensity reaches its maximum, when the values of OPD is close to zero. Positions of those maxima correspond to the positions of every specific mode at the line of time delays gained by the delay line. Determining the time delay of HOMs relative to the FM the differential modal time delays can be found. The intensity distribution of each picture, taken by the camera along the entire range of the time-delays, is composed from two terms: a background intensity $I_0(x,y)$ and an interference intensity $I_{Int}(x,y,\tau)$.

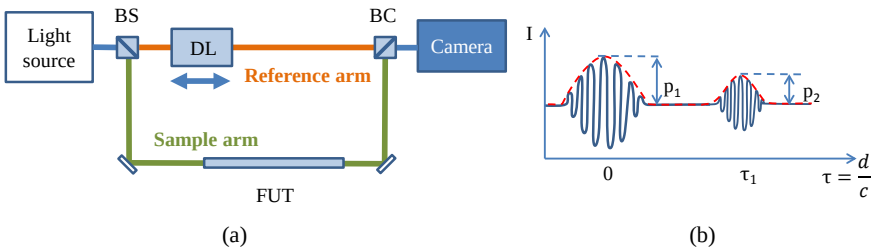

Fig. 3.2 (a) The scheme of the set-up is presented as an unbalanced Mach-Zehnder interferometer. BS and BC are a beam splitter and a beam combiner, FUT is a fibre under test and DL is a delay line. (b) An example of the cross-correlated trace, where the intensity recorded by a camera is represented as function of the time-delay τ.

$$I = I_0(x,y) + I_{Int}(x,y,\tau) \tag{3.11}$$

where (x,y) are positions of pixels in a picture, $I_0(x,y)$ is the background intensity, which is a sum of the intensities radiated from the reference and the sample arms. The background intensity for the collimated beams does not depend on the time delay τ.

$$I_0 = I_r(x,y) + I_s(x,y) \tag{3.12}$$

$I_r(x,y)$ and $I_s(x,y)$ are taken by the camera, when only one of the beams is pointed at the camera, and another one is blocked. The interference intensity $I_{Int}(x,y,\tau)$ is presented through the cross-correlation function $c_{rm}(\tau-\tau_m)$ (derived in the previous section as $g_{12}(\mathbf{r},\tau)$):

$$I_{Int}(x,y,\tau) = \sum_m 2\sqrt{I_r(x,y)I_m(x,y)}\alpha_m |c_{rm}(\tau-\tau_m)|\cos(\Psi) \tag{3.13}$$

The cross-correlated function $c_{rm}(t)$ is related to the spectral density $S_{rm}(\Omega)$ through Fourier transform as [12]

$$c_{rm}(t) = \frac{1}{2\pi}\int S_{rm}(\Omega) exp(-i\Omega t)\mathrm{d}\Omega, \tag{3.14}$$

where

$$S_{rm}(\Omega) = S(\Omega) exp(i\Delta\phi_{mr}) \tag{3.15}$$

In Eq.(3.13), α_m is the real modal weight, τ_m is the relative time delay between the FM and the definite HOM in the FUT, $|c_{rm}(\tau-\tau_m)|$ is the modulus of the cross-correlation function, Ψ is a linear phase that describes the fast oscillation behaviour and the phase mismatch between the two arms of the interferometer. Equations (3.14),(3.15) express the dependence of the cross-correlation function on the spectrum of the input light source $S(\Omega)$ and the residual dispersion mismatch between two arms of the interferometer $\Delta\phi_{mr}(\Omega)$, which is equal[7] to:

$$\Delta\phi_{mr}(\Omega) = \sum_{k\geqslant 2} \left(\beta_m^{(k)} L - \beta_r^{(k)} L_r\right) \Omega^k / k! \tag{3.16}$$

Here, $\beta_m^{(k)}$ and $\beta_r^{(k)}$ are the coefficients of the Taylor expansion derived for the propagation constant β of the FUT and reference fibre of the corresponding lengths L and L_r. Frequency Ω is a shifted frequency corresponding to a central frequency ω_0.

$$\Omega = \omega - \omega_0 \tag{3.17}$$

Equations (3.13)-(3.16) constitute the basis of the data analysis of the C^2 method and were derived in Ref.[7, 93]. The modulus of the cross-correlation function $|c_{mr}(\tau - \tau_m)|$ describes an envelope of the intensity oscillation and represents the cross-correlation trace (C^2 imaging trace, red curve in Figure 3.2(b)). Analysing a stack of images, acquired by the camera, at every pixel at each step of the delay line d, extracting the background intensity I_0 and normalizing to the intensity of the reference beam, one obtains the cross-correlation signal $\mathscr{P}(\mathbf{r}, \tau)$:

$$\mathscr{P}(\mathbf{r}, \tau) = \sum_m \alpha_m^2 |c_{rm}(\tau - \tau_m)| I_m(\mathbf{r}) \tag{3.18}$$

that encodes information about the modal weight $p_m = \alpha_m^2$, the modal intensity $I_m(\mathbf{r})$ and the differential time delay (DTD) between modes τ_m. The number of peaks at the cross-correlated trace obtained from the recorded interferograms, schematically described in Figure 3.2(b), corresponds to the quantity of modes that propagate in the FUT. The amplitude of peak defines the modal weight, while the position of each peak is interpreted as a differential modal time delay τ_m of the specific mode m relative to the FM. Integrating the interference signal $\mathscr{P}(\mathbf{r}, \tau)$ over a definite extent at time over each pixel on the imaging plane, the intensity distribution of each mode I_m can be decomposed.

Decomposition of modal content with 2D Fourier transform

The concept of interferogram analysis employing the Fourier transform is widely known within the fields of speckle interferometry [63, 29] and holography[70, 30]. The basis of the current approach of fringe-pattern analysis was reported in 1982 by Mitsuo Takeda [101]. Following its procedure a phase map is extracted from a single recorded interferogram that was Fourier transformed and undesired terms were isolated, while the required side-band is shifted and centred at zero frequency. The phase map is picked up, when derived term is inverse Fourier transformed.

This subsection will demonstrate that an approach of a two-dimensional Fourier transform (2D FT) can be implemented as an alternative for the modal reconstruction in the C^2 method. In this case, the modal intensity and phase distribution can be extracted from interferograms recorded by a CCD camera following the procedure of a fringe pattern analysis.

The spatial intensity distribution of the fringe pattern is expressed in the form [42]:

$$I(x,y) = I_0(x,y) + m(x,y)cos[2\pi f_0 x + \phi(x,y)] \tag{3.19}$$

where $\phi(x,y)$ is the phase of interest, $I_0(x,y)$ is the background intensity distribution and $m(x,y)$ is a contrast function, x and y is a position of pixels on the imaging plane, f_0 is a spatial carrier frequency along x direction, that is proportional to the angle θ, introduced between two interfering beams, and in the case of small angle can be expressed as:

$$f_0 = k_1 - k_2 \approx k_0(\theta_1 - \theta_2) = k_0\theta, \tag{3.20}$$

where k_1, k_2 are the wave numbers of the corresponding interfering beams, θ is an introduced angle between beams.

Following complex notation, Eq. (3.19) can be rewritten as:

$$I(x,y) = I_0(x,y) + c(x,y)e^{2\pi i f_0 x} + c^*(x,y)e^{-2\pi i f_0 x}, \tag{3.21}$$

where

$$c(x,y) = \frac{1}{2} m(x,y) e^{i\phi(x,y)} \tag{3.22}$$

Applying the 2D FT to Eq. (3.21) with respect to x one obtains:

$$I(f_x,f_y) = I_0(f_x,f_y) + C(f_x - f_0, f_y) + C^*(f_x + f_0, f_y), \tag{3.23}$$

where $I_0(f_x,f_y)$, $C(f_x - f_0, f_y)$ and $C^*(f_x + f_0, f_y)$ are spatial Fourier spectra separated by the carrier frequency f_0 from each other. $C(f_x + f_0, f_y)$ and $I_0(f_x,f_y)$ can be removed by using a filter centred at f_0. In this case, the larger angle between the interfering beams, the larger f_0 and the more separate the spatial Fourier spectra in reciprocal space are. Shifting $C(f_x - f_0, f_y)$ to the origin $C(f_x,f_y)$, the carrier frequency f_0 is eliminated. Employing the inverse Fourier transform to $C(f_x,f_y)$ with respect to f_x, $c(x,y)$ is derived, from which the phase $\phi(x,y)$ can be extracted.

The described approach can easily be implemented for the modal content analysis by the C^2 imaging technique. To obtain the fringe pattern at the camera plane at the output of the interferometer an angle has to be introduced between beams from the reference and the sample arms. The created fringes are described by Eq. (3.13), derived in the previous section. The fact that the beams from reference and sample arms interfere at the camera plane after travelling with a relative angle between them, introduces an extra linear phase term that is added to Ψ in the cosine in Eq. (3.13). It is important to mention, that the angle between the beams (and therefore the extra linear phase term) is known by the experimentalist and is completely under her/his control.

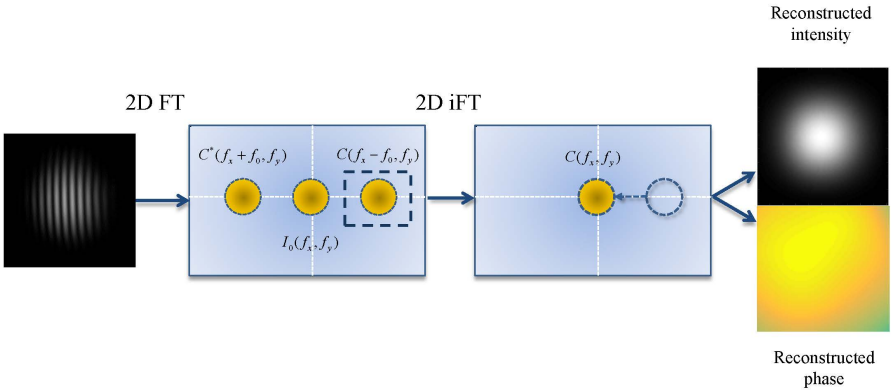

Fig. 3.3 The scheme of the 2D FT analysis of the fibre modal content.

To characterise a fibre modal content by the 2D FT, have to be used the interferograms at the time $\tau = \tau_m$, that corresponds to the maxima of interference peaks at the C^2 trace. In all presented experimental results further in the thesis, each of the collected fringe patterns is analysed following the aforesaid method. The scheme of analysis is described in Figure 3.3. At the beginning the background intensity $I_0(x,y)$ and intensity distribution of the reference beam $I_r(x,y)$ is filtered by 2D FT. The outcome term $c(x,y)$ contains information about the modal intensity distribution in its real part and the modal phase distribution encoded into the phase angle of $c(x,y)$. Applying the phase unwrapping algorithm, the phase distribution of the corresponding mode can be extracted.

3.2 Experimental results

3.2.1 The C^2 characterisation based on a visibility of interference

Figure 3.4 presents a scheme of experimental set-up based on a Mach-Zehnder interferometer (MZI) and applied for the modal characterisation by the C^2 method based on a visibility of interference. A broadband supercontinuum laser (*SuperK COMPACT, NKT Photonics*), that emits light within a range of wavelengths from 450nm to 2400nm, is used as a light source. A fibre coupler, introduced after the source, equally splits incoming light into the reference and test arms. The spectrum of the source is filtered by a bandpass filter at the input of the set-up. The reference arm consists of 1m of the single mode reference fibre 780-HP (*Nufern* [67]) with the cut-off wavelength around 730nm, and a delay line, that adjusts an optical path of the FM in the reference arm corresponding to a defined mode in the FUT. The test arm contains an unit of mechanically induced gratings (MIG) for the higher-order modes (HOMs) excitation, as it was described in Section 2.6. A polarisation controller is inserted before the MIG unit to optimize polarisation of the coupled modes and to select LP_{11} only in one polarisation. As the FUT is chosen 1m of SMF28 (*Corning* [19]). It is a single mode fibre with the cutoff wavelength around 1260nm, the core diameter of 8.2μm and numerical aperture being 0.14. During the experiment, LP_{11} is excited directly in the FUT. The first 75cm of the FUT is inserted into the polariser controller and the MIG unit, while the active length of the fibre, from a point where the HOM is excited by the gratings to the end facet of the fibre, is 25cm. The final state of the output light polarisation in both arms is controlled by a linear polarisers. Between the reference and test beams is deliberately introduced an angle. After a recombination of the beams on a beam splitter at the output of the setup,

they produce interference fringes, that are captured by a camera (8bit *Point Grey*, maximum frame rate 120fps). The optical path length (OPL) of the beam in the reference arm is adjusted by the delay line to match the OPL of modes from the FUT at the time delays $\tau = \tau_{mr}$ [Eq.(3.24)].

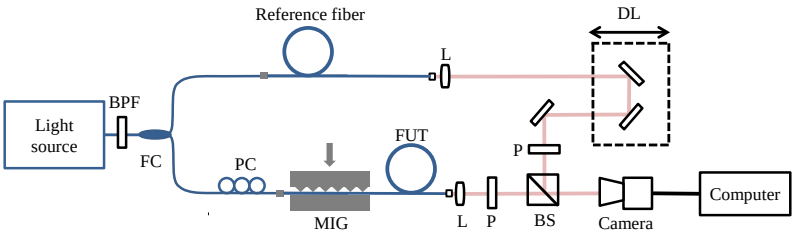

Fig. 3.4 A scheme of the C^2 set-up, where LP_{11} mode is deliberately excited by a mechanically induced gratings. Here, abbreviations denote: BPF - a bandpass filter, FC - a fibre coupler, PC - a polarisation controller, MIG - a mechanically induced grating unit, FUT - the fibre under test, L - a lens, P - a polariser, DL - a delay line, BS - a beam splitter.

According to results of the fibre simulation, at the wavelength of 850nm the FUT supports only two groups of modes: LP_{01} and LP_{11}. A dependence of numerically calculated effective indices on wavelength is depicted in Figure 3.5. By dashed lines are marked the refractive indices of the core and cladding, which are assumed to be constant over a range of wavelengths from 0.8μm to 1.3μm and equal correspondingly to $n_c = 1.452$ and $n_{cl} = 1.4468$. Values of the indices are chosen to fit the specification parameter $dn = 0.36\%$. It is also worth mentioning, that in the specification is given the cable cutoff wavelength, that is blueshifted comparing to the bare fibre cutoff wavelength.The effective refractive indices of the modes were calculated from Eq.(2.14) and (2.16). The

group velocities and the group propagation time of the modes were derived from Eq.(2.19) and (2.20). The differential time delay (DTD) is found according to Ref.[7, 93] as

$$\tau_{mr} = \frac{L}{\upsilon_m} - \frac{L_r}{\upsilon_r}, \tag{3.24}$$

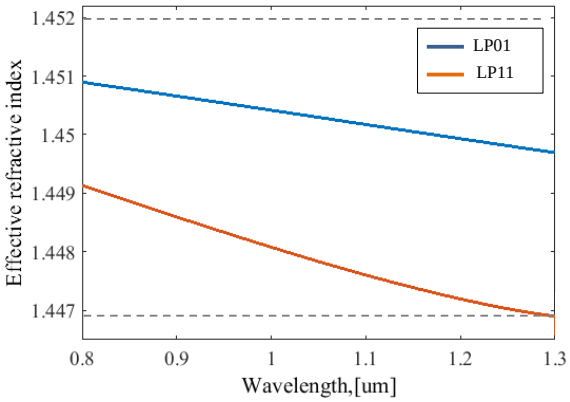

Fig. 3.5 Numerically calculated effective indices of LP_{01} and LP_{11}.

where L and L_r are lengths of the FUT and reference fibre, and υ_m and υ_r are the group velocities of the corresponding mode in the FUT and the FM in the reference fibre.

During the experiment LP_{01} is converted into LP_{11} mode at the wavelength of 850nm by the MIG unit with a period of 532μm. In order to confirm a presence of the excited HOM and to check a conversion efficiency, the FUT is spliced with a fibre (780-HP), which is single-mode at 850nm. A transmission spectrum is measured by an OSA. With an increase of pressure at the MIG unit, a depth of notch grows. Figure 3.6(a) shows, that for LP_{11} can be reached a conversion efficiency more

than -20dB, determined as a depth of notch depicted by a red curve. However, when a critical value of the induced stress is reached, an over-coupling occurs [10], that forces LP_{11} to couple back into LP_{01}, resulting in a decrease of the resonant peak at the transmission spectrum with an increase of pressure [Figure 3.6(b)] .

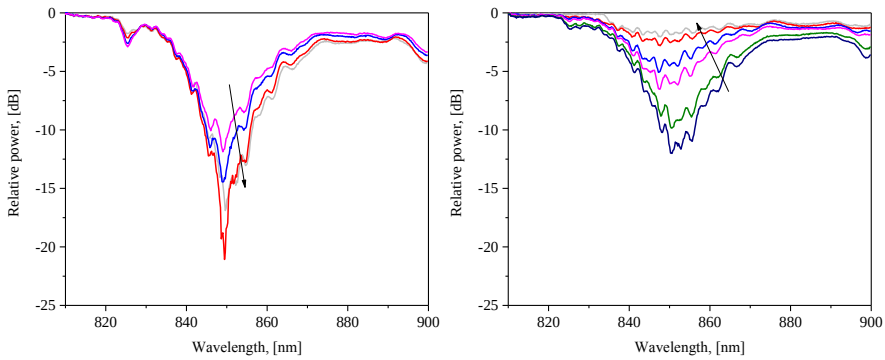

Fig. 3.6 The transmission spectra of the conversion from LP_{01} to LP_{11}. (a) With increase of pressure, the conversion efficiency grows. However, at some level of pressure overcoupling occurs, and LP_{11} gradually couples back to LP_{01} resulting in decrease of attenuation at the resonant wavelength (b).

As it was described in Section 3.1, information about a quantity of modes in the FUT can be extracted from the interferograms, captured by the camera along a range of the time delays governed by the delay line. Since fibre modes propagate with different group velocities along a fibre, each of them has its own delay time. When an angle is introduced between the beams from the reference and test arms and the OPLs in the both arms of MZI for propagating modes are equal, interference fringes of a high contrast appear. A strength of interference in this

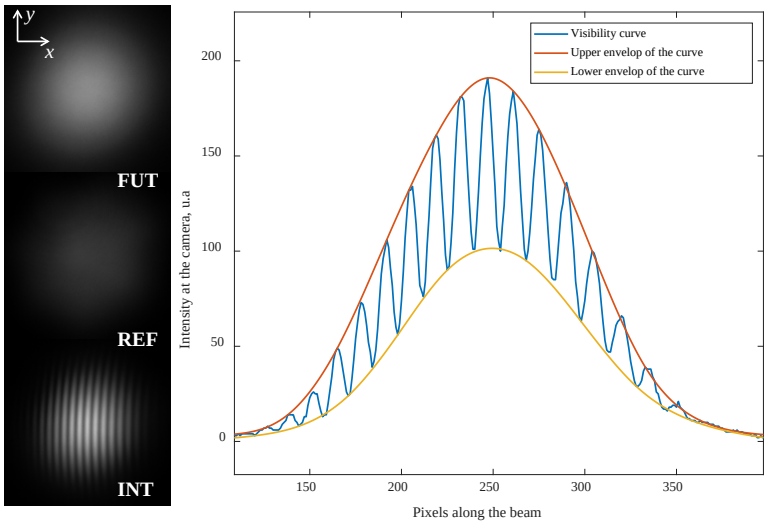

Fig. 3.7 A distribution of the pixels intensity at the the center of interfering beams along x-direction. At the insets are depicted the intensities of the reference (REF), test (FUT) and interfering (INT) beams.

case can be evaluated by the fringe visibility, that is also proportional to the normalized cross-correlation function. Therefore, fibre modal content can be characterised as well by the visibility, derived from Eq.(3.10). Analysing the visibility along the scanning time delays, a visibility trace can be obtain. Likewise the C^2 trace, the visibility trace describes a change of intensity with a time delay and reveals a quantity of propagating modes, that appear as separated peaks at the trace at time delays $\tau = \tau_{mr}$ and with amplitudes corresponding to modal powers. When the OPLs of the two interfering modes are equal, the fringe pattern possesses the strongest contrast and the highest visibility as well. As a difference in the OPLs grows, the visibility decreases gradually reaching zero.

To evaluate the interference with a help of the fringe visibility two output beams are aligned and focused at the camera. LP_{11} is not excited in the FUT and, when the OPL for the FMs in both arms of the interferometer are equal, at the camera is seen an interference pattern,

with a spatial frequency of fringes proportional to the angle between two beams [Eq.(3.20)]. Figure 3.7 demonstrates the reference (REF) and test (FUT) beams focused at the camera and the interference pattern of the interfering FMs (INT). The visibility trace depicted in Figure 3.7 is measured in the center of the image. It changes in a harmonic manner with clear maximum and minimum values. The visibility is calculated from Eq.(3.10), where a maximum intensity I_{max} is derived as a maximum of the upper envelope and a minimum intensity I_{min} is a maximum of the lower envelop. The total visibility of the image is derived as an average of visibilities along y-direction.

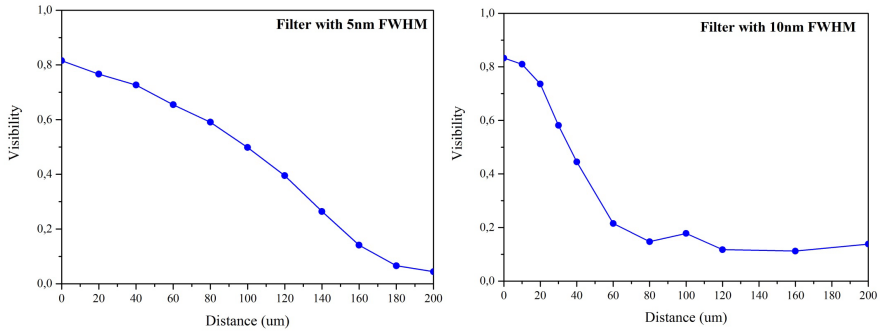

Fig. 3.8 The visibility trace measured for two bandpass filters of FHMW equal to 4nm and 10nm.

The FWHM of the modal peaks at the visibility trace is determined by the coherence time and coherence length of the light source. To analyse the aforementioned dependence, an influence of the light source bandwidth on the visibility trace is analysed by performing measurements for two different input conditions. In the first case, a spectrum of the seed source is filtered by a bandpass filter with FWHM of 5nm, in another, with FWHM of 10nm. Figures 3.8(a) and (b) present the visi-

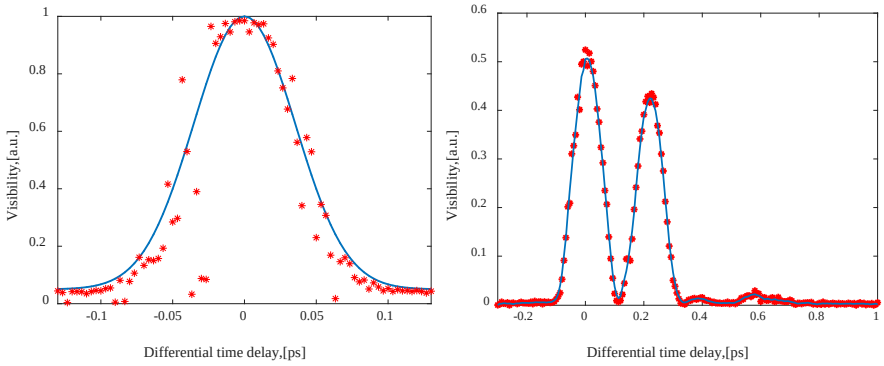

(a) (b)

Fig. 3.9 (a) A visibility trace measured without HOMs excitation and (b) when LP_{11} is excited by the MIG unit.

bility as a function of the optical path difference in μm for the different bandpass filters. For a narrow bandwidth of the spectrum [Figure 3.8(a)] the visibility trace is broad, preserving a good contrast of the interferograms along most of the scanning length. At the same time, when the bandwidth of the incoming light spectrum is larger, the coherence length is smaller and the width the peak at the trace shrinks correspondingly. However, the temporal resolution of the systems is governed not only by the coherence time of the source, but also by the dispersive broadening that will be discussed further below in this chapter. The trace, measured with a broader filter possesses higher temporal resolution and consequentially, analysing it, more features can be resolved than, for example, for the trace depicted in Figure 3.8(a). For the further measurements is chosen the bandpass filter with the FWHM of 10nm. Worth to mention, that a small peak at the distance of 100μm at the trace is present due to steep edges of the filtered spectrum.

Figure 3.9 represents two measurements made under different excitation conditions. Figure 3.9 (a) shows an example of the visibility trace measured with 10nm bandpass filter and a time delay step of 0.003ps

without HOM being excited, while Figure 3.9(b) demonstrates the results of measurement when in the test arm is excited LP_{11} with the efficiency conversion of -12dB (depicted as a pink line in Figure 3.6(a)). Two peaks at the trace in Figure 3.9(b) correspond to the FM and LP_{11} delayed by 0.22ps.

Obtained results shows, that a general information about propagating fibre modes, like their quantity and intermodal delays, can be evaluated based on the visibility. It worth mentioning, that the relative power of LP_{11} and its conversion efficiency were not in the perfect agreement. Therefore, an additional investigation of a correlation between a relative modal power and a peak amplitude at the visibility trace is required. Despite of this, the visibility allowed to investigate an important dependency of the C^2 temporal resolution on the bandwidth of the input light source. Further in a research for the C^2 trace determination is mainly used an approach described in Ref.[7, 93].

3.2.2 Flexible C^2 imaging

Description of approach for the flexible C^2 imaging

Dispersion has a crucial importance for the temporal resolution of all interferometric imaging techniques, especially when broadband sources are used as input light sources. It arises from the dependence of the propagation constant on the frequency when light propagates in a dispersive medium, as a fiber. An important aspect of C^2 imaging is the ability to balance dispersion, minimizing its influence on results of measurements. It is achieved by the careful matching of the reference fiber and the FUT in the following way [7]:

$$L_r = \frac{\beta_m^{(2)}}{\beta_r^{(2)}} L \tag{3.25}$$

where L_r and L are the lengths of the reference fibre and the FUT, $\beta_r^{(2)}$ and $\beta_m^{(2)}$ are the second-order coefficients of a Taylor expansion of the mode propagation constant β around the central frequency ω_0. It is worth mentioning that the group-velocity dispersion (GVD) is precisely matched for the FM in the FUT, while HOMs are still affected by the residual dispersion that leads to broadening of the modal peaks at the C^2 imaging trace. Another important parameter that has to be taken into account is the spectral bandwidth of the input light source. To reach a high temporal resolution for C^2 imaging an optimal spectral width of the light source has to be chosen.

As it was described previously, Eq. (3.14-3.15) shows the correlation between the C^2 trace appearance and the group-delay dispersion $\Delta\phi_{mr}(\Omega)$ as well as the input spectrum $S(\Omega)$. The last two parameters determine the temporal resolution of the cross-correlation trace.

When the influence of dispersion is minimized ($\Delta\phi_{mr} \approx 0$) the temporal resolution of the system is mainly governed by the coherence time of the light source $\Delta\tau_{FWHM}^{coher} = 8 \cdot ln(2)/\Delta\Omega$, where $\Delta\Omega$ is the FWHM of the input pulse and $\Delta\tau_{FWHM}$ is the FWHM of the interference peak at the imaging trace. In this case, an increase of the spectral bandwidth for the seed source allows to obtain a better temporal resolution. On the other hand, if the interferometer is not balanced and the residual GVD is large, the temporal resolution is affected by dispersive broadening $\Delta\tau_{FWHM}^{disp} = \Delta\phi_{mr}(\Omega) \cdot \Delta\Omega$ and increase of the spectral bandwidth causes degradation of the resolution. However, to cancel dispersion completely for all modes simultaneously is impossible, consequently a compromise between the residual dispersion and a spectrum width has to be found. Furthermore, between the spectral shape and the shape of the C^2 imaging trace exists a direct dependence as well. The smooth bell-shaped (Gaussian shape) spectrum leads to the smooth cross-correlation trace, while the steep edges in the spectrum, for example, caused by implementation of a bandpass filter result in artefacts at the imaging trace around

interference peaks that affects the data analysis. Therefore, deliberate selection of an appropriate bandwidth of the seed source and the set-up components are a high concern for the C^2 imaging technique.

The scheme of the set-up for the flexible cross-correlated imaging is shown in Figure 3.10. As a light source we used the supercontinuum laser *SuperK EXTREME*, the output of which was filtered by a multi-line tunable filter *SuperK Select*, both produced by *NKT Photonics*. *SuperK EXTREME* emits light within the range of wavelengths from 400nm to 2400nm, while *SuperK Select* scans along the near infrared wavelengths from 800nm to 1400nm with filter bandwidth of approximately 7.23nm. An aforesaid spectral width corresponds to one excited channel of *SuperK Select* or in other words, one excited beam with a central wavelength deliberately chosen along the range of scanned wavelengths. The measured spectrum of one beam at the central wavelength of 1050nm is depicted in Figure 3.11 and has a characteristic sinc-shape. *SuperK Select* and *SuperK EXTREME* are independent products of *NKT Photonics* and additional information can be found in [72, 73, 71]. The principle of operation of *SuperK EXTREME* is based on a supercontinua generation that is formed when a photonic crystal fibre is pumped by a ps 1064nm laser at wavelength close to zero dispersion wavelength, while *Super Select* is an acousto-optic tunable filter, principle of operation of which is based on an acousto-optic diffraction in an optically anisotropic medium.

One of the powerful features of *SuperK Select* in combination with *SuperK EXTREME* is an opportunity to add up to 8 emitting channels at the output increasing in this way the spectral bandwidth of the seed source at the input of the C^2 set-up. The power of each channel of *SuperK Select* can be individually controlled and modified. In Figure 3.11, for instance, the beam power was adjusted to 30% of the maximum power, that results in the sidelobes suppression up to -10dB in comparison with the main peak. Power modulation allows shaping of the input spectrum

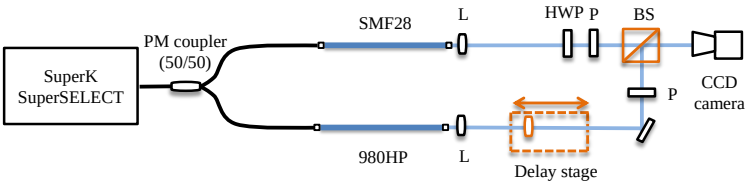

Fig. 3.10 A scheme of the set-up for the flexible C^2 imaging. Here, L is a lens, HWP - a half-wave plate, P - a polariser, BS - a beams splitter, CCD - a camera.

in any desired way. The tunable spectral width together with adjustable spectral shape, create a unique opportunity for optimization of the C^2 imaging method making it a flexible diagnostic tool with a high degree of variability of parameters that can easily be adjusted for the measurement of fibres with particular designs.

Demonstration of the method

To demonstrate a flexibility and simplicity of the method is chosen a standard step-index fiber SMF28 of 1m length as the FUT, that was balanced by the same length of a single mode fiber 980HP (*Nufern* [68]) as a reference fiber. Operational wavelengths, chosen for the measurement, are from 870nm to 1090nm. Current selection of wavelengths is determined by an operational window of the set-up components. As it was described previously, up to wavelength of 1300nm the FUT is considered as a few-mode fiber, where only the FM and the first HOM group are supported. Numerical simulation confirms presence of two modal groups along the entire range of wavelengths of interest. Dependence of

the effective refractive indices for LP_{01} and LP_{11} versus wavelength is shown in Figure 3.5.

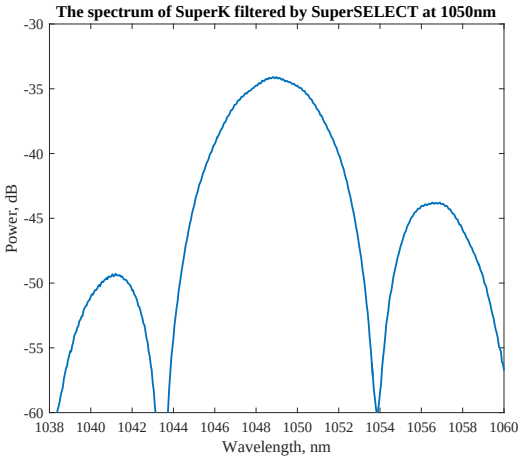

Fig. 3.11 The output spectrum of SuperK filtered by SuperSELECT at 1050nm, when the only one channel is turned on.

To investigate an influence of the spectral shape and width on the temporal resolution and appearance of the C^2 imaging trace was performed a set of measurements of SMF28 with diverse input spectra from the seed source. Combinations of the merged input beams and their total FWHM are presented in Table 3.1.

Table 3.1 Combination of beams from *SuperSELECT* used in the measurements.

Number of beams	Wavelengths, nm	Spectral width, nm
1	1050	7.23
2	1040-1050	4 and 5
2	1045-1050	9
3	1045-1050-1055	14
5	1042-1046-1050-1054-1058	16.93
8	1042-1045-1048-1050-1052-1055-1058-1061	28.25

Thus, spectra created from 1, 2, 3,5 and 8 beams were used. Figure 3.12(a) demonstrates selected spectra taken at the wavelength of 1050nm. Wavelength of the characteristic peak at 1064nm corresponds to the wavelength of the laser pump. Spectra, that include the wavelength of the pump peak, can be affected by its power, but when the level of the pump peak is sufficiently suppressed it does not corrupt the shape of the total spectrum and hence it does not affect the imaging trace. It is also worth taking into account that excitation of the beams in close proximity to each other (less than 4nm between channels) especially close to the pump peak wavelength introduces noise between the channels that originated from the RF signal from the RF drive that powers *SuperSelect*. The noise is clearly seen at the spectrum of 8 beams at 1050nm [Figure 3.12(b)]. Moving to the shorter wavelengths the influence of the pump peak as well as fluctuation in the spectrum is reduced, for example, the same beam combination at 890nm [Figure 3.12(b)] experiences lower interaction noise between the channels than at 1050nm.

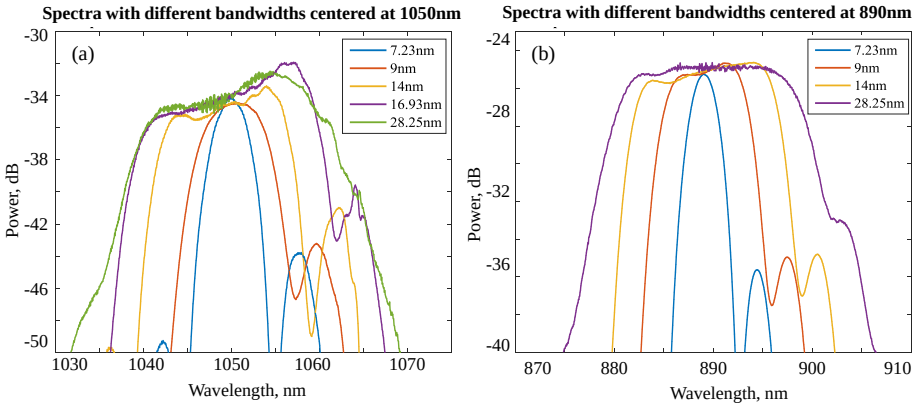

Fig. 3.12 The output spectrum of *SuperK* filtered by *SuperSELECT* with different FWHM centered at 1050nm (a) and 890nm (b).

During the experiments the input spectral width was varied from 7.23nm to 28.25nm. Dependence of the temporal resolution on the spectral width is presented in Figure 3.13. Here the blue curve corresponds to

the calculated values and the red one to the temporal resolution obtained during the measurements as a full-width half maximum of the interference peak for LP_{01} at the C^2 trace. For the input spectrum merged from 8 beams the measured temporal resolution is 0.15ps and the calculated value is 0.154ps, while for the spectrum of 1 beam, presented in Figure 3.11, the predicted value is 0.465ps and the measured is 0.47ps. In Figure 3.14 two C^2 imaging traces are depicted measured at 1050nm with the highest and the lowest temporal resolution.

An example of the spectral shape influence on the C^2 trace appearance is shown in Figure 3.15, where the input spectrum was combined from 2 channels with spectra centred at the wavelengths of 1040nm and 1050nm. Individual spectra of each channel resembles in the shape the spectrum depicted in Figure 3.11, while the spectral shape of two combined channels with separation of 10nm is shown as inset in Figure 3.15. Due to the split shape of the resultant spectrum of the two joined channels, the interference peaks acquire characteristic sinc-shape with strong undesirable sidelobes. Consequently, the the combined spectrum from channels with separation of the central wavelengths larger than the FWHM of the single channel, here more than 7nm, results in artefacts on the imaging trace in the form of the sidelobes around each interference peak.

During the measurements the delay line was programmed to scan with an increment of 5μm that corresponds to 16fs of the time delay along 1mm distance. Such incremental step and scanning distance allow us to resolve LP_{01} and LP_{11} at the C^2 trace along the entire range of chosen wavelengths and for the all selected spectra. The first order HOM is excited in the FUT by positioning the input beam relative to the fiber core, so the input coupling condition is changed and light power is distributed between the FM and the HOMs. At the beginning two modes were detected at 1050nm with the modal power close to 60% and 40% corresponding to LP_{01} and LP_{11} [Figure 3.14]. Detected modal power

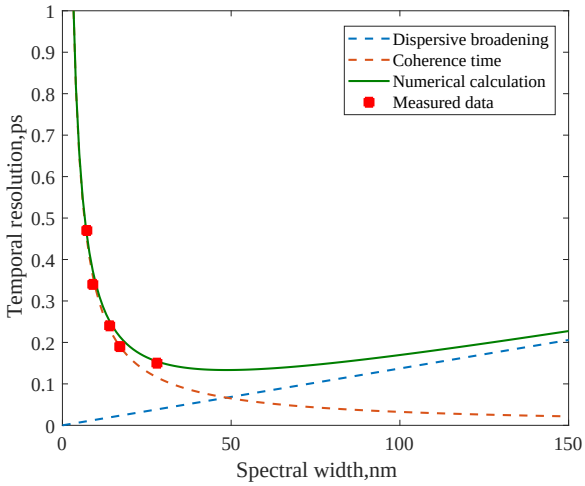

Fig. 3.13 Temporal resolution governed by dispersive broadening and coherence time as function of the FWHM of spectrum at the wavelength of 1050nm. By green line is depicted total numerically calculated resolution of the set-up. By the red dots are marked the measured values.

demonstrates one of the advantages of the C^2 imaging method to reveal the modes with equal or close to equal modal power.The positions of the peaks on the trace specify the temporal delay of HOM with respect to the FM. At wavelength of 1050nm measured the DTD between modes is -2ps/m, while the predicted value is -1.92ps/m. At the range of wavelengths from 870nm and up to its cutoff, LP_{11} propagates faster than LP_{01} due to higher group velocity, and during the measurements it comes out as a first arriving mode at the C^2 trace. Expected turn around point in the group velocities of the modes is around 870nm. To investigate modal behaviour at shorter wavelength tuned input spectrum merged of 8 channels were implemented further for the C^2 characterization of the fibre modal content.

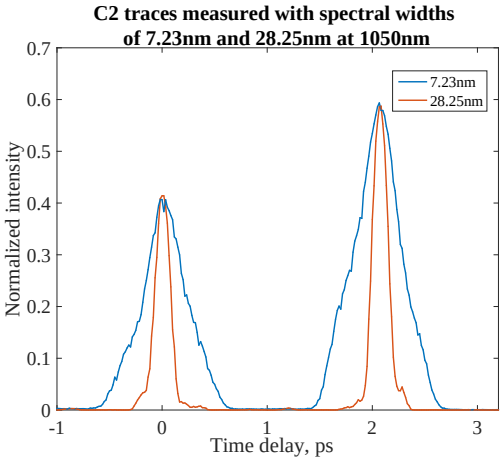

Fig. 3.14 Comparison of the C^2 traces measured with the spectral bandwidths of 7.23nm (blue line) and 28.25nm (red line) at the wavelength of 1050nm.

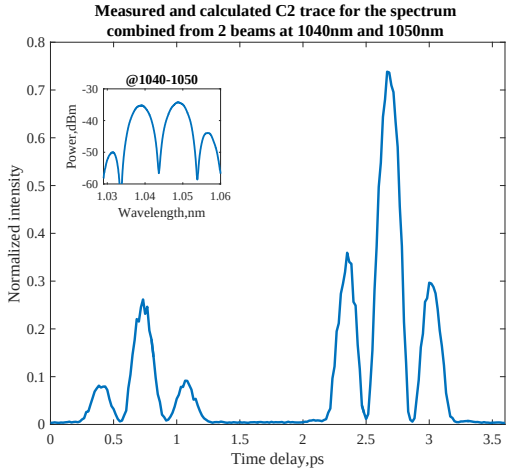

Fig. 3.15 The measured C^2 trace for the spectrum combined with 2 beams at the central wavelengths of 1040nm and 1050nm. At the inset is depicted the input spectrum.

3.2.3 Characterisation of a step-index fibre (SMF28) by the flexible C^2 imaging

As it was shown in the previous section an unique feature of the set-up for the flexible cross-correlated imaging is an opportunity to perform measurements at any desired wavelength from 870nm to 1090nm due to implementation of the broadband light source (*SuperK*) in combination with the tunable filter (*SuperSELECT*). The 8-beams spectrum described in Table 3.1 with power in each channel 60%-80%-100%-90%-90%-70%-50%-30% and shown in [Figure 3.12(a)] as a green curve is translated to central wavelengths 870nm, 930nm, 970nm, 1030nm, 1050nm and 1090nm and used for estimation of the SMF28 modal contents. From the C^2 traces recorded at the aforesaid wavelengths is extracted the DTD between LP_{01} and LP_{11} that is presented in Figure 5.8 as a function of wavelength.

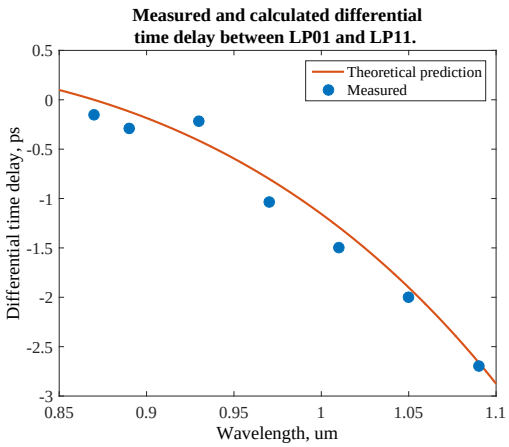

Fig. 3.16 Calculated and measured DTD between LP_{01} and LP_{11} propagating in the FUT.

Red curve is a calculated estimation, while blue dots are the measured data. As it can be seen, experimental and measured values are in a good

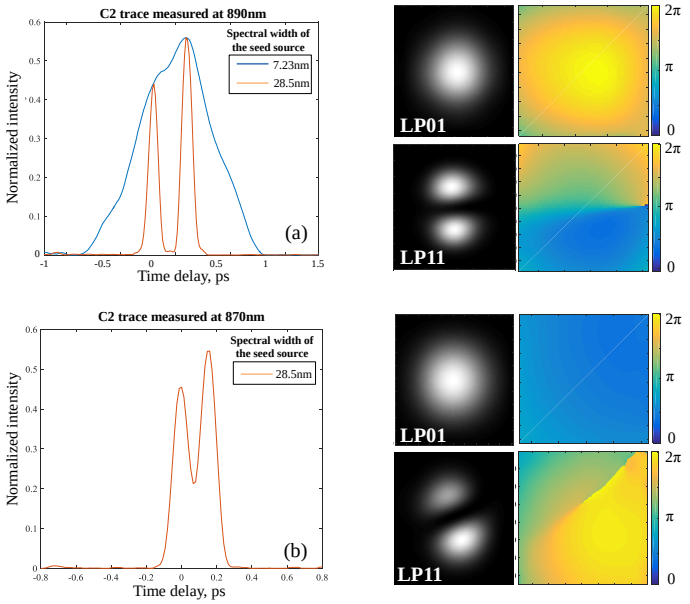

Fig. 3.17 The C^2 trace recorded at the central wavelength of 890nm (a) with spectral widths of 7.23nm (blue line) and 28.25nm (red line) and 870nm (b) with spectral width of 28.25nm (red line). As wavelength varied the relative modal power is maintained to be kept constant. Insets on the right side represent reconstructed modal intensity profiles of LP_{01} and LP_{11} at the maxima of the interference peaks and corresponding phase distributions zoomed in the area of interest.

agreement. It is noticeable how the DTD between two modes decreases approaching zero value at wavelength close to 870nm. Down to 930nm an intermodal time delay between detected modes is large enough to resolve them even with the smallest input spectrum bandwidth of 7.23nm, while approaching the turn-around point it is beneficial to increase the temporal resolution of the system to the maximum using the widest bandwidth of 28.25nm. The imaging traces taken for the two extreme bandwidths of the input spectrum at the central wavelength of 890nm are demonstrated in [Figure 3.17(a)]. The recorded C^2 trace with a narrow input spectrum of 7.23nm, that consists of 1 beam, has lower temporal

resolution and at 890nm it is already impossible to resolve modes, since they coincide with one another [blue curve in Figure 3.17(a)].

The temporal resolution improvement of the imaging trace is reached by implementation of the input spectrum with a wider spectral bandwidth of 28.25nm. Measurement of the C^2 trace with 8 merged channels mentioned in Table 3.1 at 890nm gives clear identification of the propagating LP_{01} and LP_{11} modes. Moreover, the intensity profiles and the spatial phase profiles are extracted and depicted at the insets. LP_{01} has a characteristic flat phase distribution, while between the lobes of LP_{11} there is change close to π in the phase. Abrupt jump of 2π at the reconstructed phase distribution of LP_{11} at wavelength of 870nm is an artefact that appears due to the poor interferogram quality at that wavelength, since it is the edge of the operational window of the input fibre coupler, and the beams intensity distribution and power from the reference and the sampling arms are not the same.

With the optimized configuration of the set-up and the reached temporal resolution of 0.15ps we are able to resolve propagating modes at the wavelength of 870nm close to their turn around point. The cross-correlated trace recorded at 870nm is presented in [Figure 3.17(b)]. Here LP_{11} appears as a superimposed shoulder on LP_{01}. Two modes coincide with each other, nevertheless they can be decomposed. Intensity and phase profiles are depicted as the insets in [Figure 3.17(b)]. The sharp edge in the lower part of the extracted phase distribution of LP_{11} appears due to the error in the phase unwrapping. LP_{11} remains the fastest mode at the imaging trace at 870nm and still possesses higher group velocity than LP_{01}. The relative time delay between modes is -0.15ps. Results of the measurement show that the turn around wavelength for LP_{01} and LP_{11} in the SMF28 is lower than the calculated value. However, restriction of the operational wavelength window of the components in the C^2 set-up does not permit to go below 870nm. At the same time, the results of the C^2 imaging performed at wavelength of 850nm, described

in Section 3.2.1, shows that LP_{01} in the C^2 trace is already faster than LP_{11}. Therefore it could be assumed, that a crossing point for modes is around wavelength of 860nm. It has to be noted that the reference fibre at wavelengths shorter than 920±30nm also support HOMs, but any influence from them on the results of the measurements was not noticed.

3.2.4 Characterisation of fibres with advanced design by the C^2 imaging technique

In Section 2.5 was already briefly discussed a solid-core PCF. That type of fibres can be used as a key element for fibre-based lasers and amplifiers, development of which had been boosted after demonstration of a double clad approch [98]. The principle is based on design of the fibre with an inner and outer cladding, where pump light is coupled into the inner cladding, while the signal is coupled into the doped by the active materials (rare-earth dopants) fibre core. The energy of the pump is absorbed by an active material in the core that causes amplification of the propagating signal [47, 82]. One of the main limitations of the fibre laser systems is non-linear effects in a fibre that arises from interaction of high intensity light with a material. A common approach for reduction of the impact of high power intensities is an enlargement of the fibre core diameter. At the same time, it leads to appearance of HOMs in a fibre. However, while the refractive index contrast between the core and cladding is maintained small, a fibre will be still operating in a single-mode regime. As it was overviewed in Section 2.5 by adjusting the cladding parameters of a solid-core PCF one can design a large-mode area (LMA) PCF, operating in a single-mode (SM) regime over a definite range of wavelengths. To minimize influence of bending on the guided modes of large areas, the fibre has to be kept straight. An example, of

such design is AeroGAIN ROD fibre [74], experimental characteristic of which is under focus in this Section.

Physical parameters of the rod fibre

A microscope picture of the rod fibre cross-section is presented in Figure 3.18. AeroGAIN ROD fibre is a special type of LMA fibre known as a distributed mode filtering (DMF) rod fiber [74, 4, 48]. Due to unique design of the DMF rod fibre it has three regimes of operation: single mode (SM), multimode (MM) and leaky mode (LM) regime over a specific range of wavelengths. To ensure the single mode (SM) operation, in the cladding are introduced additionally doped multiple spatially localized elements arranged in a honeycomb-type of lattice [4], that are utilized as resonators to trap and confine the HOMs providing the SM operation over a certain range of wavelengths. While resonators maintain HOMs filtered out of the core, the air holes in the cladding allow to compensate uncertainties in the refractive indices of the core and cladding introduced during manufacturing. The geometrical parameters of the rod fibre are denoted in Table 3.2.

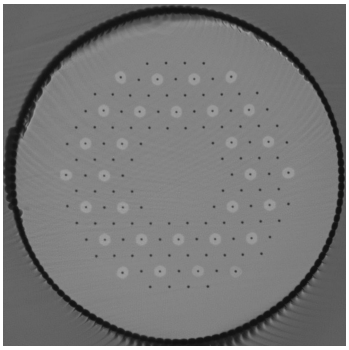

Fig. 3.18 The microscope image of the distributed modal filtering (DMF) rod fibre.

Table 3.2 The geometrical parameters of DMF rod fibre.

Dimensions	
Inner cladding diameter	269μm
d/Λ	0.103-0.106
Pitch	15.09-15.4
NA	0.58

When the rod fibre operates in the SM regime, the HOMs are leaking to the cladding, while the FM is confined by the core and propagates within it with a large fraction of the modal power. The rod is considered to be a single mode, when the fraction of power of the FM in the core exceeds 80%, while the fraction of the HOMs power is less than 50%. The DMF rod fibre becomes slightly multimode for wavelengths longer than the SM bandwidth, where the overlap of the HOM with the core gradually increases. On the other hand, for wavelengths shorter than the SM bandwidth, there is a small range of wavelengths where the FM experiences a drop in the power, due to coupling to the resonators in the inner cladding structure (LM regime). The aim of the current section is to demonstrate an advantage of the flexible cross-correlated method to distinguish all three operational regimes of the DMF rod fibre and the opportunity to tune the system in a desired manner according to the specific fiber design.

Measurement of the rod fibre with the flexible cross-correlated method

Investigation of modal regimes of the DMF rod fiber with the C^2 method was already performed by Laurila *et al.* in Ref.[52]. However, due to a light source, that was applied during the measurements, fixed at 1050nm, wavelength tuning was achieved by an angle-tunable bandpass filter, limiting flexibility of the modal analysis. As it was described in the

previous section, due to a tunable source, than can scan along a larger range of wavelengths, and opportunity to adjust the input spectrum shape and width, it is possible to reach much better flexibility for the analysis of all 3 regimes of operation of the DMF rod fibre. However, in the case of the rod fibre is very important to chose an optimal bandwidth and a spectral shape of the seed source to obtain a smooth C^2 trace and still to be able to resolve modes with a small intermodal delays. Otherwise, an overlap in wavelengths of the spectrum with the MM or LM regimes would affect results of measurements due to the HOMs, that originate from the MM or LM wavelength ranges. The DMF rod fibre under test is manufactured to be a single mode around 1064nm with a presumptive SM wavelength range from 1050nm to 1070nm. To derive an optimal condition for the rod fibre characterization an influence of the input spectral width on the temporal resolution and an overlap of the chosen spectra with LM and MM regimes were investigated. Figure 3.19 shows the input spectra merged from 1,3,5 and 7 beams at the central wavelength of 1060nm in a way as it was previously described in Section 3.2.2. Table 3.3 represents a relation between an input spectral bandwidth and corresponding temporal resolution of the C^2 trace, measured as FWHM of the peak. The schematic representation of the set-up is depicted in Figure 3.10 and as reference fibre is used a single-mode fibre 980-HP. During the measurement coupling was optimized for the FM, peak of which at the C^2 trace was normalized to the unity. At all C^2 traces is detected a HOM, that corresponds to LP_{02} , suppressed more than -20dB relative to the FM. The power level of the central beam is 50% of the total power, while the side beams were radiated with 25% of the power. In Figure 3.19 at the wavelength of 1064nm is clearly seen the characteristic peak, that corresponds to the pump. Its amplitude can be manually reduced by controlling the power level of beams excited at 1064nm or in close proximity to the aforesaid wavelength. From Table 3.3, it can be seen that with increase of the

Table 3.3 The dependence of the temporal resolution on the spectrum bandwidth for DMF rod fibre.

Spectral width,nm	**Wavelengths,nm**	**Temporal resolutio**
9.79	1060	0.73
19.69	1056-1060-1064	0.56
21.03	1054-1057-1060-1063-1066	0.41
24.86	1051-1054-1057-1060-1063-1066-1069	0.29

spectral bandwidth, the temporal resolution of the C^2 trace improves. Nevertheless, the best temporal resolution is achieved for the spectral bandwidth of 24.86nm, it was discarded due to the largest overlap outside the SM regime. The spectral bandwidth of 9.79nm was rejected due to the lowest temporal resolution. Among two other bandwidths of 19.69nm and 21.03nm, the former results in the lowest suppression of LP_{02}, that is close to -26dB. By this reason, all measurements along wavelength were performed with the spectral bandwidth of 19.69nm. A change of the chosen spectrum shape from 1040nm to 1090nm is shown in Figure 3.20. Being smooth at the shorter and longer wavelengths, the shape of the spectrum experiences alteration approaching the wavelength of 1064nm. Therefore, it is expected that aforesaid effect might have influence on the temporal resolution of a C^2 trace at 1064$\pm$5nm. It is also worth to mention, that the level of the beam power radiated around the pump peak wavelength was not controlled and kept 25% during all measurements.

An evaluation of the modal content of the rod fibre are performed as a set of C^2 measurements at a range of wavelengths from 1050nm to 1090nm (with a variable step from 1 to 5nm) with the aforesaid chosen spectrum bandwidth of 19.69nm. Based on the measurements, the SM regime of operation is determined from the most offset that was introduced during different measurements and established at a wavelength range, where the power of HOMs is suppressed more than -20dB relative

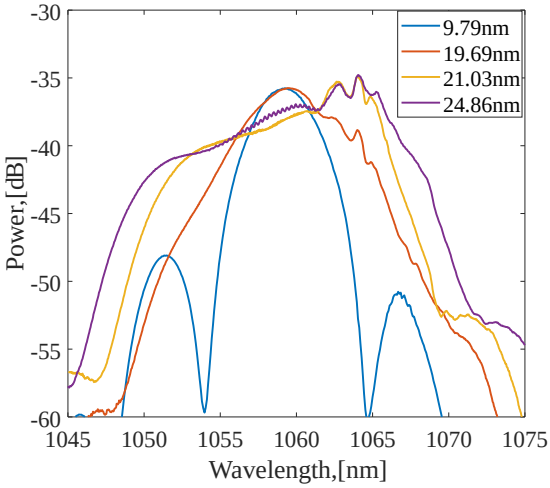

Fig. 3.19 The spectra of the SuperK measured at the central wavelength of 1060nm and combined from 1,3,5 and 7 beams for characterisation of the DMF rod fibre.

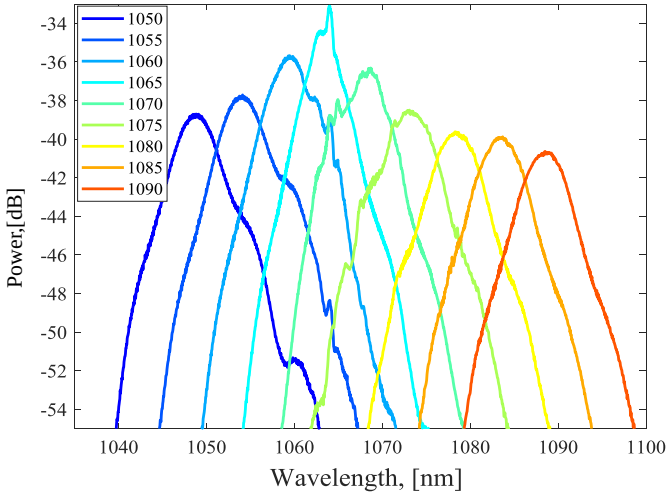

Fig. 3.20 The evolution of the spectrum merged from 3 beams along the wavelength range of the interest.

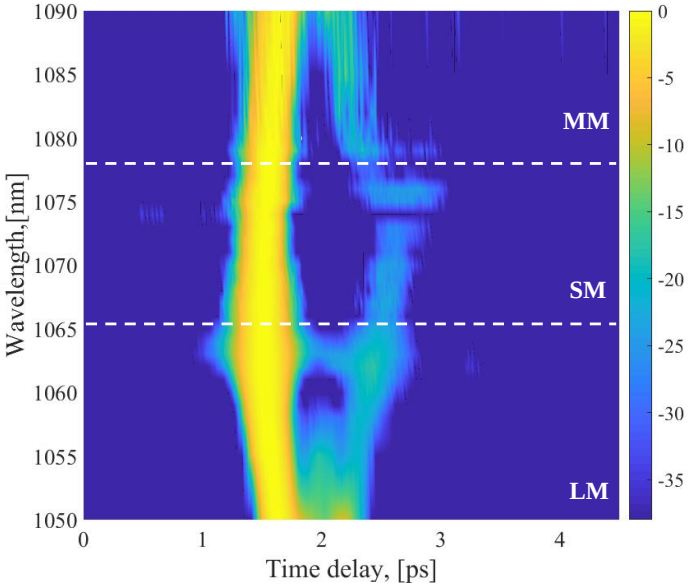

Fig. 3.21 A spectrogram of the intermodal time delay depending on wavelength. Every horizontal line on the spectrogram corresponds to a C^2 measurement with the spectrum centred at a specific wavelength.

to the FM. Figure 3.21 depicts a spectrogram of the intermodal group delay dependence on wavelength, when a certain offset was introduced to excite LP02-like mode in the region of the LM regime. According to the spectrogram depicted in Figure 3.21 the SM regime is present at wavelengths from approximately 1064nm to 1078nm. However, the ranges of the SM regime are dependent on an amount of an introduced offset and can be underestimated due to the influence of the spectral overlap with the MM and LM regimes. As it was expected, close to wavelength of 1064nm the temporal resolution is slightly lower, that leads to broadening of the peaks at the C^2 trace and probably to an additional temporal overlap between modes.

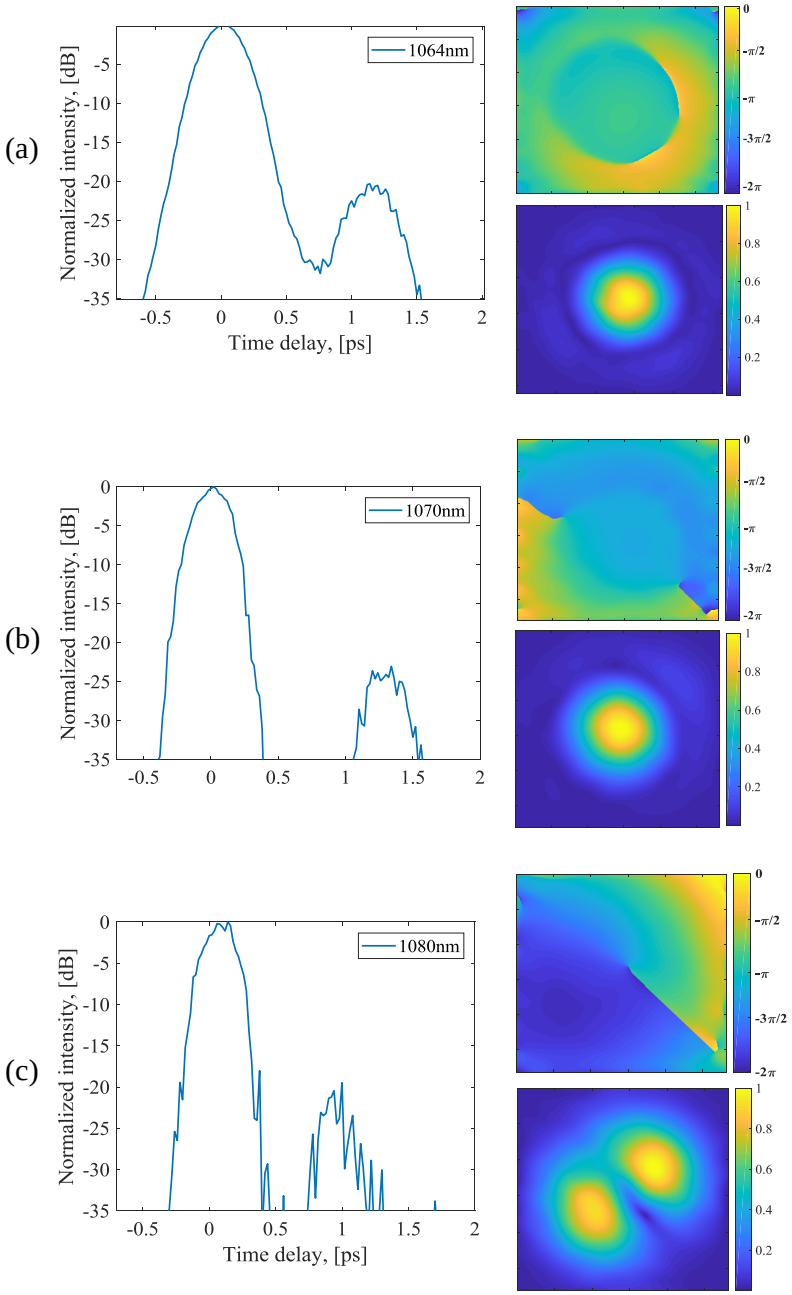

Fig. 3.22 The C2 traces measured at (a) 1064nm, (b) 1070nm and (c) 1080nm and corresponding reconstructed intensity and phase distributions of the propagating HOMs.

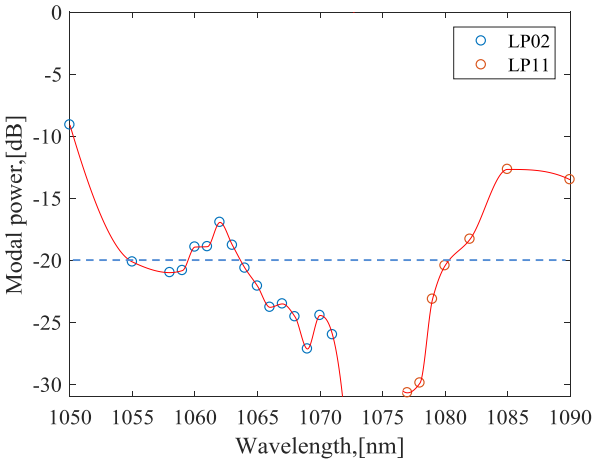

Fig. 3.23 The variation of the modal power for LP_{02} and LP_{11} along a range of the scanned wavelengths from 1050nm to 1090nm.

Examples of the reconstructed C^2 traces at wavelength 1064nm,1070nm and 1080nm are shown in Figure 3.22(a),(b) and (c). The chosen wavelengths correspond to a border between the LM and SM regimes, a middle of the SM regime and a border between the SM and MM regimes. Nevertheless the shape of spectrum experiences influence from the characteristic pump peak at wavelength of 1064nm (turquoise curve in Figure 3.20), the shape of the C2 trace and the reconstruction of modes remain unaffected [Figure 3.22(a)]. Another peculiar feature, that is worth to mention, is LP_{02}-like mode, which is supported by the rod fibre from 1050nm to 1064nm. Its reconstructed phase and intensity distributions are depicted in the inset of Figure 3.22(a). Modal reconstruction within the SM regime is not straightforward, since it resembles the mixture of two modes: LP_{02} and LP_{11}. Approaching the MM regime the reconstruction of HOM becomes more distinct, resembling LP_{11} from the wavelength of 1078nm.

The modal power variation along the scanned wavelength range from 1050nm to 1090nm is shown in Figure 3.23. By the blue and red dots are marked the measured values, while the red curves represent the shape preserving interpolation. Modal power of LP_{11} gradually increases and exceeds -20dB at wavelength longer than 1080nm. For LP_{02} at a range of wavelengths from 1060nm to 1064nm occurs a growth of power, origin of which is hard to determine. It may originate in the additional temporal overlap of the modes due to a change of the spectral shape in a close proximity of the pump wavelength as well as being intrinsic fibre property.

According to the original C^2 method [7], a power of mode is determined by an integral approach averaging over the time delays within the range

$$\frac{1}{\omega_0} \ll t \ll \frac{1}{\Delta\omega} \tag{3.26}$$

Since each measurement was performed with a time delay step close to the upper range of time delays considered by Eq.(3.26) and an influence of the dispersion broadening is minimized, modal powers are detected as the peak values picked up from the C^2 trace.

To verify the results of the C^2 measurement, a model of the DMF rod fibre was made.

Modelling of the DMF rod fibre

The simulation is performed in COMSOL (Appendix A) for a quarter of the fibre cross-section [Figure 3.24] in accordance with a model made by Jørgensen *et al.* in Ref.[48]. The next boundary conditions are applied to get a full set of modes: to the vertical and horizontal axes - a combination of the prefect electric contour and perfect magnetic contour to get a set of the symmetrical modes; or one of these conditions to each axis to obtain a set of the asymmetrical modes; for the outer boundary is used

the scattering boundary condition. The core is built as a quadrilateral surrounded by the inner cladding with introduced air holes of diameter $d_{air-holes}$ separated by the pitch Λ and germanium-doped rings with diameter d_{Ge}. All modes are confined to the inner cladding by the air cladding, represented here as a air ring. One of the advantages of the DMF rod fibre is ability to tune the uncertainties of the core refractive index during the fabrication by varying the diameters of the air holes and the Ge-doped rings. The results of modelling, presented here, are obtained for $d_{air-holes}/\Lambda = 0.095$ and the pitch $\Lambda = 15.58\mu m$. The both values are in disagreement with the fibre specification parameters and were chosen to hit the SM regime measured by C^2 imaging.

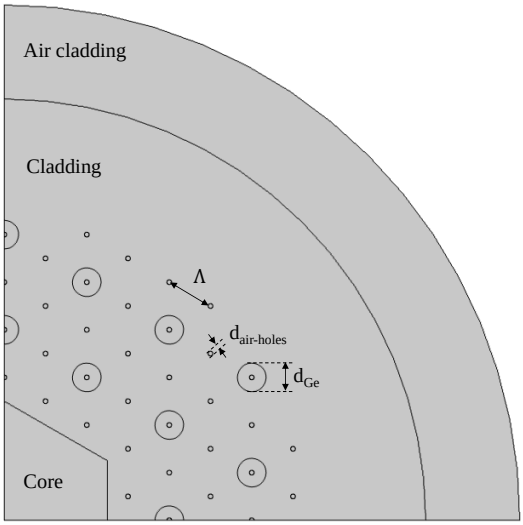

Fig. 3.24 The model of the distributed modal filtering (DMF) rod fibre.

According to the results of the rod fibre measurement the SM regime starts from approximately 1064nm and stretches to approximately 1080nm. The SM regime, obtained during the simulation, corresponds to a wavelength range from 1058nm to 1070nm. Edges of the SM regime are

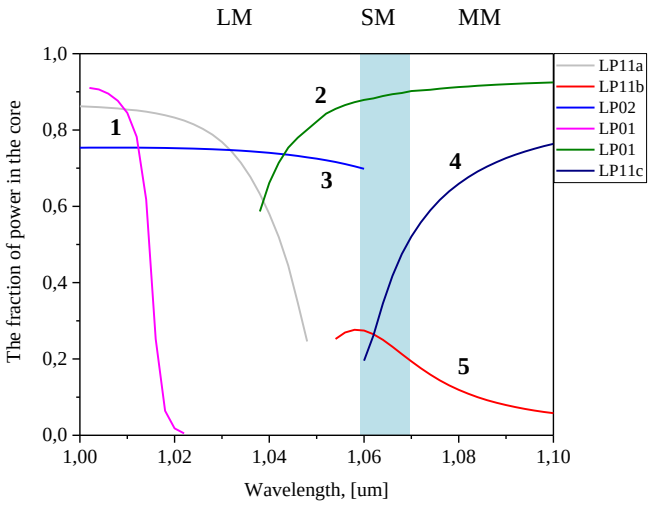

Fig. 3.25 The simulates fraction of the modal powers in the DMF rod fibre for the strongest propagating modes.

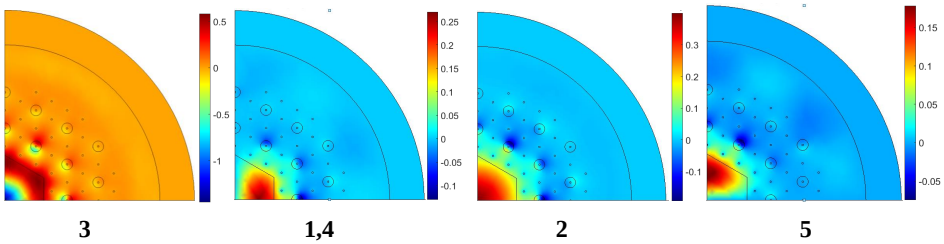

Fig. 3.26 The simulates distributions of the electric field for the strongest propagating modes at 1010nm,1050nm and 1080nm.

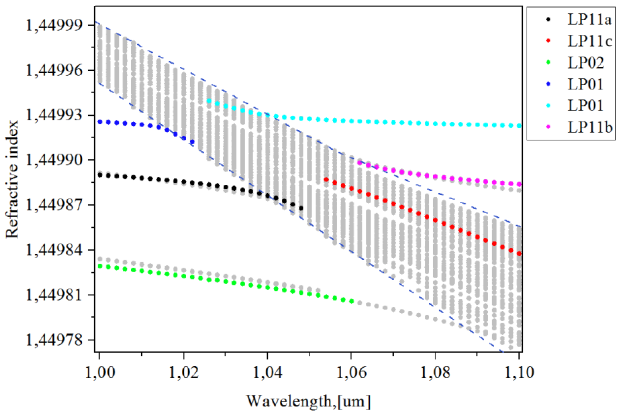

Fig. 3.27 The distribution of the refractive indices of the FM and the first 2 groups of HOMs in the DMF rod fibre.

determined by the fraction of the HOM power in the core lower than 50% and the FM power higher than 80%. Following to the model the main mode that limits the wavelength range of the SM regime from shorter wavelengths is LP_{02}, while from the longer wavelengths it is LP_{11}. The distribution of the fraction of modal power in the core depending on wavelength is depicted in Figure 3.25. It is obvious, that within the MM regime propagate LP_{11b} and LP_{11c}-like modes, while within the LM regime in the rod fibre are supported LP_{11a} and LP_{02}-like modes. Figure 3.26 shows the electrical fields distribution of the modes LP_{11a} at 1010nm (position 1 in Figure 3.25), LP_{02} and LP_{01} at 1050nm (positions 3 and 2 in Figure 3.25), and LP_{11b} and LP_{11c} at 1080nm (positions 5 and 4 in Figure 3.25). Since LP_{11a} at 1010nm and LP_{11b} at 1080nm have the same electrical field distributions and reduction of the fraction of modal power approaching 1050nm, it can be conclude that it is the same mode, which within the SM regime are delocalized and captured by the resonators (Ge doped elements) in the inner cladding.

The distribution of the refractive indices depending on wavelength for the FM and the first 2 groups of HOMs is shown in Figure 3.27. A region of the gray dots corresponds to a continuum of the modes in the Ge-doped elements. When a phase of mode from resonators is matched with a phase of the core mode, they are coupled filtering a mode out of the core. An example of such coupling is LP_{11c} mode [Figure 3.27, red dots], that is captured within continuum of the resonators modes.

Numerically calculated values of the effective refractive indices of the propagating modes are used to determine the DTDs according to Eq. (3.24). Comparison of the numerically and experimentally obtained DTDs is presented in Figure 3.28, where measured values are marked by the dots and numerical values are solid curves. Since LP_{11a} was not noticed during the C^2 measurement, it was not taken into consideration during the calculation of the intemodal time delays. From Figure 3.28 a good agreement for LP_{11} in the MM regime is observed. However, the simulated and experimentally measured DTDs for LP_{02} are in close proximity only for a quadratic fit of the simulated curve.

Since the model is made to fit a measured range of wavelengths for the SM regime, that can be underestimate, a slight disagreement between simulation and experimental results is expected. The width of the wavelength range where the rod fibre is considered single mode, as it was discussed previously, could be affected by the overlap of the input spectrum with the MM or LM regimes during the measurement. Also the introduced strong offset coupling could have influence and reduce the width of the SM regime. Another unavoidable factor is uncertainties in the refractive indices of the core and cladding during a production. As it was mentioned by Jørgensen *et al.* in Ref.[48], a lower refractive index of the core shift the SM regime to longer wavelengths, while a higher values introduce a blueshift of the SM wavelengths. At the same time even a small increase in a pitch of the inner cladding can cause the redshift of the SM regime.

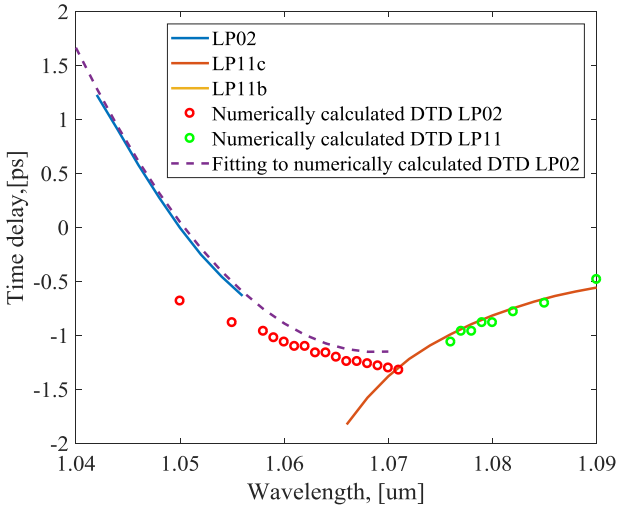

Fig. 3.28 The model of the distributed modal filtering (DMF) rod fibre.

As a conclusion, in this Section was demonstrated an unique ability of the flexible cross-correlated imaging to evaluate a behaviour of modes in a fibre by a spectrogram approach. One of the peculiar features of the set-up is an ultimate tunability in wavelength, bandwidth and spectral shape. Being exceptionally adjustable the system allows to tune an input spectral shape and bandwidth to scan along a wide range of wavelengths. For the DMF rod fibre was chosen a spectral width of 19.69nm, that results in the temporal resolution of 0.56ps. A spectrogram of the intermodal time delays against wavelength resolves all 3 regimes of the rod fibre operation, which is a noteworthy advantage of the flexible C^2 method. However, a special attention should be paid to a spectral shape at wavelengths close to 1064nm, that corresponds to the pump wavelength, since the strong pump peak at 1064nm affects the shape of the spectrum. Also at the shorter wavelengths the input spectrum is smoother than at the longer wavelengths due to reduced noise introduced

by the RF signal from *SuperSelect*. Therefore, if it is possible, better to avoid the C^2 measurements at wavelength of 1064±5nm.

Following the results of measurement, the C^2 trace and the modal detection are slightly affected by the aforementioned features. The reduction of the temporal resolution is detected around 1064nm, that may lead to an increase of modal power of LP_{02} supported within the LM regime. The propagation of LP_{02} itself within a wide range of shorter wavelengths is not common for that type of fibre and could be caused by a strong misalignment of the coupling. Reconstruction of the modes with 2D Fourier filtering demonstrates an opportunity to extract an intensity and a phase distribution of the modes from a single interferogram. However, the current way of reconstruction magnifies the level of the modal intensity distribution and consequently gives a higher MPI values for the mode. Therefore, the modal power was detected from the C^2 traces as a peak values. On the other hand, the chosen step of the time delay at the delay line during the measurements and reduced dispersion broadening allow to consider the effect of averaging over time delays determined in the original method negligible.

3.2.5 Verification of the C^2 stability and reliability

Measurement of a polarization maintaining fibre at wavelengths close to cutoff

For an evaluation of the C^2 set-up sensitivity and repeatability were carried out a number of measurements for detecting modes of small power (approximately 20dB or more of suppression corresponding to the FM) for a fibre, a cutoff wavelength of which is known in advance. As the FUT was chosen a polarisation maintaining (PM) germanium doped step-index fibre (SC-250/14-PM-GE manufactured by *NKT Photonics*). A core diameter of the fibre is 14μm, a cladding diameter is 250μm, an

average mode field diameter (MFD) is approximately 14.7μm. At the beginning the effective cutoff wavelength was measured by a modified version of a bend reference technique [31, 28] and afterwards by the C^2 method.

Procedure of the original bend reference method is based on a comparison of fibre transmissions. First, a white light source is coupled to a straight fibre and its transmission is measured. Afterwards, the FUT is bent with a curvature radius of 124cm and the output power is measured again. With every measurement the curvature radius of bend decreases without any changes in the input coupling condition. As a result, a difference in transmissions between the straight and bent fibre is derived and an effective cutoff wavelength is determined as a long wavelength, at which the attenuation edge is greater than the long wavelength baseline by 0.1 dB [Figure 3.29- 3.30]. One of the criteria of the single-mode operation is suppression of the first HOM (LP_{11}) to more than 19.3 dB for a 28-cm coil. The procedure for the modified version of measurement is similar, only the curvature radiuses differ. For example, a condition, that corresponds to the 28-cm coil bend for the modified measurement is preserved under the bend marked as "31cm Table30" in Figure 3.29 and depicted by a blue curve. Its transmission power alone is presented in Figure 3.30. According to the bend reference cutoff measurement, when light is coupled to the fast polarization axis of the FUT, LP_{11} experiences cutoff within the wavelength range from 1035nm to 1045nm.

To verify the cutoff wavelength, the FUT is scanned by the C^2 method along wavelengths from 1000nm to 1045nm with a step of 5nm and an input spectrum bandwidth of approximately 7.23μm (1 beam with 30% of power). A configuration of the set-up is similar to Figure 3.10, where as a FUT is used 1m of SC-250-14-PM-Ge fiber. To couple light into the fast axis of the fibre an additional polariser, is inserted before the FUT. An input coupling is offset to insure the propagation of LP_{11} mode along a scanning wavelength range. The resultant spectrogram of the C^2 scan,

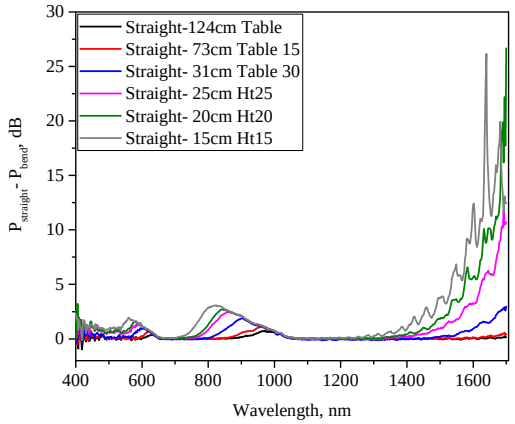

Fig. 3.29 Modal properties test of SC-250-14-PM-Ge fibre.

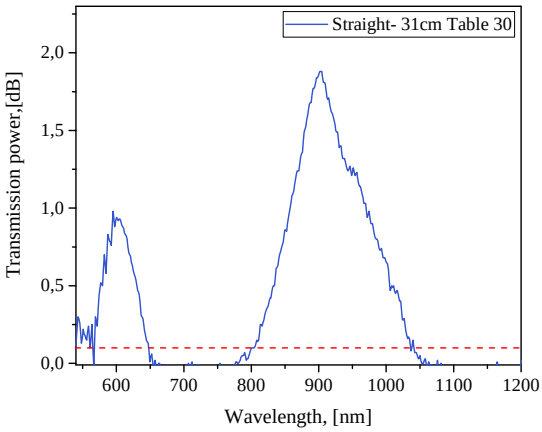

Fig. 3.30 The transmission power measured for a condition that corresponds to a 28cm coil. A cutoff is determined as an intersection of the long wavelength edge and the reference level of 0.1dB, marker as a dashed red line.

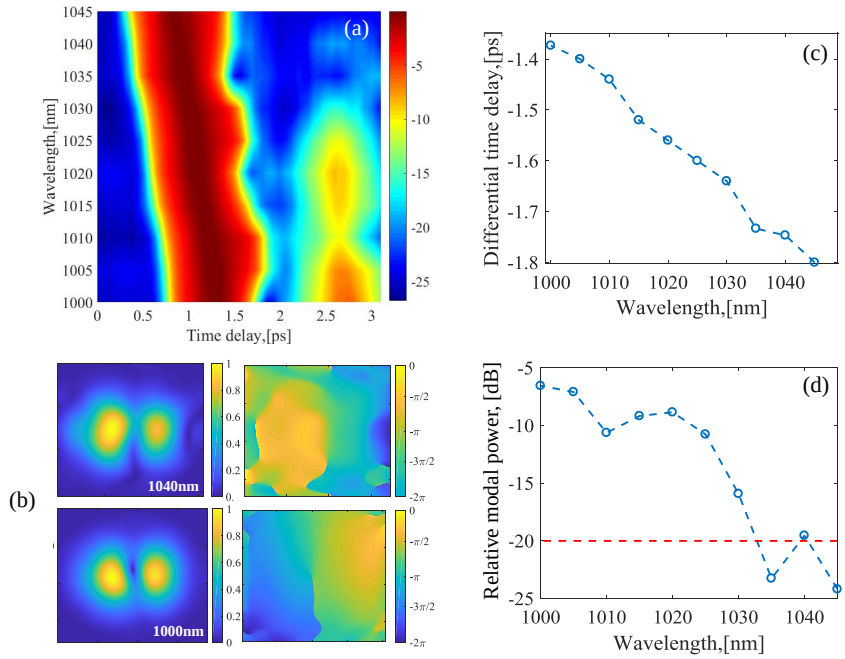

Fig. 3.31 (a) A spectrogram of intemodal time delay depending on wavelength for the FUT. (b) The reconstructed intensity and phase distributions of the LP_{11} at 1000nm and 1040nm. (c) Dependence of the DTD between LP_{01} and LP_{11} on wavelength. (d) The variation of the modal power of LP_{11} along wavelengths.

presented in Figure 3.31(a), demonstrates the presence of LP_{11} at shorter wavelengths and its cutoff approaching 1030nm. Figure 3.31(b) shows the reconstructed intensity and phase distributions of LP_{11} at wavelengths of 1000nm and 1040nm. Moving from shorter to longer wavelengths the DTD between modes increases as it is shown in Figure 3.31(c). A change of the relative power of LP_{11} with wavelength is demonstrated in Figure 3.31(d).

From Figure 3.31 it can be seen, that results obtained by the C^2 methods confirm the cutoff of LP_{11} within wavelengths from 1035nm to 1045nm. However, a precise position of the cutoff wavelength is difficult

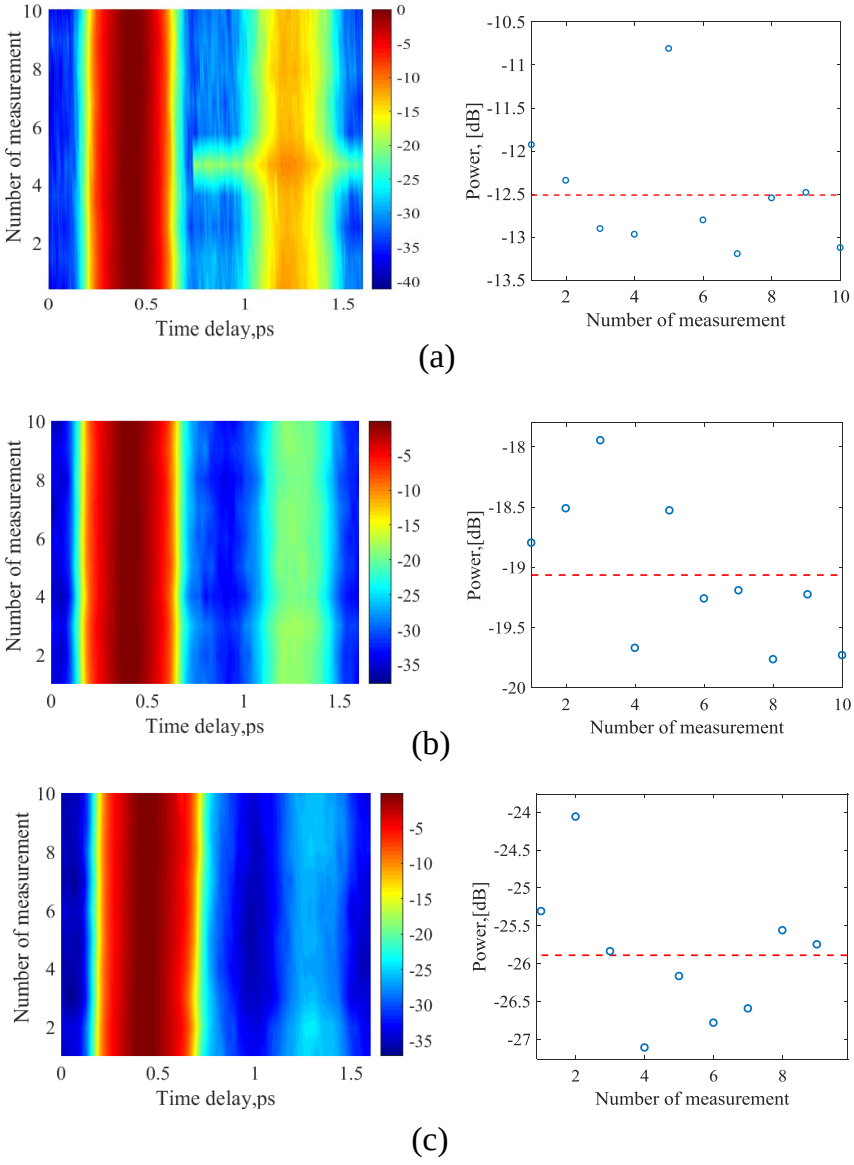

Fig. 3.32 (a) A spectrogram of LP_{11} for the 10 measurements at 1029nm and (b) at 1040nm with a slight offset , (c) at 1040nm with an improved coupling. Graphs from a side depicts a spread of modal power. By the red dashed line is marked the average modal power.

to determine, since the modal power of LP_{11} diminishes not gradually. To investigate the accuracy and repeatability of modal detection by the C^2 method is performed a set of measurements at wavelengths of 1040nm and 1029nm. Figure 3.32 (a) demonstrates a spectrogram for 10 repeated measurements at wavelength of 1029nm with the same input coupling condition as for the wavelength spectrogram, when LP_{11} was deliberately excited in the FUT. A corresponding deviation of the modal power in depicted in a figure from a side of the spectrogram. A range of power deviation, determined as a difference between the maximum and minimum detected values, is 2.39dB. An average modal power is -12.53dB and the corresponding standard deviation is 0.712dB. From the spectrogram it can be observed that a measurement number 5 differs from other within a set and has a non-characteristic jump in power around 0.6ps at the C^2 trace. Generally, an interferometric set-up is sensitive to a change of the ambient surroundings and most probably this measurement was corrupted during the experiment. Excluding that measurement from the set, the average power becomes -12.7dB and the standard deviation is 0.464dB. Figure 3.32 (b) demonstrates a spectrogram obtained under the same coupling condition at wavelength of 1040nm. A measured spread of powers is 2.6dB with a mean value of -19.06dB and the standard deviation is 0.606dB. For the improved coupling condition [Figure 3.32 (c)] an average power of LP_{11} in the fibre decreased to -25.9dB, however, the range of deviation increased to 3dB and the standard deviation is 0.865dB.

A deviation of the detected modal powers establishes an evidence of the larger detection error for the modes of smaller power. If one excludes the 5th strongly deviating measurement from the spectrogram in Figure 3.32 (a), a tendency becomes more clear, definitely showing a better reliability in detection of stronger modes. In the context of the cutoff measurement the range of the cutoff wavelengths decreased to approximately 5nm from 1040nm to 1045nm. For the more precis

evaluation of the cutoff wavelength a larger amount of measurements could be suggested, that is a quite time consuming. Therefore, the flexible C^2 imaging method is a valuable tool that allows to get a detailed insight into a general behaviour of the modes approaching the cutoff, but one could find more suitable techniques for the cutoff wavelength measurement.

Also, it should be mentioned, that the sensitivity and accuracy of the set-up are lower than expected and can be improved by exclusion of the main noise sources. First of all, the set-up can be additionally stabilized during the measurement reducing an influence from surroundings. An another option could be optimization of the equipment. In the case of the current measurement the main error is brought by the low quantum efficiency of the 12bit camera [76], which is less than 10% of the total efficiency at the chosen wavelength range. Also during alignment an appropriate attention was not paid to the spatial frequency of the fringes, which was a bit lower than, for example, for the rod fibre measurements. Introducing the larger angle between interfering beams and increasing the spatial frequency one can get improvement in the modal reconstruction.

To verify the accuracy of the C^2 set-up to determine an intermodal time delay was performed a comparison of the method with another imaging technique under the same measurement conditions, which is described in details in the next section.

Comparison of the C^2 and S^2 imaging techniques

As it was mentioned in Section 2.7, among developed modal characterisation techniques a spatially and spectrally resolved imaging (S^2) and cross-correlated imaging (C^2) might be considered as the most applicable techniques for the fibre modal content evaluation. Until this section all previously discussed results were focused on implementation of the C^2 technique and its advantages and disadvantages in estimation

of the fibre modes characteristics. However, in the current section an attention is manly paid to a comparison of the C^2 technique with another valuable technique for the modal decomposition, namely the S^2 imaging technique.

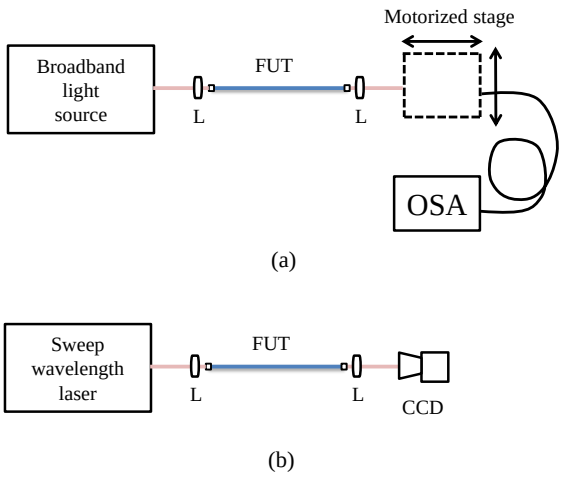

Fig. 3.33 The scheme of (a) the original and (b) modified S^2 set-up.

There are two approaches for the S^2 imaging: original and modified. The scheme of the original S^2 set-up is depicted in Figure 3.33(a). Light from a broadband source is coupled to the FUT, magnified output of which is scanned over *xy*-plane by a pigtail fibre fixed at a motorized stage. Afterwards, transmission spectra at all *(x,y)* points are collected by the OSA. In the case of the modified S^2 set-up [Figure 3.33(b)] a scanning is performed along wavelengths by a sweep wavelength source and a near-field picture of the fibre output is recorded at each scanning wavelength by a camera. From a stack of images are derived transmission spectra at all *(x,y)* points, whose are analysed in the same way as for the original approach.

The S^2 method is based on a principle of the spatial and spectral interference between modes propagating in a fibre. When two modes interact

a characteristic interference pattern is observed in the near-field image, as well as in a transmission spectrum, measured at the spatial point of their interaction, due to the modal group delay difference. Measuring the transmission spectra in each *(x,y)* point of the imaging plane and applying the Fourier transform one can derive a S^2 trace, which in analogy to a C^2 trace, contains an information about a fibre modal content as modal powers and differential time delays of the propagating modes. According to the assumption made in Ref.[65] one of the propagating modes has to be dominant, generally it is the FM, while the power in other modes is small. Taking into consideration aforesaid assumption the intensity of one mode can be represented through an intensity of the dominant mode by wavelength independent constant $\alpha(x,y)$ that is [65]

$$\alpha(x,y) = \frac{1-\sqrt{1-4f^2(x,y)})}{2f(x,y)}, \tag{3.27}$$

where f is the ratio between an amplitude of the HOM at the characteristic time delay $\tau = \tau_m$ and the amplitude of the FM at $\tau = 0$ in the Fourier transform. From $\alpha(x,y)$ and $I_t(x,y)$ (an integrated intensity over all frequencies of the optical spectrum at a given *(x,y)* point) the intensities of the FM and corresponding HOM are found as [65]

$$\begin{aligned} I_1(x,y) &= I_t(x,y)\frac{1}{1+\alpha^2(x,y)} \\ I_2(x,y) &= I_t(x,y)\frac{\alpha^2(x,y)}{1+\alpha^2(x,y)} \end{aligned} \tag{3.28}$$

A proper comparison of the S^2 and C^2 can be achieved, if measurements are performed under the same input conditions and suitable for both techniques operational arrangement. Aforesaid requirements can be fulfilled, when both set-ups share the same input light source. Therefore, based on available equipment and mentioned earlier measurement requirements, it was decided to compare the C^2 method with the original

S^2 method and to combine two set-ups into the one in purpose to prevent any influence of an input alteration on measured results.

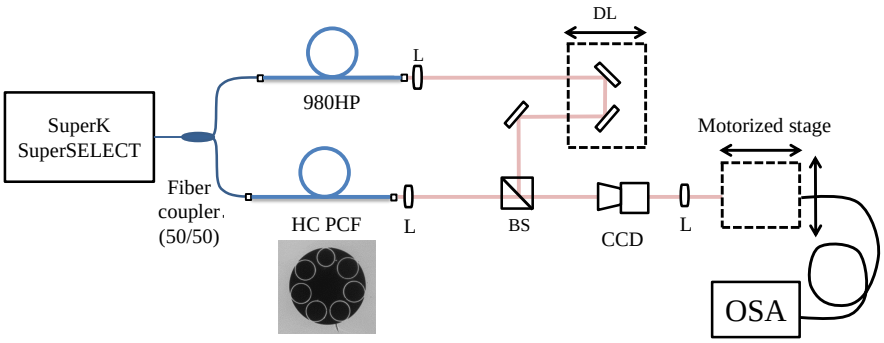

Fig. 3.34 The scheme of the combined set-up for the C^2 and S^2 imaging.

Figure 3.34 shows a scheme of the combined set-up used to perform the C^2 and S^2 measurements under the same coupling condition. As a fibre under test is chosen a hollow core fibre, designed for the delivery of ultrashort laser pulses of high powers, properties of which is described in details by *Michieletto* in Ref.[59, 60]. The inset, inserted below the FUT, demonstrates the profile of the hollow core PCF with 7 antiresonant elements attached at the core-cladding interface. In the case, when the C^2 set-up has to be transformed to the S^2 set-up the reference arm is blocked and the beam splitter together with the camera are removed from the set-up. The FUT output then is magnified at the pigtail fibre, fixed at the motorized stage, that performs a two-spatial dimensional scanning. The temporal resolution of the C^2 trace depends on the dispersion broadening in a fibre and reciprocally on the input spectrum bandwidth of the seed source. Therefore, to reach a high temporal resolution for the C^2 method, the FUT has to be balanced by a single mode fibre with the same dispersive properties and the input light source spectrum has to be broad.

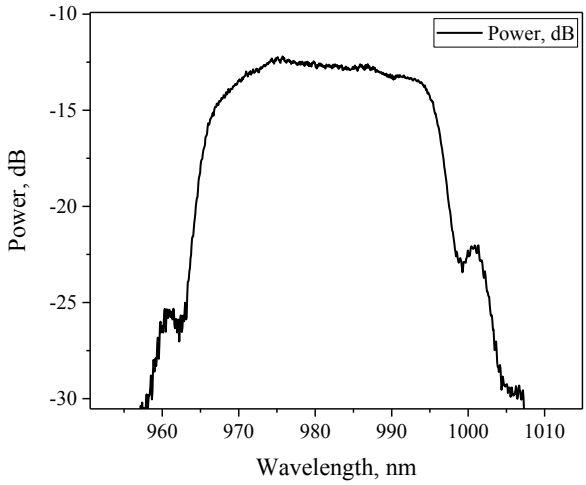

Fig. 3.35 The spectra used in the measurement at the central wavelengths of 980nm.

Simultaneously, a high temporal resolution for the S^2 imaging is reached by a deliberate choice of a spectral bandwidth and a finite resolution of an OSA. Therefore, to satisfy both methods, the input spectrum is chosen to be as wide as possible and still been able to preserve a smooth shape of a C^2 trace.

The input spectrum of *SuperK* filtered by *SuperSELECT* is merged from 8 beams positioned at wavelengths of *968nm-972nm-976nm-980nm-984nm-988nm-992nm-996nm* with separation of 4nm and controlled power of 25% for each beam. A choice of the central wavelength of the spectrum is made based on a properties of the FUT, which experience the lowest loss at the aforesaid wavelength. Considered input spectrum is shown in Figure 3.35. Its bandwidth is approximately 33.71nm, that in combination with the OSA resolution of 0.04nm allows to evaluate

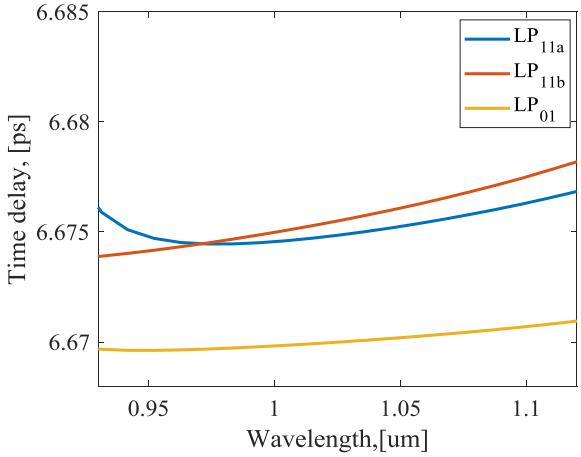

Fig. 3.36 A numerically calculated a time delay dependence on wavelength for LP_{01}, LP_{11a} and LP_{11b} modes in the FUT.

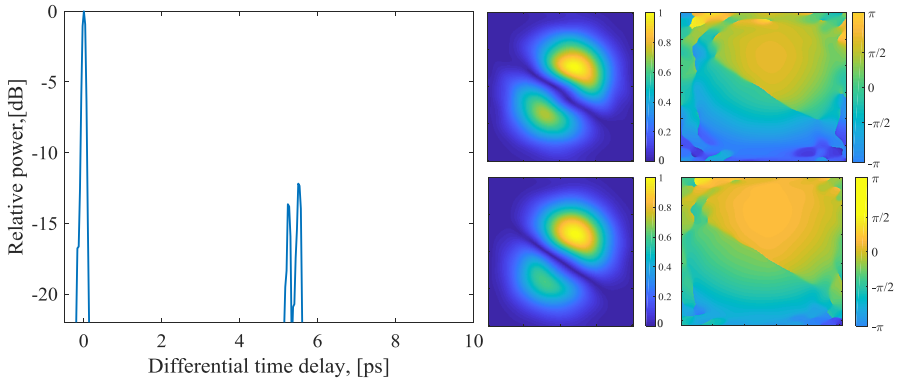

Fig. 3.37 The C^2 trace for the measured FUT with an input spectrum centred at the wavelengths of 980nm.

a range of time delays of approximately 20ps for the S^2 set-up. The length of the FUT is 2m and for the C^2 measurement it is balanced by the identical fibre of the similar length coiled with a diameter of 9cm, which results in elimination of all present HOMs and improvement of

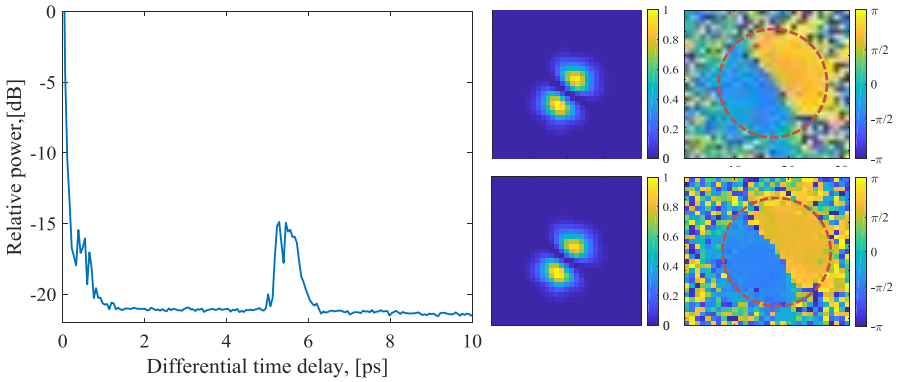

Fig. 3.38 The S^2 trace for the measured FUT with an input spectrum centred at the wavelengths of 980nm.

the temporal resolution that is 0.11ps for the FM, the highest achieved for the current set-up. According to a numerically calculated dependence of the modal time delay on wavelength [Figure 3.36] at wavelength of 980nm are expected the FM and two LP_{11} modes delayed corresponding to the FM by 4.73ps and 4.94ps.

Initially, the measurement is performed by the C^2 method, since it takes a few minutes and afterward by the original S^2 that takes a couple of hours. The resultant C^2 trace is depicted in Figure 3.37. It discovers two HOMs at the time delays of approximately 5.26ps and 5.53ps with relative powers of -13.5dB and -12dB corresponding. The reconstructed intensity and phase distributions definitely demonstrate two LP_{11} modes of the same geometrical direction. Subsequently, the S^2 measurement is conducted and the derived S^2 trace is shown in Figure 3.38. It possesses the same measurement results, revealing two HOMs delayed by 5.22ps and 5.47ps corresponding to the FM. The extracted profiles of the modes exhibit two LP_{11} of the similar intensity and phase distributions and relative powers of -14.4dB and -11.4dB. Nevertheless, the measurement

condition for the S^2 method is optimal, but not outstanding, the demonstrated results for both techniques exhibit a good agreement in the modal content detection, time delays and relative powers.

Being independent imaging techniques, the C^2 either the S^2 has to be chosen depending on the experimental requirements, since each of them has its own advantages and disadvantages. To sum up, it could be mentioned, that both of techniques are valuable and strong diagnostic tools. However, despite being very sensitive in determination of the modal power, the temporal resolution of the S^2 technique is limited by the resolution of OSA and are constrained by a requirement of the dominant modes present in a fibre. To overcome the first limitation and to be able to resolve small intermodal delays, a long section of fibre has to be analysed. However, it is not always possible to achieve a large difference in modal power for propagating modes, which makes determination of MPI values unreliable. On the other hand, the C^2 is free of such constrains and can easily detects modes of equal power, if a high temporal resolution of the system is reached. In this case, a complication can arise from a lack of the suitable reference fibre. If the residual dispersion of fibers in the both arms of the interferometer is not balanced, increase of the spectal width would lead to a poor temporal resolution. However, if a suitable fibre and a broad input spectrum are used, the C^2 could resolve small intermodal delays in a short piece of a fibre. Characterisation of the long fibre lengths, on the other hand, is not straightforward owing to a complicated set-up alignment, since a difference in optical paths of the both interferometric arms has to be in order of a micrometer for low coherent light sources. The aforementioned features, as well as tedious and sometimes even complicated alignment and sensitivity to the ambient medium of the interferometric set-up, are disadvantages of the method.

Chapter 4

19-cell hollow core photonic bandgap fiber

Conventional fibres guide light by total internal reflection, providing transmission within a core of a higher refractive index. However, fibres of advanced designs, like for example, photonic bandgap fibres (PBGFs), can transmit light by a totally different mechanism, not inherent to conventional fibres. HC PBGFs are designed as a regular periodic structure of air holes in a cladding, maintained along the whole length of a fibre, meanwhile a waveguiding air core is created as a defect in a structure by removing a certain amount of central capillaries from a stacked preform. A variety of the distinctive features intrinsic to HC PBGFs has led to many advantageous applications in telecommunication, high pulse power delivery and gas sensing [77]. Since light is predominantly guided in the air core, HC PBGFs are expected to exhibit a low attenuation and non-linearities compared to solid-core fibres. Nevertheless, the lowest reported loss for HC PBGF is 1.2dB/km [84]. The loss mechanism of HC PBGF originates in scattering on roughness of the glass surface and, compared to the loss limit of the silica core fibre ($\sim$ 0.15dB/km [50]), there is a long way for improvement. One of the approaches for the

loss reduction and enhancement of the confinement ability of the air-guiding modes is introduction of antiresonant features around the core that can efficiently reduce the field intensity at the glass-air interfaces [85, 86, 97].

Current Chapter is focused on a simulation of the 19-cell HC PBGF with an introduced anti-resonant elements (ARE) that allowed to reduce a fraction of power of the air-guiding modes resided within the air-glass interface and, thus, to decrease a transmission loss of the fibre.

4.1 The design and physical properties of the 19-cell HC PBGF

The 19-cell HC PBGF has been manufactured by *NKT Photonics*. Its cross-section is shown in Figure 4.1 (a). The cladding is composed as a hexagonal periodic array of the air-filled capillaries and the core is formed by omitting 19 central capillaries from the preform. At the core-cladding interface are inserted solid silica rods, creating the anti-resonant elements (AREs). They are clearly seen in Figure 4.1 (b) as 12 ellipses symmetrically positioned around the core. The core and cladding diameters are 22μm and $129\pm2\mu$m corresponding. The air-filling fraction is 91% and a cladding pitch is 3.7μm. The main physical parameters of the fibre are presented in Table 4.1.

The fibre is designed to be a low loss within an operation bandwidth of the C-band from 1530nm to 1565nm. In Figure 4.2 (black curve) is depicted a FM loss measurement performed by a cut-back method. The level of the measured loss at 1550nm is approximately 4dB/km, while the lowest level of loss is detected at wavelength of 1536nm and equal approximately 3dB/km [Figure 4.2]. The 3dB bandwidth of the low loss transmission window extends from 1515nm to 1565nm and is 50nm wide.

Table 4.1 The physical properties of 19-cell HC PBGF.

Dimensions	
Core diameter	22μm
Cladding diameter	$129\pm 2\mu$m
Cladding pitch	3.7μm
Air-filling fraction	91%
Optical properties	
Mode field diameter	14μm
Fundamental mode loss at 1550nm	4dB/km

Properties of the 19-cell HC PBGF and the low-loss performance within the C-band of wavelengths have appealed for further investigation of the fibre implementation as a transmission medium in MDM scenario. Since fibre modes in MDM are considered being individual channels for data transmission, an insight into the modal behaviour and losses over the low loss bandwidth of the fibre are in great concern. Consequently, a reliable model of the fibre is of high importance. In the next section will be presented a detailed description of the modelling procedure and a main set of parameters chosen for the 19-cell HC PBGF simulation.

4.2 The fibre modelling and the simulation parameters

It should be emphasized, that the model described in this section, is an idealised representation of the 19-cell HC PBGF with AREs. Figure 4.1(a) presents a scanning electron microscope (SEM) image of the FUT cross-section. Figure 4.1(b) shows a zoomed region at the core-cladding boundary. Here AREs are clearly seen as a number of ellipses distributed around the core. This form of core surrounds imitate an arrangement of Anti-Resonant Reflective Optical Waveguides (ARROW) [57] and, when an appropriate preform is used, the shape of AREs is consistent with

the surface tension forces present during the fibre-drawing process [86]. The AREs, when they are tuned to the anti-resonance with the cladding bandgap, suppress the fibre's loss due to an anti-resonant reflection at the high-low index interfaces [57]. Each of the individual layers at the core boundary and in the cladding can be considered as a Fabry-Perot-(FB-) like resonator. In the case of the resonance in FB-like resonators at the certain propagating wavelengths, light escapes from the core and transmission is low. While, in the case of the anti-resonance, due to the destructive interference in the FP-like resonators, light is trapped within the low-index core. In the same manner, by adjusting the shape of walls at the core-cladding boundary a low loss transmission can be achieved over a certain operational wavelength range.

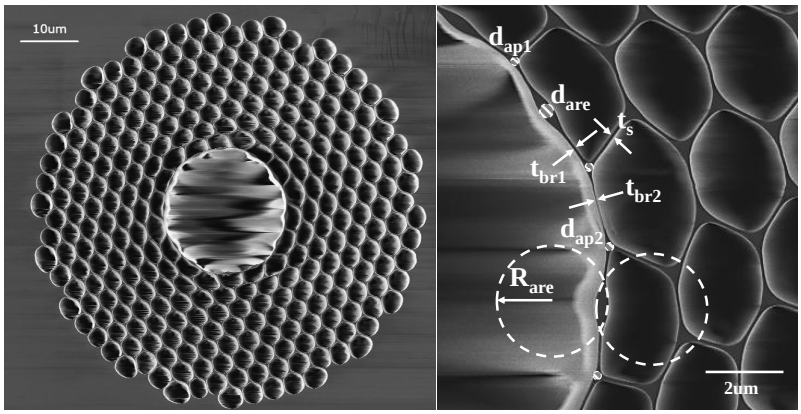

(a) (b)

Fig. 4.1 (a) The scanning electron microscope (SEM) image of the 19-cell HC PBGF cross-section. (b) A zoomed region of the fibre cross section with the anti-resonant elements and the main parameters, marked by circles and arrows, used for the simulation.

The low loss transmission window mainly depends on the edges of bandgap and the surface modes (SMs) that are present within the bandgap.

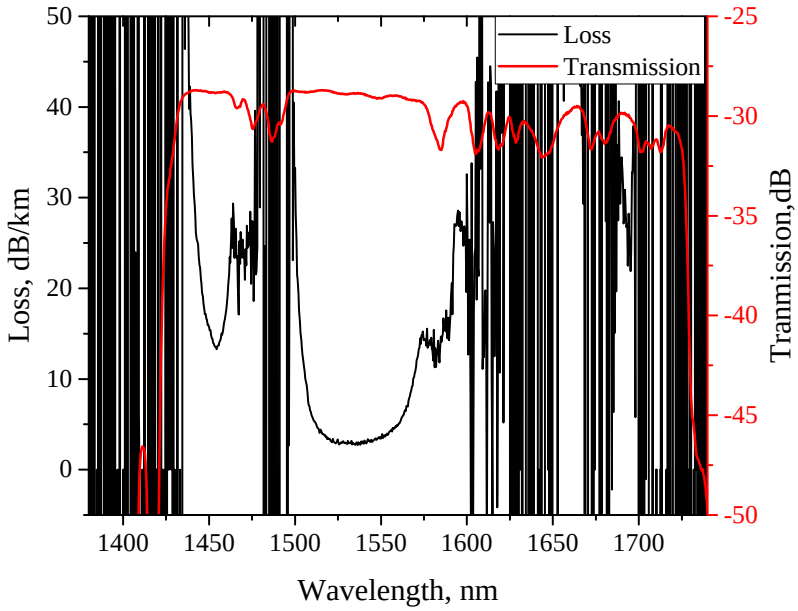

Fig. 4.2 Black curve: Measured by the cut-back method loss of the 19-cell HC PBGF. Blue curve: The transmission spectrum through 1m of 19-cell HC PBGF.

One of the disadvantages of the current geometry is an introduction of unwanted anti-crossing events between the guided modes and the SMs. At wavelengths where the air mode and SM are phase matched, they are not "pure" any more, since both of the modes concentrate their energy in the air core and silica region around the core. The modes confined by the silica glass at the core-cladding interface can easily couple to the lossy cladding modes. Therefore, the air-guiding modes experience strong attenuation approaching the wavelength of the anti-crossing point [6, 107].

Following Ref.[62], the width of the bandgap is determined by the air-filling factor f, that depends on the width of an unit cell in the cladding D, the diameter of the curvature D_c [Figure 4.3(b)] and the pitch Λ as:

$$f = \left(\frac{D}{\Lambda}\right)^2 \left[1 - \left(1 - \frac{\pi}{2\sqrt{3}}\right)\left(\frac{D_c}{D}\right)^2\right] \tag{4.1}$$

The bandgap width can be determined based on a transmission curve, presented in Figure 4.2 (red curve). According to the transmission measurement, the bandgap extends from approximately 1426nm to 1728nm. A number of deeps, present at the transmission spectrum, corresponds to an interaction of the air-guided modes with the SMs. The widest region of the high transmission stretches from 1500nm to 1572nm and compatible with the measured low loss region at approximately the same wavelength range, depicted in Figure 4.2 by black curve. Therefore, it might be concluded that the low loss bandwidth of the fibre is positioned in the center of the bandgap and constricted by the SMs at the shorter and longer wavelengths.

To obtain a model with a realistic core-cladding boundary representation, the average geometric parameters of the bridges, nodes and apexes were measured from the SEM image presented in Figure 4.1(b). One of the main goals was to fit a position of the low loss bandwidth determined by the transmission measurement. The air-filling factor f and the pitch Λ are known from the fibre's specification and are fixed. However, the curvature of the unit cells D_c is unknown and can be varied in the model for better match of the low loss bandwidth. To maintain the air-filling factor f unchanged during the modelling, while D_c is changed, the relative hole size D/Λ is also adjusted based on Eq. (4.1).

By trail-and-error it was determined that a combination of D/Λ equals 0.965 and D_c equals 1.767μm gives the best fit for the low loss transmission window. However, the bandgap edges and position of the SMs are in a slight disagreement with the measurement. It worth mentioning, that presence of the SMs are dictated by the geometry profile of glass structure at the core-cladding boundary. Since the SMs reside in very small silica regions, like bridges, nodes and apexes at the glass

interface of the first ring of holes around the core, even a small mismatch between the real and simulated parameters of the geometry can lead to a discrepancy.

The main parameters, used in the model, are marked by arrows and dashed curves in Figure 4.1(b). Their averaged measures listed in Table 4.2. The amount of glass at the core-cladding boundary was determined by the thickness of the struts t_s and the bridges in the cells with AREs t_{br1} and without them t_{br2}, and by a size of the apexes d_{ap1} and d_{ap2}. The shape and size of the elliptical features were measured by written inside them circles of the diameter d_{are}, while two circles of larger curvatures R_{are} set up the realistic shape of the AREs at the core-cladding boundary. It should be said, that SEM images were taken under condition without low vacuum, that results in accumulation of the additional charge at the surface and presence of regions with higher brightness around silica glass. Therefore, determination of the silica edges based on the SEM image is not straightforward and imposes a discrepancy within $\pm$2pixel that correspond to 0.06μm at the regions of the high contrast.

In Figure 4.1(a) and (b) can be observed a certain degree of distortion of the unite cells around the core, that is formed due to an extension of the core from a designed diameter of 5Λ (18.5um) to 22μm during the fibre draw. The aforesaid effect establishes a deformation of a few first rings of the air holes in the cladding. To derive the final geometry of the 19-cell HC PBGF, the simulation was performed in two steps. At the first step, in COMSOL Multiphysics (Appendix A) is created a geometry based on already known parameters without consideration of distortion. Then all coordinates of the geometry are exported and processed in Matlab, where the Gaussian expansion is implemented to a set of coordinates to reach realistic expansion of the core and deformation of the cladding. Afterwards, resultant expanded geometry is adjusted according to the averaged measures obtained from the SEM image, listed in Table 4.2 and an additional set of simulations is executed in COMSOL.

Table 4.2 The parameters used in the model and corresponding averaged measures from the SEM image.

Parameters	**Measured**	**From the model**
Thickness of the struts t_s	0.12um	0.126um
A thickness of bridges in the cells with AREs t_{br1}	0.11um	0.07um
A thickness of bridges in the cells without AREs t_{br2}	0.08um	0.12um
A diameter of a circle written in an apex between two cells with AREs d_{ap1}	0.64um	0.68um
A diameter of a circle written in an apex between the cells with AREs and without ARES d_{ap2}	0.2um	0.16um
A diameter of a circle written into AREs d_{are}	0.4um	0.35um
Curvature of the AREs R_{are}	1.7um	2um

To minimize a calculation time and taking into consideration a sixfold symmetry of the 19-cell HC PBGF, simulation is performed in a quarter domain with four boundary conditions (Appendix A) to derive a full set of modes supported by the fibre. Figure 4.3(a) shows the initial geometry of the fibre cross-section, Figure 4.3(c) the fibre cross-section after expansion of the core. Comparably to the real fibre, an extension of the core has impact on the first 3 rings, while the last ring of air holes is almost unaffected. The shape of air holes in the cladding is chosen according to Ref. [62] as a hexagon with a distance between walls D and corners rounded with a curvature D_c [Figure 4.3(b)]. Figure 4.3(d) shows the Gaussian distribution curve, from where a relation between new and old coordinates of the model is found. The value of the refractive indices are considered to be 1.45 for the silica and 1 for the air.

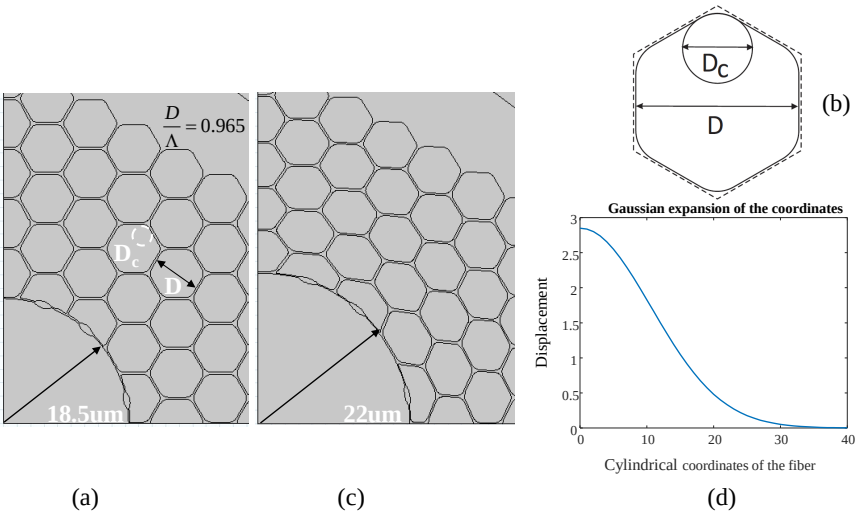

Fig. 4.3 A schematic representation of the modelled fibre cross-section. (a) An initial geometry. (b) An unit cell of the cladding structure. A dashed line represents the idealistic shape of a hexagon. A solid line is a hexagon shape with rounded corners used in the model. (c) A geometry of the fibre cross-section with expanded core. (d) Gaussian curve, that describes a relation between old and new coordinates of the geometry.

4.3 Results of the modelling

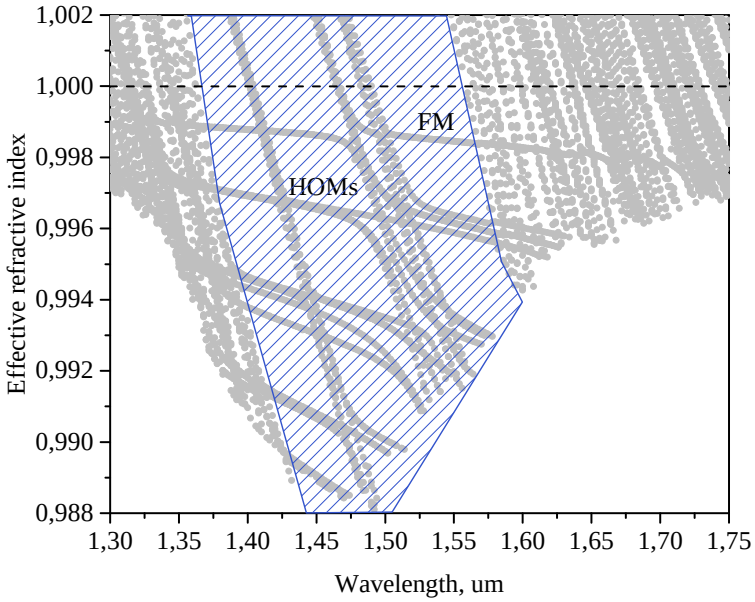

Fig. 4.4 Distribution of the effective refractive indices of the modes, propagating in the fibre, along wavelengths. By sparse blue polygonal is marked the edges of the bandgap. The black dashed line marks the air line.

As a result of the modelling, it was revealed that within the air core is confined two degenerate FMs ($HE11^{x,y}$) and 3 groups of the HOMs ($HE21^{o,e}$, TE_{01}, TM_{01}, $HE31^{o,e}$,$EH11^{o,e}$, $HE12^{x,y}$). The suffixes "x" and "y" denote two orthogonal polarizations, while "e" and "o" are used to identify the even and odd degenerate modes. Figure 4.4 shows dependence of the numerical effective indices on wavelength. The continuum of the cladding modes extends from 1300nm to 1370nm at shorter wavelengths and from 1570nm to 1750nm at longer wavelengths. The edges and the region of the bandgap is marked by the polygon with sparse lines. The transmission window for the FM starts from 1370nm and extends to 1570nm. However,within the bandgap region the fibre

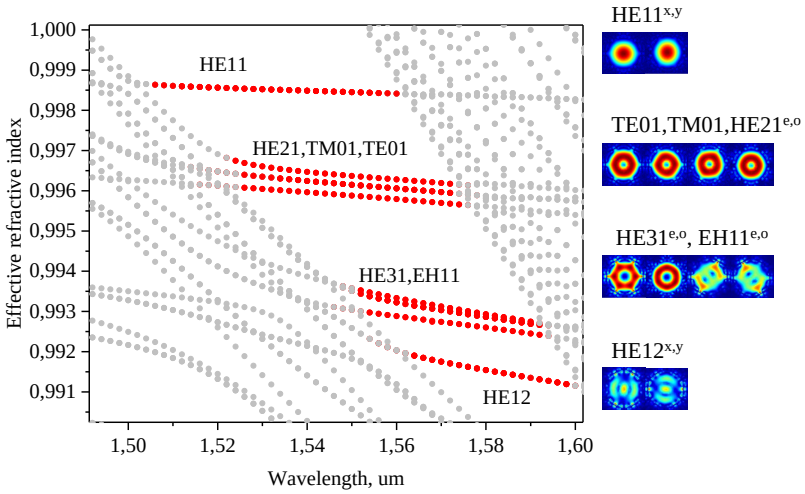

Fig. 4.5 The distribution of the effective refractive indices along wavelengths for the air guided vectorial modes and corresponding profiles of their intensity distribution.

has a crossing between the FM and the SMs around 1410nm and two avoided crossings around 1478nm and 1496nm. Presence of the SMs results in a reduction of the transmission bandwidth from 200nm to 50nm within the range of wavelength from 1510 to 1560nm. Comparing numerical results of simulation with the measured transmission, the high agreement in a width and position of the low loss transmission region is evident. However, a width of the measured bandgap is wider (from 1420nm to 1730nm) and its position is shifted to longer wavelengths.

Figure 4.5 demonstrates a dependence of the effective indices of the air guided modes on wavelength within the low loss bandwidth. By red dots are marked the first 4 full vectorial mode groups that exist within the low loss region from approximately 1510nm to 1560nm. Their intensity distributions are represented along the side of the graph.

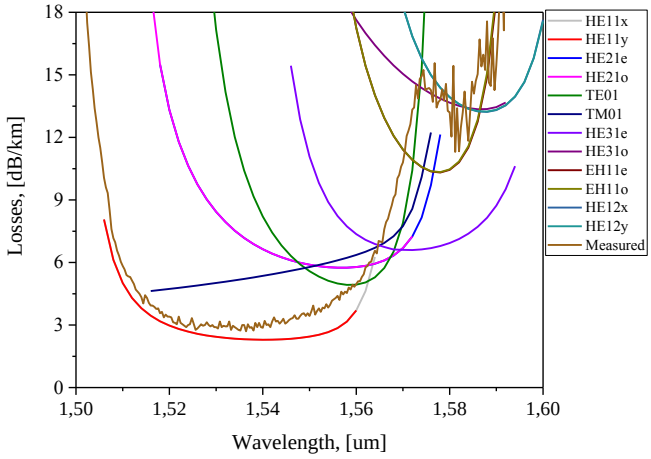

Fig. 4.6 A comparison of the measured and numerically calculated modal losses.

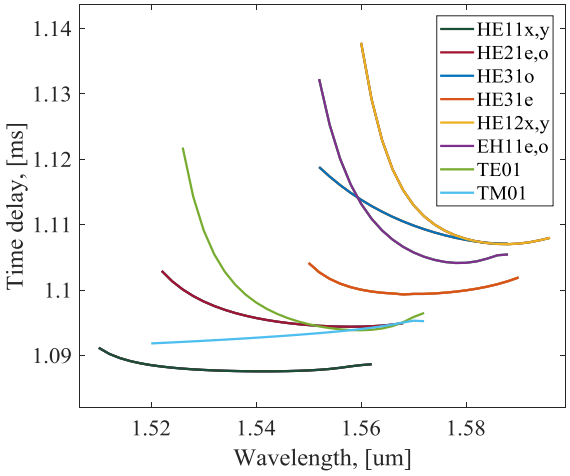

Fig. 4.7 The numerically calculated intermodal time delay for the first 4 groups of modes.

Table 4.3 The difference in the numerical effective refractive indices at 1550nm.

Modes	$n_i - n_j$
HE_{11}^{x}-HE_{11}^{y}	$0.003{\cdot}10^{-6}$
HE_{21}-HE_{21}^{o}	$0.01{\cdot}10^{-6}$
$HE_{21}^{e,o}$-TM_{01}	$2.69{\cdot}10^{-4}$
$HE_{21}^{e,o}$-TE_{01}	$2.2{\cdot}10^{-4}$
HE_{31}^{e}-HE_{31}^{o}	$5.3{\cdot}10^{-4}$
EH_{11}^{e}-EH_{11}^{o}	$0.004{\cdot}10^{-6}$

A comparison between measured and calculated losses for the 19-cell HC PBGF is depicted in Figure 4.6. Total losses are estimated as a sum of the confinement (CL) and scattering (SL) losses (Eq.(2.31)-(2.32) Section 2.5). Nevertheless, the edges of the low loss transmission bandwidth are in agreement for the simulation and measurement, the average level of simulated losses is approximately 1dB/km less. Losses of the first group of HOMs HE_{21a} and HE_{21b} are approximately 5.89 dB/km at 1550nm, that is $\sim$2.4 times higher than for the FM. At wavelength range from 1565nm to 1600nm, where HE_{11} is strongly attenuated, it might be assumed that light is carried mainly by the HOMs, transmission bands of which are shifted to longer wavelengths.

From the numerically calculated effective refractive indices are derived time delays for the modes travelling along 325m of the 19-cell HC PBGF [Figure 4.7]. Thus, the HOMs are delayed comparing to the FM on 6ns for HE_{21}, 12ns for HE_{31e} and 27ns for HE_{31o},and 28ns for EH_{11}. The differential time delay is calculated at wavelength of 1558nm, that is an operation wavelength of a time-of-flight set-up used for the fibre characterization in Chapter 5.

In the beginning of the current chapter, one of the main motivations for the 19-cell HC PBGF modelling was a verification of its implementation as a medium for data transmission under MDM scenario. The

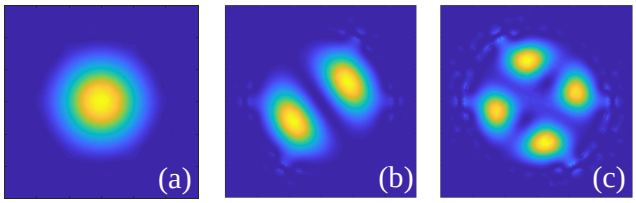

Fig. 4.8 LP_{ml} modes as a result of superposition of the corresponding full vectorial modes.

modes presented in Figure 4.5 are full vectorial modes. However, in real fibres due to imperfection of the geometry and induced stress or bend, the full vectorial modes propagate as a combination of modes, for example, as those described in Chapter 2 as LP_{ml} modes. An intermodal coupling within the corresponding modal groups brings one of the main limitations for the MDM systems, namely a cross-talk between channels. Reduction of the mode coupling can be achieved by an appropriate design of a fibre with separation between refractive indices more than 10^{-4} [49]. Table 4.3 demonstrates the numerically calculated refractive index difference between different modes at wavelength of 1550nm. As can be seen from Table 4.3, the splitting in indices for TM_{01}, $HE_{21}^{e,o}$ and TE_{01} exceeds 10^{-4}. According to a description of relation between vectorial and linearly polarized modes described in Table 2.1 from Chapter 2, for the 19-cell HC PBGF can be derived a set of LP modes, particularly LP_{01}, $LP_{11}^{a,b}$, $LP_{21}^{a,b}$ and LP_{02}. The suffixes "a" and "b" are used for two degenerate modes that also exist in two orthogonal polarizations. Examples of the aforesaid modes are depicted in Figure 4.8 (a),(b) and (c). (Since a considerable part of the field of LP_{02} penetrates into the cladding and its calculated loss is the highest among all simulated modes, it was disregarded.)

Another peculiar type of modes, that is in focus of many recent researches, are orbital angular momentum modes (OAMs). OAMs possess

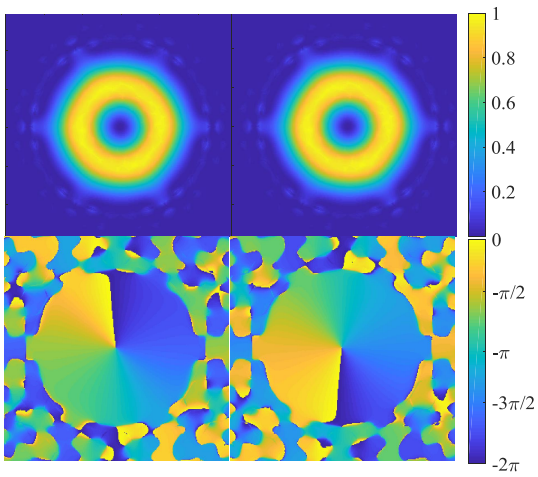

Fig. 4.9 $\pm$ 1 OAM modes combined from $HE_{21}^{o,e}$.

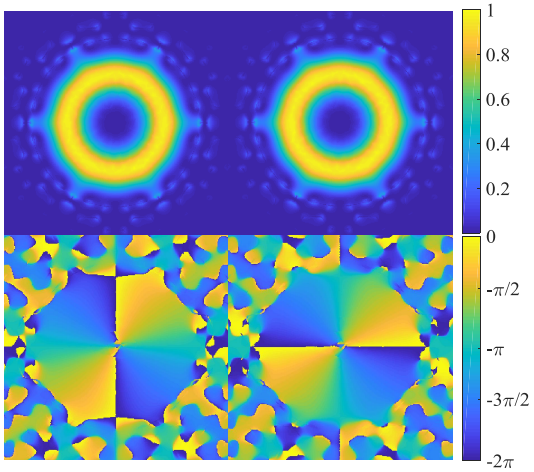

Fig. 4.10 $\pm$ 2 OAM modes combined from $HE_{31}^{o,e}$.

spatial polarisation and have a characteristic annular shape preserving phase singularity, a point where phase is unidentified. The wavefront of light is curled about the optical axis due to the spiral phase of vortex around the singularity point [80]. The expression for light carrying the orbital angular momentum was derived by Poynting in the beginning of the 19th-century [78] and it took almost a decade to prove the theory by an experimental demonstration performed by Beth [8], who showed that a circularly polarised light transmitted through the half-wave plate imparts a rotation to the wave-plate. Much more later by Allen [5] was considered that OAM is also present in Laguerre-Gaussian (LG) laser beams, the complex amplitude of which in the waist plane of the beam is [49]

$$\Psi_{l,p}(r,\phi) = \frac{C_{lp}}{\omega_0}\left(\frac{r\sqrt{2}}{\omega_0}\right)^{|l|} L_p^{|l|}\left(\frac{2r^2}{\omega_0^2}\right) exp\left(-\frac{r^2}{\omega_0^2}\right)\exp(il\phi), \quad (4.2)$$

where C_{lp} is the normalization term of the amplitude, ω_0 is the waist size of the beam and $L_p^{|l|}$ is the Laguerre polynomial. The integer l represents the topological charge of the LG mode and can be positive or negative depending on the handiness of the twist. Another integer, p, is determined by the number of nodes in radial direction. The most important part of Eq.(4.2) is the last exponential term $\exp(il\phi)$, since it represents the characteristic helical phase front intrinsic to LG beams. In the case, when $l = p = 0$ the solutions of Eq.(4.2) is reduced to the fundamental Gaussian beam solution. One can quantify the energy ratio carried by an OAM beam as l/ω, where ω is angular frequency of light, and LG beam carries an OAM of $l\hbar$ per photon. In communication were already demonstrated several experiments [64, 38, 43, 13] that took advantage of the orthogonally of OAMs as independent carries of data. In a case of an optical fibre, according to Ramachandran *et al.* in

Ref.[80] the OAMs can be presented as a $\pi/2$-shifted linear combination of the vectorial modes:

$$\begin{aligned} HE^{e}_{2,m} \pm iHE^{o}_{2,m} &= F_{1,m}(r)\left(\hat{\sigma}^{\pm} exp(\pm i\phi)\right),\ p=0, l=1, \\ HE^{e}_{l+1,m} \pm iHE^{o}_{l+1,m} &= F_{l,m}\left(\hat{\sigma}^{\pm} exp(\pm i\phi)\right),\ p=0, l>1, \\ EH^{e}_{l-1,m} \pm iEH^{o}_{l-1,m} &= F_{l,m}\left(\hat{\sigma}^{\mp} exp(\pm i\phi)\right),\ p=0, l>1, \end{aligned} \tag{4.3}$$

where $F_{1,m}$ and $F_{l,m}$ are corresponding radial field distributions of the LP modes and $\hat{\sigma}^{\pm} = \hat{x} + i\hat{y}$ denotes the right or left handed circular polarization, that determines also a spin angular momentum (SAM) of a beam of value $\sigma\hbar$, where depending on handiness of polarization σ is equal ± 1.

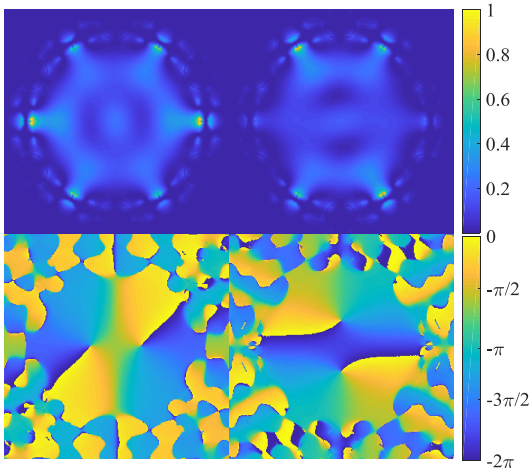

Fig. 4.11 $\pm$ 2 OAM modes combined from $EH^{o,e}_{11}$.

Following Eq.(4.3), exported from COMSOL electric fields of the modes are combined in corresponding OAM modes depicted in Figure 4.9-4.11. It is apparently, that ± 1 OAM [Figure 4.9], combined from $HE^{e,o}_{21}$ according to the first equation in Eq.(4.3), preserves an unique

circular distribution of its intensity with a hollow center, while the phase distribution has a characteristic jump in a pattern from 0 to 2π around the singularity point. Figure 4.10 depicts $\pm$2OAM mode as a combination of HE_{31}^{o} and HE_{31}^{e}. Its intensity distribution is also unique and the phase has a double twist from 0 to 2π around the singularity point. However, the 19-cell HC PBGF have a C_{6v} symmetry, which means that its cross-section possesses a sixfold rotation symmetry in addition to a mirror symmetry, hence the modes $HE_{3p,m}$ and $EH_{3p,m}$, where p is an integer, are split into two non-degenerate modes in a contrast to conventional fibres with a $C_{\infty v}$ symmetry, where corresponding two modes are degenerate [40, 1]. From Table 4.3 can be seen that the splitting in the effective indices for $HE_{31}^{o,e}$ is in 2 orders higher than, for example, for $HE_{21}^{o,e}$ modes and is equal $5.3{\cdot}10^{-4}$. Therefore, it was concluded that propagation of $\pm$2OAMs, as linear combination of HE_{31}^{o} and HE_{31}^{e} modes, in the 19-cell HC PBGF is improbable. Figure 4.11 shows OAM mode formed by $EH_{11}^{o,e}$. Neither its intensity nor phase distributions possesses characteristic profiles. By this reason the current combination of modes cannot be considerate being OAM mode.

Results of the modelling presented in the current chapter allow to conclude a possibility of the 19-cell HC PBGF implementation in a MDM scenario. According to the model along a low loss bandwidth the fibre supports 4 groups of the full vectorial modes. At least 2 of them ($HE_{11}^{x,y}$ and $HE_{21}^{o,e}$) are well confined and exhibit a relatively low loss. Aforesaid modes can be guided in the fibre as LP_{ml} modes or optical vortices that carry OAM states. The next chapter will present detailed experimental characterisation of the fibre as well as describe challenges of OAMs propagation in the 19-cell HC PBGF.

Chapter 5

Experimental characterisation of the 19-cell HC PBGF

Optical fibre as a key component of optical fibre communication systems have been playing an important role in delivering a growing amount of data to users all round the world. However, information traffic of networks is exponentially growing, demanding even higher information capacity of communication links. On the other hand, noise-to-single ratio of transmitted signals imposes an upper limit on capacity of a given fibre channel over a given transmission distance. The conclusion of the limited fibre capacity was derived by Shannon[21, 94, 23] and its existence leads to a possible capacity crunch of optical network systems. The problem has already attracted attention of researchers and scientists all over the world in attempt to find an appropriate solution. Among all dimensions for the data signal multiplexing as time, frequency, polarisation and phase, only spatial dimension has not been utilized. The latest technological advancement of communication systems as well as development of techniques for design and manufacturing of optical fibres with advanced properties, permits to take advantage of spatial fibre

modes as separate channels for data transmission using mode division multiplexing[83].

Among recently reported demonstrations of data transmission under MDM scenario can be accented a transmission in a few mode fibre of 2 LP modes over 96km with 6x6 MIMO post processing [89] and 4 LP modes over 130km with 12x12 MIMO[88], transmission of 9 LP modes in a multi-mode fibre over 22.8 km using 30x30 MIMO post processing [27] and parallel transmission of 2 LP modes over 146 wavelength channels over 500km [44]. Except LP modes there is an another type of modes that received an enormous attention, known as OAM modes in a fibre. Transmission of 12 OAM modes over a kilometer-length for a specially designed ring-fibre was reported in Ref.[36, 43]. Also was demonstrated transmission of OAM over longer transmission distance of 13.4km [38]. Simultaneously, an implementation of HC PBGFs as a transmission medium for MDM was shown in transmission of 2 LP modes over 30m of 7-cell HC-PBGF [110], over 193m of 19-cell HC PBGF[17] and transmission over 310m of 37-cell HC PBGFs in combination with WDM over 96 channels [95]. Common challenges for all types of HC PBGFs implemented in MDM are a limited low-loss transmission bandwidth due to the presence of the surface modes (SMs) and relatively high loss due to scattering at the surface roughness.

In Chapter 4 was presented a model of the 19-cell HC PBGF with the anti-resonant elements (AREs) introduced at the core-cladding interface. Due to the AREs the fibre loss were suppressed below 5.5dB within 3dB bandwidth at C-band. According to the model, the 19-cell HC PBGF supports 2 groups of full vectorial modes within almost the whole bandwidth of the low loss window, that can create 2 groups of LP modes (LP_{01}, LP_{11}) or 2 groups of OAM modes (with a topological charge of l=0, $\pm$1). Nevertheless, HC PBGFs were explored for transmission of LP modes in MDM systems, the propagation of OAM states in that type of fibre has not been demonstrated yet. However, a theoretical

prediction that a HC PBGF can support OAM modes was reported in Ref.[54, 56, 55].

Being intrigued by a low loss performance of the 19-cell HC PBGF and a theoretical envision of OAM states supported by the fibre, an experimental excitation and propagation of OAM states in the HC PBGF are carried out and described in this Chapter. A first section of the Chapter 5 is focused on a detailed experimental characterisation of the 19-cell HC PBGF, which is performed with a S^2 imaging technique with a spectrogram approach. While in a second section are described challenges, that were met during a multiplexing and demultiplexing of OAM states excited in the 19-cell HC PBGF.

5.1 Experimental characterisation of the fibre

Experimental characterisation of the 19-cell HC PBGF is performed with a modified S^2 imaging technique, the schematic set-up of which is depicted in Figure 3.33 (b). The choice of the current approach for the modal content detection was made based on the available equipment. As a light source is used a tunable laser ANDO4321 with a maximum wavelength resolution of 1pm and a scanning wavelength range from 1520nm to 1620nm. Light is coupled into 10m of the FUT and at the fibre output it is focused on InGaAs camera (Xenics [109], 100Hz frame rate, 14-bit).

Following the modified S^2 method, the magnified near-field image of the fibre output is captured by the camera at each scanning wavelength of the sweep source within a narrow wavelength window. Calculating the Fourier transform at each *(x,y)* point of images along the whole scanned wavelength range, one derives Fourier spectra, that gives a dependence of the Fourier amplitude of the intermodal beats on the intermodal time delays. Summing the obtained Fourier transforms over all pixels, one obtains a S^2 trace measured at a central wavelength of the scanned

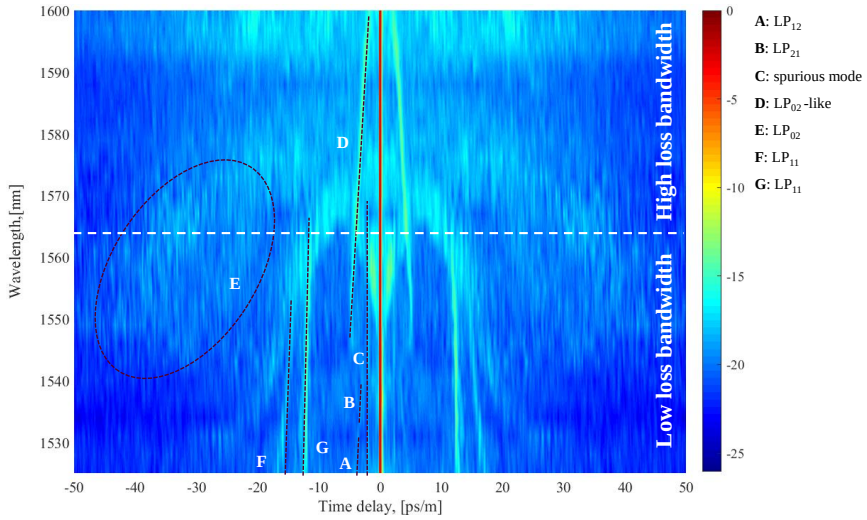

Fig. 5.1 A spectrogram measured by the S^2 imaging technique along wavelength range from 1525nm to 1600nm for 10m of the FUT. Time delay axis is normalized to ps/m units. A positive values of time delays correspond to a real measurement, while a spectrogram at the negative axis is a mirrored reflection of the positive axis.

wavelength range. Further modal reconstruction is performed according to the original S^2 technique [65], briefly described in Section 3.2.5.

For the FUT characterisation was implemented a spectrogram approach, previously described in Ref. [46, 66, 35]. A narrow wavelength window of 8.192nm with a resolution of 4pm was swept along a wavelength range from 1525nm to 1600nm in a wavelength step of 3nm. Subsequently, the spectrogram is assembled from all S^2 traces measured along scanning wavelength range. A relative power between the dominant and other propagating modes is found as a ratio between peak amplitudes at a corresponding time delay for a mode of interest and a dominant mode.

One of the limitations of the S^2 approach is based on an assumption that in a fibre one of the propagating modes is dominant, while a relative power of other modes is small. For the 19-cell HC PBGF at a low

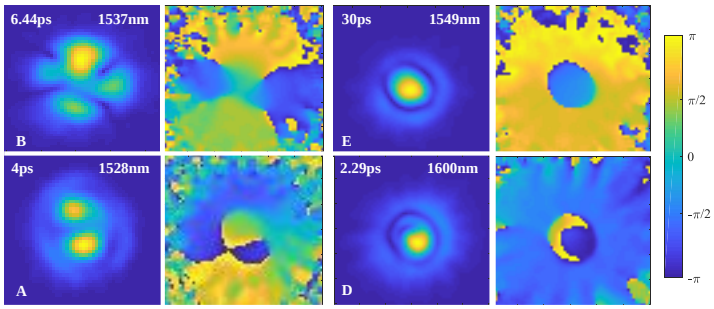

Fig. 5.2 The intensity and phase distributions of the C,D,E,F modes.

loss bandwidth [Figure 5.1, shorter wavelengths] the loss of the FM is less than 5dB/km [Figure 4.2,black curve]. However, approaching wavelength of 1565nm, marked by a dashed white line in Figure 5.1, the loss of the FM increases due to the present surface modes. Therefore, it could be assumed that within the high loss bandwidth, one of the HOMs becomes a dominant mode in the fibre or possesses an equal modal power as the FM. An aforesaid circumstance could bring uncertainties in the modal characterisation for the S^2 method at the longer wavelengths.

Figure 5.1 shows a spectrogram measured for 10m of the FUT along wavelength range from 1525nm to 1600nm. The axis of time delays is normalised to the fibre length to obtain units of ps/m. The initial coupling is performed at 1550nm for the FM as a dominant mode. The description of the modes in Figure 5.1 follows. A trace *A* corresponds to LP_{12} that is present along a wavelength range from 1525nm to 1531nm and afterwards is "replaced" by a trace *B*, which is LP_{21} present from 1534nm to 1540nm. A trace *C* appears along a scanning wavelengths range from 1525nm to approximately 1555nm at the same time delay of $\sim$2.2ps and is considered being a spurious mode. Its reconstruction did not give any specific mode. By the trace *D* is marked LP_{02} mode, that is also detected within a broad region E. The last two sharp traces of G

and F correspond to LP_{11} modes clearly present and reconstructed until wavelength of 1573nm.

Figure 5.2 demonstrates the reconstructed intensity and phase distributions for the modes picked up from regions A,B,D and E at different wavelengths. The phase distributions are obtained from the Fourier spectra at the corresponding time delays. Nevertheless, all reconstructed modes resemble the intensity and phase distributions of LP_{12} (A), LP_{21} (B) and LP_{02} (D,E), it is obvious from reconstruction that they are not pure and affected by other modes. From the reconstruction of the trace D at the wavelength of 1600nm in Figure 5.2 may be noticed a component of a surface mode present at the outer edge of the reconstructed intensity. Development of LP_{11} modes (the traces G and F) along wavelengths are analysed as separate S^2 traces picked up from the spectrogram [Figure 5.1] at wavelengths 1525nm[Figure 5.3] ,1540nm[Figure 5.4] ,1552nm[Figure 5.5] ,1570nm[Figure 5.6] and 1591nm[Figure 5.7]. They reveal several interesting features and further discussed below in more detail.

In Figure 5.3, that depicts the S^2 trace measured at wavelength of 1525nm, are detected two sharp peaks 2 and 3, which represent $LP_{11a,b}$ modes from the traces G and F at time delays close to 12.4ps and 16.4ps. Also two LP_{12}-like modes are discovered at 10.07ps (the trace A) and 28.58ps. Worth mentioning, that a dominant mode in the FUT, inset in Figure 5.3, resembles a mixture of LP_{01} and LP_{11} modes.

At wavelength of 1540nm 3 distinct LP_{11} modes exist with time delays corresponding to approximately 12.3ps, 15ps and 18.2ps. The peaks marked by numbers 1 and 2, that correspond to LP_{11} modes from the traces G and F, can be assumed to be $LP_{11a,b}$ resembling the same polarisation and the third peak, marked as F_2, since it appears from a side of the trace F, is LP_{11a} in the orthogonal polarisation. At longer time delays only LP_{02} mode is detected over a broad range from approximately 30ps/m to 70ps/m. Its reconstructed intensity profile is depicted in Figure

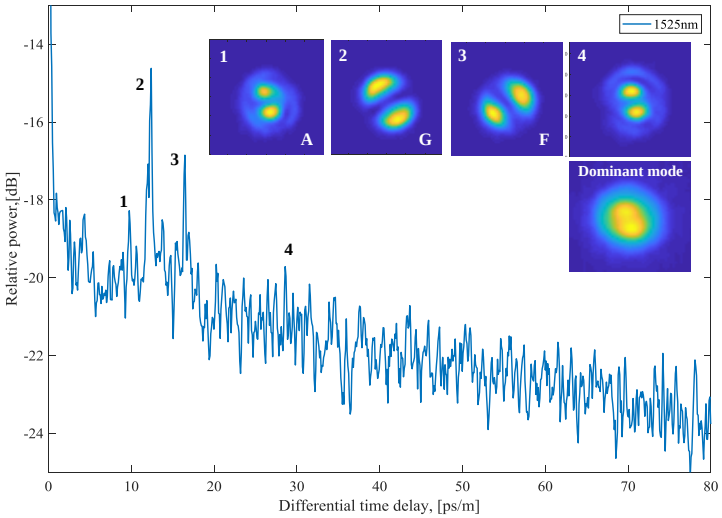

Fig. 5.3 The S^2 trace measured at 1525nm and the intensity reconstructions of the first 4 strongest peaks that reveal 2 LP_{11}-like and 2 LP_{12}-like modes.

5.4 as inset 4. From 1552nm in the S^2 trace appears a sharp evident peak at 5.25ps/m, which corresponds to LP_{02}-like mode, an intensity distribution of which is affected by the presence of the surface mode, especially at longer wavelengths. All other extracted modes at 1552nm [Figure 5.5] are similar to those detected at 1540nm [Figure 5.4]. Along the whole range of wavelengths the first LP_{11a} (G) mode is strong and evident comparing to other modes from LP_{11} group, that are decreased in power and experience an influence from each other. LP_{11} (G,F) group of modes becomes less evident with increase of wavelengths and are hardly resolvable at wavelengths longer than 1573nm. Already at 1570nm [Figure 5.6] the reconstruction of G and F is blurred and at the S^2 trace they appear being squeezed between a sharp LP_{02}-like mode at short time delays and a broad distribution of LP_{02} mode at longer time delays. It is remarkable, that along the whole wavelength range from 1525nm to 1573nm were not reconstructed all 4 clear LP_{11} modes

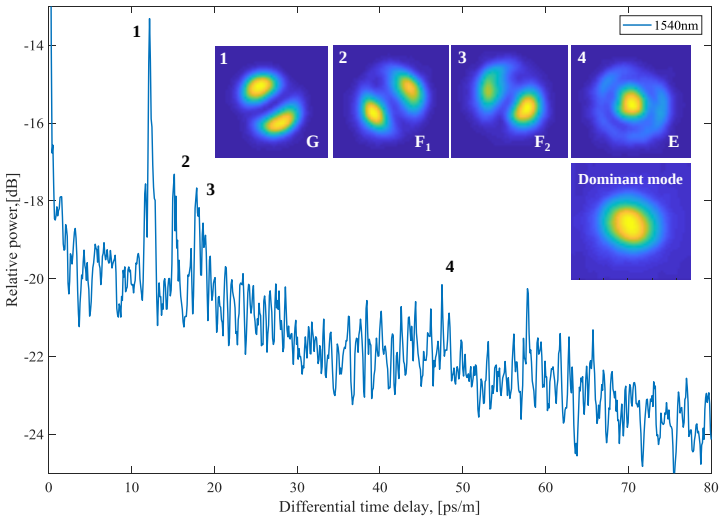

Fig. 5.4 The S^2 trace measured at 1540nm and the intensity reconstructions of the first 4 strongest peaks that reveal 3 LP_{11}-like and LP_{02}-like modes.

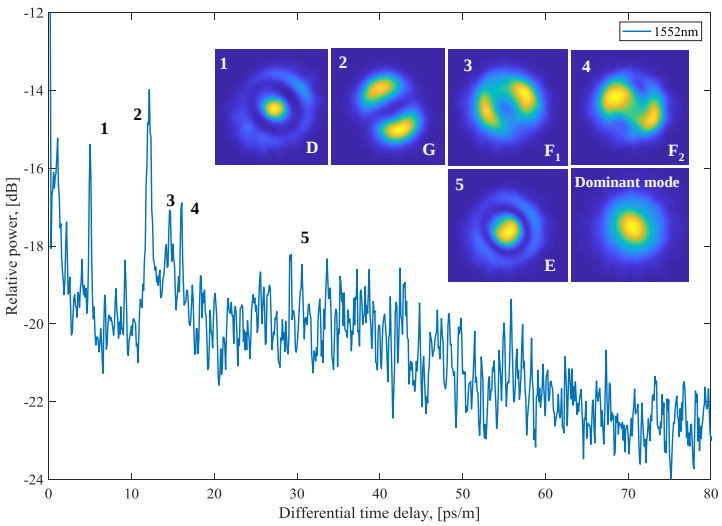

Fig. 5.5 The S^2 trace measured at 1552nm and the intensity reconstructions of the first 5 strongest peaks that reveal 3 LP_{11}-like and 2 LP_{02}-like modes.

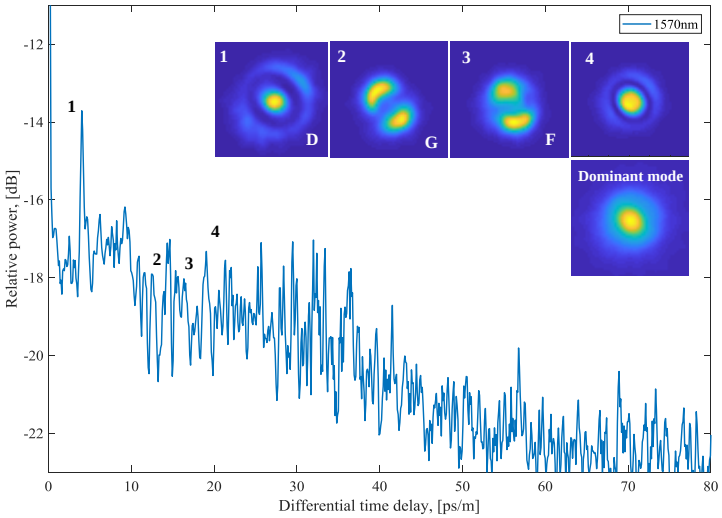

Fig. 5.6 The S^2 trace measured at 1570nm and the intensity reconstructions of the first 4 strongest peaks that reveal 2 LP_{11}-like and 2 LP_{02}-like modes.

simultaneously present at the S^2 trace. According to the model described in Chapter 4 at the wavelength of 1550nm three of the ideal modes, TE_{01} and $HE_{21}^{o,e}$ coincide, preserving the same differential time delay corresponding to the FM [Figure 5.8(a)]. Thus, resulting in one distinct LP_{11} mode, like the one from the trace G [Figure 5.1], for example, and three other LP_{11} modes propagating with a small intermodal delay between each other. Perhaps, for the longer length of the fibre all four LP_{11} modes of different geometrical orientations are more separated in the group delays as it was noticed in Ref.[66]. However, the range of time delays achieved for the current S^2 set-up was insufficient to cover the whole range of time delays of 325m of the FUT. Therefore, to monitor differential times delays and launching conditions of mode for the whole span of the FUT is implemented a time-of-flight technique, as discussed in Section 5.2. Figure 5.7 shows the S^2 trace measured at 1591nm. All reconstructed intensity distributions of modes exhibit a

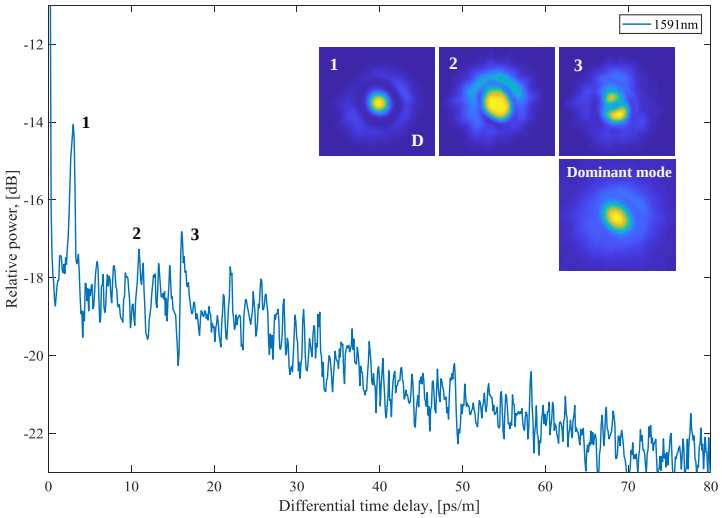

Fig. 5.7 The S^2 trace measured at 1591nm and the intensity reconstruction of the first 3 strongest peaks that reveals LP_{02}-like modes and mixture of modes.

strong influence from the surface modes and the dominant mode resolves LP_{02}-like mode.

An evaluation of the spectrogram [Figure 5.1] and separately analysed S^2 traces [Figure 5.3-5.7] allow to conclude that around wavelength of 1565nm the FM experiences attenuation, while LP_{02} comes into play at longer wavelengths. An interesting feature is a general modal behaviour within the low loss [Figure 5.1, shorter wavelengths] and high loss regions [Figure 5.1, longer wavelengths]. The discrete scattering modes, represented as narrow trails in the low loss region, stream into a continuum of the mixed modes in the high loss region, present over a broad range of time delays. Similar results were reported in Ref.[66], where 19-cell HC PBGF without ARE was tested by the S^2 technique.

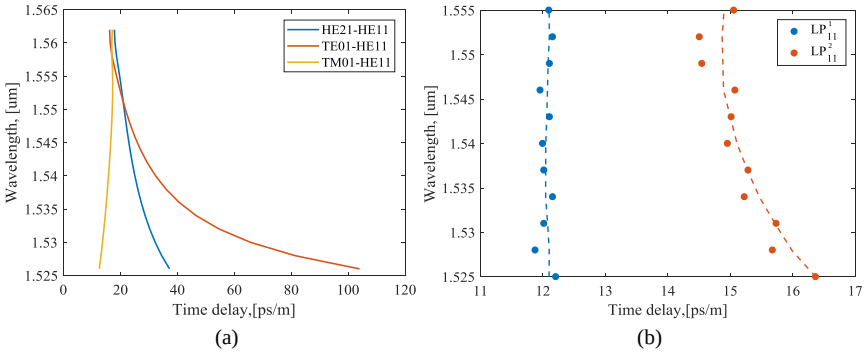

Fig. 5.8 The comparison of (a) the numerically and (b) the measured differential time delays for LP_{11} modes (G,F).

Figure 5.8(a) and (b) show a comparison of the differential time delays (DTDs) numerically calculated for the ideal modes belonging to LP_{11} group and the measured DTDs for LP_{11} modes from trails F and G on the spectrogram [Figure 5.1]. Despite an evident difference, especially at shorter wavelengths, between the calculated and measured DTDs, there is a common tendency of modes to approach each other at longer wavelengths. Numerical prediction is made for an idealized fibre geometry, while in the real fibre due to defects at the core-cladding boundary as well as due to imperfection of the geometry, the propagating modes are a mixture of the ideal modes. Structural distortions of the real fibre's cross-section make modelling of HC PBGF complicated and a certain difference between results of the fibre simulation and measurement is expected.

The S^2 set-up for a spectrogram characterisation of the 19-cell HC PBGF discussed previously in the section does not resolve polarisation. As it was already mentioned, that along the whole range of the scanned wavelengths simultaneous presence of all four LP_{11} was not detected. Consequently, to investigate a dependence of LP_{11} modes on the input state of polarisation, in the set-up before the FUT are introduced a

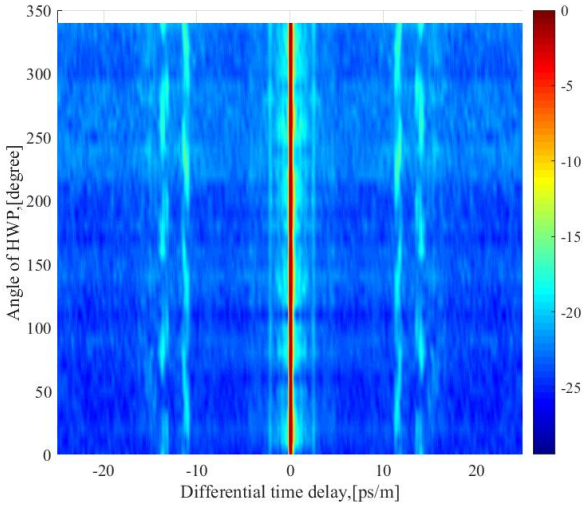

Fig. 5.9 A S^2 spectrogram acquired for the different launching polarisation orientations.

linear polariser and a half-wave plate (HWP), rotation of which is controlled by a computer. The S^2 measurements are performed at the central wavelength of 1550nm every 10^o of the HWP rotation and afterwards combined into a polarisation dependent spectrogram depicted in Figure 5.9. Two evident trails in the spectrogram [Figure 5.9] correspond to orthogonally polarised LP_{11}. A dependence of their relative power on a angle of HWP rotation is shown in Figure 5.10, exhibiting a clear correlation in polarisation orientations. Other two LP_{11} modes were hardly resolvable during the measurement and did not preserve a clear polarisation dependence neither reconstruction. Results of the polarisation measurement may be interpreted as strongly coupled $TE_{01} \pm HE_{21}$ and $TM_{01} \pm HE_{21}$ modes.

Further investigation of the 19-cell HC PBGF is performed for OAM fibre modes, experimental propagation of which in HC PBGF has not been yet reported. Aiming for an additional investigation, 325m of the 19-cell HC PBGF was examined for excitation, multiplexing, propagation

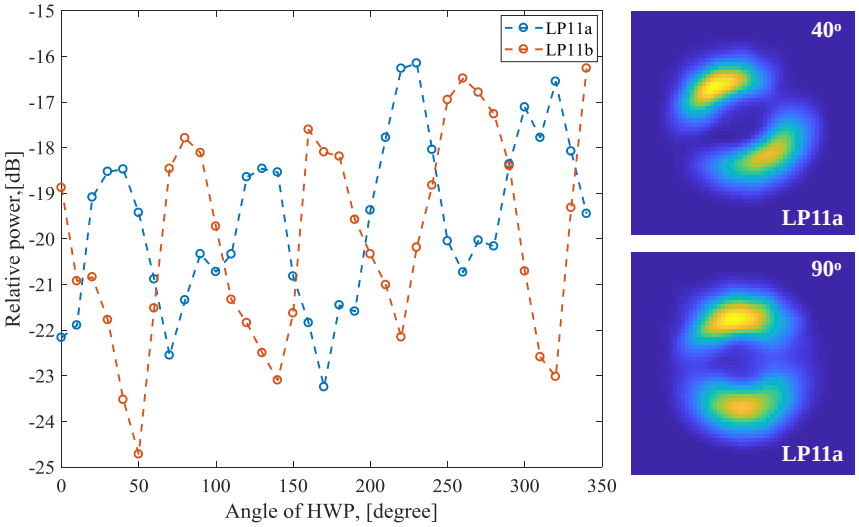

Fig. 5.10 Dependence of a relative modal power of LP_{11a} on an angle of the HWP. Insets show reconstructed modal intensity at the peaks of 40^o and 90^o for each of LP_{11a} mode.

and demultiplexing of OAM modes. Results of investigation and final conclusion are presented in the next section.

5.2 The 19-cell HC PBGF in the MUX and DeMUX set-up for OAM modes

In a long section of a fibre a differential mode delay can be measured by an arrival time of ps pulses launched simultaneously into different modes. Such type of measurement is known as a time-of-flight (ToF) technique. Its advantage is a real-time evaluation of the coupling conditions and intermodal time delays. On the other hand, the method does not allow

to reconstruct the propagating modes and is used in combination with a theoretical model or another characterisation technique.

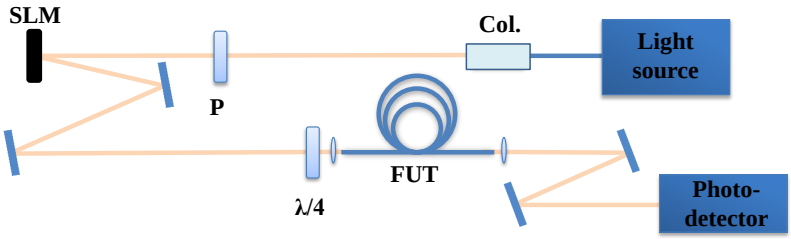

Fig. 5.11 A schematic representation of the set-up for the time of flight measurement. Here, Col. stands for a collimator, P - polariser, $\lambda/4$ - a quarter-wave plate, SLM - a spatial light modulator, FUT - the fibre under test.

The ToF measurement is carried out with a mode-locked ps pulse laser (a repetition rate of 15.3MHz and a bandwidth of approximately 11nm) operating at central wavelength of 1558nm and coupled into approximately 325m of the 19-cell HC PBGF. At the fibre output light is focused on a 5GHz photodetector connected to a 10 GHz bandwidth sampling oscilloscope, which is triggered by the pulsed laser. Figure 5.11 shows a scheme of the ToF set-up used for characterisation of the FUT, when OAM modes, generated by a spatial light modulator (SLM), are coupled into the fibre. Collimated beam from a pulse laser is directed onto SLM, through a polariser, since the best conversion at SLM is only achieved for the incoming light beams in a horizontal linear polarisation. Digitally created hologram at SLM converts incoming Gaussian beam into a beam of annular shape, while by the quarter wave

plate (QWP) at the input of the FUT linearly polarised light is converted into circularly polarised. An excited OAM mode is characterised by a topological charge $|l|$, defined by the amount of 2π phase jumps around the singularity point, where phase is not defined.

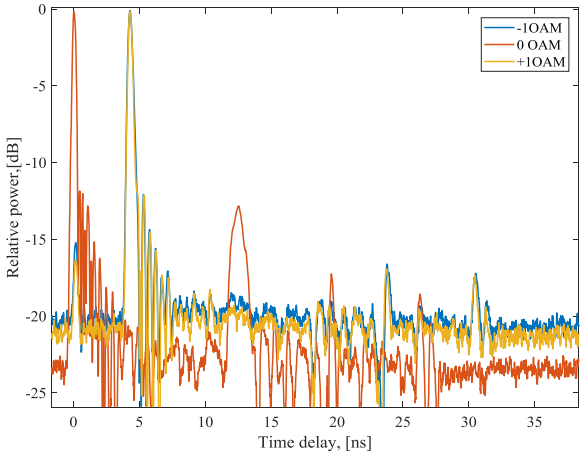

Fig. 5.12 Time-of-flight traces for the launched into the FUT 0, and ± 1 order of OAM modes at wavelength of 1558nm.

Measured traces of the temporal impulse response for 0 and ± 1 order OAMs are depicted in Figure 5.12. Peaks, that appear at 19.6ns, 26.3nm and 27ns for 0 OAM mode and at 23.9ns, 30.6ns and 31.3ns for ± 1 OAM modes are considered artificial, since they appear at the same time delay from the highest peak for all excited modes. In the trace obtained for OAM mode of $l = 0$ [Figure 5.12], around 12.45ns is present a peak, position of which corresponds to position of the flat LP_{02} plateau, detected by the S^2 imaging in the previous section. Aforementioned peak is intrinsic only for the coupled fundamental mode and its amplitude decreases, when any of the modes from the LP_{11} group is coupled into the fibre. Deliberately excited LP_{02} does not change the ToF trace, which remains similar to the pulse response of the FM mode. A relative power of the aforesaid peak has never exceeded the values of -10dB.

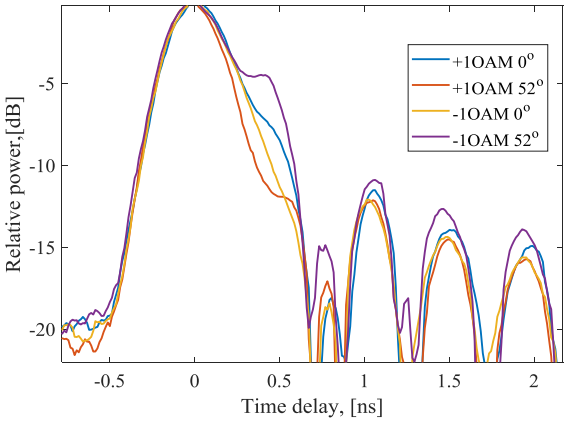

Fig. 5.13 Time-of-flight traces measured for the launched into the FUT 0 and ± 1 order of OAM modes at the central wavelength of 1558nm.

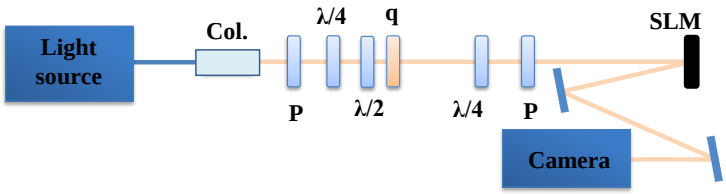

Fig. 5.14 A schematic representation of the set-up for a back-to-back measurement. Here, Col. stands for a collimator, P - a polariser, q - is a Q-plate, $\lambda/2$ - a half-wave plate, $\lambda/4$ - a quarter-wave plate, FUT - the fibre under test.

A relative mode purity is calculated according Ref.[36, 37] as multi-path interference:

$$MPI = 10log_{10}\frac{P_j - \overline{P}_{noise}}{P_k - \overline{P}_{noise}}, \tag{5.1}$$

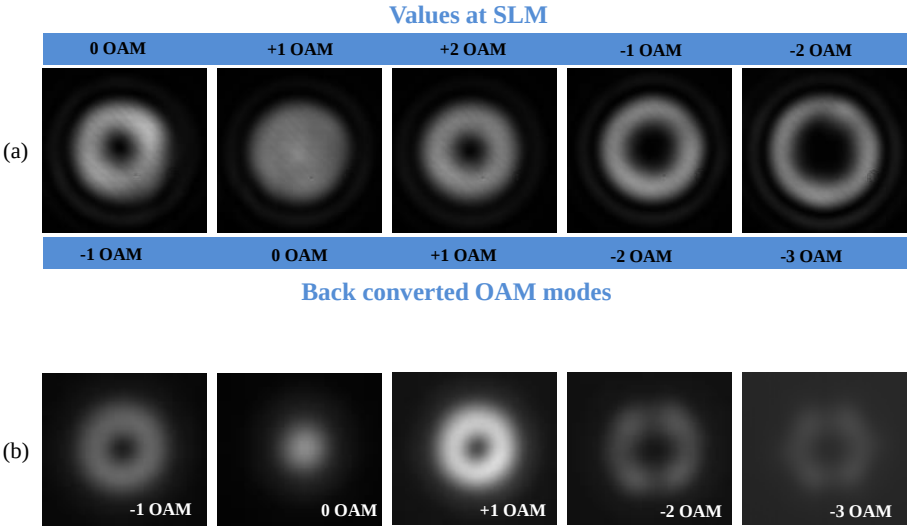

Fig. 5.15 (a) The images of OAMs excited by Q-plate and back converted by SLM to 0, ± 1, -2 and -3 orders. (b) The intensity profiles of the coupled into the FUT OAM modes of orders 0, ± 1, -2 and -3 orders captured by the camera at the output of the 19-cell HC PBGF.

where P_j is an amplitude of a modal peak for which MPI values is calculated, P_k is an amplitude of the peak for the kth mode present on the trace and $\overline{P}_{noise}$ is an average noise level.

From Eq.(5.1) MPI values are found to be: -13.9dB for the FM, -18.8dB for +1 OAM mode and -19.07dB for -1 OAM mode. It is also worth mentioning, that a relatively pure excitation of -1 OAM mode is reached at an angle of the QWP $\theta = 0^o$, while for +1 OAM $\theta = 52^o$. In the case of any other value of θ, at the ToF trace is noticed an additional peak stronger than -10dB of the relative power and delayed by 0.5ns from ± 1 OAM, which can be observed in Figure 5.13. For the clarity of explanation, the position of the peak center for ± 1 OAM was moved to

time delay τ =0. Following the simulation and numerically calculated modal time delays [Figure 4.7], at wavelength of 1558nm the intermodal delays of $HE_{21} - TE_{01}$ is 0.52ns and $HE_{21} - TM_{01}$ is 0.51ns. Therefore, the additional peak on the ToF trace for ± 1 OAM can originate in non-degenerate TE_{01} and TM_{01} modes.

Results obtained by the ToF measurement for OAM modes of order l=0,$\pm$1 were promising enough to investigate the simultaneous excitation and coupling of the aforesaid modes in the FUT. Supplementary to the excitation by SLM was added an excitation by a "Q-plate", a birefringent wave-plate with a layer of a liquid crystal (LC) polymer [14, 96]. Q-plate converts an incoming Gaussian beam into an optical vortex,that carries OAM state.

Q-plate possesses its own characteristic half-integer q ($|l| = 2q$) and performers a transformation of incoming light [37] equal to:

$$q \cdot \left(A\widehat{\sigma}^{+} + B\widehat{\sigma}^{-}\right) = \left(A\widehat{\sigma}^{-}e^{i2q\phi} + B\widehat{\sigma}^{+}e^{-i2q\phi}\right), \tag{5.2}$$

where A and B are the input polarisation states, $2q$ is imposed by the Q-plate order of OAM state. By a careful control of a polarisation state of an input beam a definite OAM fibre mode can be excited in the FUT. However, in a case of the first order OAM ($|l|$=1) particular attention has to be paid, since in a fibre it can exist only as a combination of $HE_{21}^{e,o}$ modes [Eq.(4.3) for $|l|$=1], forming an aligned OAM, for which the sign of the topological charge is similar with a sign of the handedness. Therefore, from the first group of HOMs can be created only two OAM modes, being $A\widehat{\sigma}^{-}e^{-i2q\phi}$ and $B\widehat{\sigma}^{+}e^{i2q\phi}$, while two another are a specific linear combination that exist as TE and TM modes. Generally, for $|l| > 1$ four OAM modes can exist as two aligned and two anti-aligned states[37, 80]. However, following the simulation made in Chapter 4, in the 19-cell HC PBGF cannot be excited and propagated OAM modes of orders higher than $|l| = 1$.

Performance of the Q-plate and efficiency of back conversion are analysed by a back-to-back(B2B) measurement, schematic representation of its set-up is depicted in Figure 5.14. A collimated beam from a ps pulsed laser source is incident on a polariser before a QWP to control incoming polarisation state of a beam. Q-plate (*Thorlabs* [103]) possesses a q-value of 1/2, the sign of which is converted by a HWP. In the measurement, excited modes are back converted at SLM, when a definite OAM mode of +1 or -1 orders is selected by the QWP. The back conversion is monitored by the camera and a single mode fibre, that is connected to a powermeter.

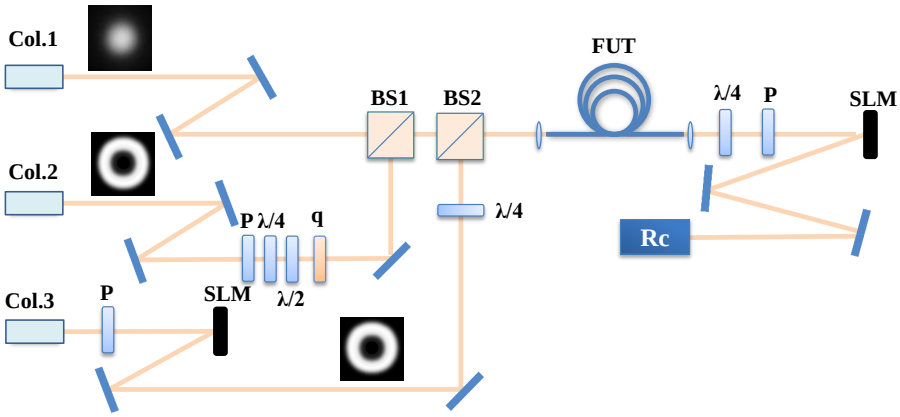

Fig. 5.16 A schematic representation of the set-up for multiplexing and demultiplexing of 0 and ± 1 OAMs states in the 19-cell HC PBGF. Col. is a collimator, P - polariser, q - Q-plate, $\lambda/4$ - quarter-wave plate, SLM - a spatial light modulator, BS - beam splitter, Rc. - receiver, FUT - the fibre under test.

An example of the back-to-back demultiplexing for -1 OAM mode excited by the Q-plate is demonstrated in Figure 5.15(a). Values above the pictures correspond to the generated at SLM holograms, while the

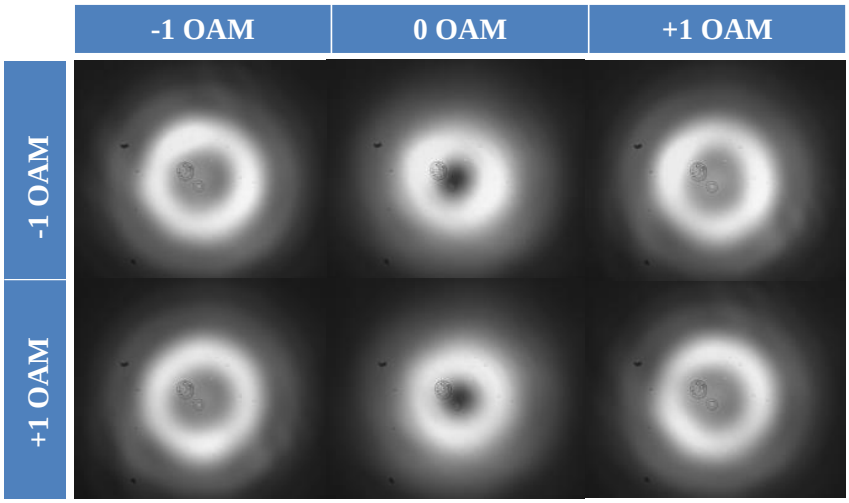

Fig. 5.17 Images of the demultiplexed by a SLM OAM modes with $|l| = 1$.

real values of the modes is denoted below the pictures. From Figure 5.15(a) can be observed a clear conversion of -1 OAM mode to a Gaus-

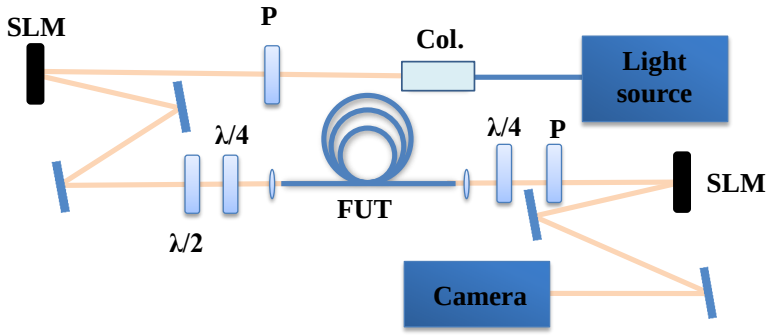

Fig. 5.18 A scheme of the set-up used for verification of the output polarisation of the 19-cell HC PBGF.

sian beam, when a pattern of +1 OAM is created at SLM. In the same manner are obtained the back converted OAM modes with topological charges of l=±1,-2 and -3. Figure 5.15(b) demonstrates the intensity profiles of 0,±1,-2 and -3 OAM modes after they have been launched and propagate in 325m of the FUT. As it can be seen from Figure 5.15(b), the second and third orders of OAM modes do not propagate in the 19-cell HC PBGF as OAM modes. Their intensity distributions are not unique and most probably resembles EH_{11} depicted in Figure 4.5.

Figure 5.16 shows a scheme of the set-up built for multiplexing and demultiplexing of 0 and ±1 orders of OAM modes coupled into the 19-cell HC PBGF. The set-up has 3 inputs. The first arm couples the FM into the fibre, the second arm is comprised from linear polariser, QWP, HWP and Q-plate for excitation of OAM mode with topological charge of l=+1, while the third arm is built from linear polariser and SLM for generation of -1 OAM mode. All inputs are launched into the FUT after being combined on beam splitters before the fibre input. Back conversion into a Gaussian beams is performed by QWP, linear polariser and SLM. Afterwards, back converted modes are coupled into a single-mode fibre. Figure 5.17 shows projected back OAM modes with l=±1. It is expected that -1 OAM is converted to a Gaussian beam at SLM, when a hologram of +1 OAM is chosen and vice versa. However, as it is seen from Figure 5.18, in both cases a projected back mode does not exhibit the expected Gaussian distribution neither for OAM modes generated by Q-plate nor by SLM at the input. A residual amount of the annular beam intensity is present for all back converted modes.

The problem of the back conversion could be a consequence of (a) bad coupling due to contaminated or not flat fibre cleaves, (b) wrong coupling lens or (c) due intrinsic properties of the fibre caused by mode mixture or random change of polarisation along the fibre. To check polarisation maintenance of the OAM modes along the fibre is used a set-up depicted in Figure 5.18. OAM modes are excited by SLM and

an optimal coupling is achieved by controlling an optical lens value. The circular polarisation at the fibre input was checked with a help of polarisation beam splitter and was aligned in a way to split light equally in both polarisations. Afterwards an angle at the QWP at the fibre output was changed and back conversion was verified by the camera. However, the results of demultiplexing, independent on the QWP angle, remained the same. Current the measurement shows that the polarisation state for the excited mode at the fibre output is neither circular nor linear. Therefore, it could be assumed that the FUT does not preserve OAM mode due to disturbed circular polarisation.

To conclude, in this chapter was performed the detailed characterisation of the 19-cell HC PBGF by the spectrogram approach of the S^2 method. The measurement revealed that within a low loss bandwidth, except LP_{01}, also propagate two modes: LP_{11} and LP_{02} . It should be emphasized, that LP_{11} modes are present in the spectrogram as narrow discrete trails, while LP_{02} is distributed over a large range of time delays. According to the loss measurement at wavelength longer than 1565nm the FM attenuates, which makes an analysis of the FUT by the S^2 method complicated. It was discovered, that LP_{02} becomes a dominant mode instead of the FM after 1573nm and all discrete trails at longer wavelength disappear and the spectrogram reveal only a continuum of distributed modes. Also was discovered an influence of the surface modes on the propagating mode noticed in reconstructed profiles of some modes within a high loss bandwidth. According to the spectrogram and simulation of the vectorial modes, that compose the LP_{11} group, at wavelength of 1550nm TM_{01} is separated in time delay from TE_{01} and HE_{21}, whose are crossing each other at the aforementioned wavelength. Similar tendency is observed for the measured S^2 trace at 1550nm, where independent on the input polarisation present only two LP_{11}. An investigated dependence of the excited LP_{11} modes on the state of input polarisation revealed a clear correlation in polarisation orientations of two LP_{11} modes, while

two other were unresolvable and did not preserve a clear polarisation dependency. Therefore, it was assumed that the non-degenerate TE_{01} and TM_{01} modes are hardly separated from $HE_{21}^{o,e}$ and might prevent formation of the ± 1 OAM modes in the 19-cell HC PBGF. The similar results were obtained for measurements performed by the ToF technique. For ± 1 OAM modes in the ToF trace were present an additional shoulder peak, time delays of which corresponded to numerically calculated time delays of TE_{01} and TM_{01}. Simultaneously, back conversion of the coupled into the FUT OAM modes was not efficient.

Therefore, it can be concluded that support of OAM modes by 325m of the 19-cell HC PBGF is doubtful. However, in the case of a HC PBGF with a larger diameter of air core, for example 37-cell, where larger amount of HOMs can be supported over a broad low loss transmission bandwidth, propagation of higher orders of OAM modes could be still possible.

Chapter 6

Conclusions

This chapter presents final conclusions concerning the research performed in this thesis and provides an outlook for further possible investigations. The thesis can be divided into the following parts: the first part presents a detailed investigation of the C^2 imaging technique and its implementation for different types of fibres (a step index and polarisation maintaining fibres, DMF rod fibre, hollow core photonic crystal fibre and hollow core bandgap fibre); the second part presents a modelling of the 19-cell HC PBGF with anti-resonant elements and the experimental characterisation of its modal properties by the S^2 imaging with the spectrogram approach; the last part demonstrates the excitation of OAM modes in the 19-cell HC PBGF and explains challenges met during the back conversion of OAM modes at demultiplexing.

An experimental characterisation of the fibre modal content is one of the main topics in this thesis with the C^2 and S^2 imaging techniques in the focus. By investigating principles of the interferometric-based approach for the modal content detection, it was also demonstrated, that simply evaluating the visibility of the interference between two beams, general properties of the propagating fibre modes can be derived. The visibility itself is proportional to the cross-correlated function and can be

measured as a modulation depth of interference. Despite of determining a quantity of the modes and their differential time delays, a correlation between a relative modal power and amplitude of a peak at the visibility trace has to be investigated as well as more precise procedure for the visibility measurement.

The original C^2 method in the time domain implemented with a tunable and flexible light source is a valuable diagnostic tool for the fibre mode characterisation with a spectrogram approach, since it has an additional degree of the flexibility to control not only the spectral width, but also the spectral shape of the seed source. The method is a beneficial for the fibres of either common or advanced designs. In the case of the flexible C^2 approach, attention had to be paid to the shaping of the spectrum around the pump wavelength of 1064nm. Nevertheless, the temporal resolution of the C^2 trace at 1064nm is affected in a slight degree by the presence of the pump peak at the input spectrum, as it was observed for the DMF rod fibre measurement, it is still possible to eliminate its influence by a careful choice of the wavelength channels and their powers.

It should be mentioned as well, that a type of the imaging technique has to be chosen depending on the measurement requirements and opportunities. Comparing the C^2 and S^2 imaging, advantages and disadvantages of both techniques were clear. The S^2 is worth to implement for long pieces of fibre with a distinct dominant mode. When aforesaid conditions are fulfilled, the S^2 is reliable and extremely sensitive technique. On the other hand, the C^2 is not restricted by the same conditions. It can easily detect modes of the same power in a short piece of a fibre. However, the fibre under test has to be balanced by a reference fibre with the same dispersion properties. In that case, high temporal resolution can be reached within a definite range of the spectral bandwidths. The highest temporal resolution, for example, was achieved for the HC PCF balanced by the same type of fibre coiled to a defined diameter to eliminate all

HOMs. However, it was challenging to find an appropriate reference fibre for the 19-cell HC PBGF. The characterisation was performed by the modified version of the S^2 method, that experienced difficulties of the modal content detection within a high loss bandwidth of wavelengths due to the weak fundamental mode and strong higher-order modes.

For the 19-cell HC PBGF not only its experimental characterisation is challenging. Theoretical modelling of this fibre type requires an extra attention paid to the choice of modelling parameters. A good agreement within a narrow wavelength range was achieved for experimental results and a simulation based on a SEM image of the fibre. However, due to a charge accumulated at the silica surface, a quality of the SEM image is reduced and geometrical parameters for the model were chosen based on averaged measures. At the same time, some defects at the air-glass interface, like for example, a surface roughness, are so small that they cannot be revealed in the SEM image bringing a disagreement between the simulated and measured results. Aforementioned features make modelling of HC PBGF challenging.

In the concluding part of the thesis an investigation of the OAM modes propagation in the 19-cell HC PBGF was performed. This type of modes already attracted a tremendous attention as a possible carriers of information in a MDM system. Also a couple of paper were published with a prediction of OAM modes confinement within a HC PBGF. According to the results of simulation, in the 19-cell HC PBGF with anti-resonant elements would be also possible to propagate the OAM mode of the first order. However, spending a fair amount of time on an attempt to multiplex and demultiplex the OAM modes, that were coupled to the fibre, based on the experimental results it was concluded that the OAM modes propagation in 325m of the 19-cell HC PBGF is doubtful.

As a future investigation may be considered the excitation and propagation of OAM modes in a short piece of the 19-cell HC PBGF with a more careful polarisation control. Also a characterisation of HC PBGF

with a larger core diameter can be studied as well. Since for a HC PBGF with a broad bandgap range, that could support a larger number of modes with low modal dependent losses, the excitation of the higher orders of OAM modes could be realistic.

Appendix A

COMSOL Multiphysics for numerical modelling of a fibre

COMSOL Multiphysics is the commercial software-platform implemented by engineers for modelling of physics-based problems [18]. Simulation are provided based on a set of partial differential equations (PDE), that are solved by the finite-element method (FEM). COMSOL has an user-friendly graphic interface with a number of physics modelling functionalities. Usually, the problem is defined by establishing the physics and study, setting up geometry and materials properties,defining subdomains and boundary conditions, meshing the geometry and running studying. COMSOL can be integrated with Matlab, allowing to run the whole simulation in Matlab or to post process the results of simulation by exporting all data from COMSOL to Matlab.

The COMSOL Electromagnetic Waves interface is used to solve for time-harmonic electromagnetic field distributions. For this physics interface, the geometry is divided into a large number of meshing elements, the maximum size of which is limited to a fraction of a wavelength. The COMSOL solves the wave equation, briefly discussed in Section 2.2 for a specified cross-section of the fibre. To reduce the calculation time,

taking into account the circular symmetry of the fiber, the structure can be divided into quarter domains with implementation of the boundary conditions as the perfect electric and perfect magnetic contour, and perfectly match layer (PML) for non-reflecting boundaries. The study type "Mode Analysis" computes the propagation constants of all propagating modes in a fibre at the given wavelength around chosen value of refractive index. As result of modelling, one gets the full vectorial field distributions of all modal at given wavelength as well as the propagation constant for each mode.

At the post processing stage all fields and the main parameters, as the effective refractive indices, modal areas and fractional power of the guided modes are exported to Matlab. To simulate a fibre along a range of wavelengths the simulation were controlled by Matlab repeating the whole procedure at each wavelength along the required wavelength range.

Appendix B

List of abbreviations

C^2 Cross-correlated imaging

CL Confinement loss

DMF Distributed modal filtering

DTD Differential time delay

FM Fundamental mode

FUT Fibre under test

HC Hollow core

HOM Higher order mode

HWP Half wave plate

LM Leaky mode

LMA Large mode area

LPG long period grating

MDM Mode division multiplexing

MM Multi mode

MPI Multi path interference

MZI Mach-Zehnder interferometer

OAM Orbital angular momentum

OPD Optical path difference

OPL Optical path length

OSA Optical spectrum analyser

PCF Photonic crystal fibre

PM Polarization maintaining

S^2 Spatially and spectrally resolved imaging

SL Scattering loss

SLM Spatial light modulator

SM Single mode

SMF Single mode fibre

SMs Surface modes

ToF Time-of-Flight

QWP Quarter wave plate

References

[1] K.Z. Aghaie, V. Dangui, M. J. F. Digonnet, S. Fan, and G.S. Kino. Classification of the core modes of hollow-core photonic-bandgap fibers. *IEEE Journal of Quantum Electronics*, 45(9):1192–1200, 2009.

[2] G. P. Agrawal. *Fiber-Optic Communications Systems, Third Edition.* Wiley, New York City, 2002.

[3] M. M. Ali, Y. Jung, K. S. Lim, M. R. Islam, S. U. Alam, D. J. Richardson, and H. Ahmad. Characterization of mode coupling in few-mode FBG with selective mode excitation. *IEEE Photonics Technologe Letters*, 27(16):1713—-1716, 2015.

[4] T. T. Alkeskjold, M. Laurila, L. Scolari, and J. Broeng. Single-mode ytterbium-doped large-mode-area photonic bandgap rod fiber amplifier. *Optics express*, 19(8):7398–7409, 2011.

[5] L. Allen, M. W. Beijersbergen, R. J. C. Spreeuw, and J. P. Woerdman. Orbital angular momentum of light and the transformation of Laguerre-Gaussian laser modes. *Physical Review A*, 45(11): 8185–8189, 1992.

[6] R. Amezcua-Correa, N. G. R. Broderick, M. N. Petrovich, F. Poletti, and D. J. Richardson. Optimizing the usable bandwidth and loss through core design in realistic hollow-core photonic bandgap fibers. *Optics Express*, 14(17):7974–7985, 2006.

[7] R. Barankov. Cross-correlation imaging for waveguide characterization. Master's thesis, Boston University, 2012.

[8] R. Beth. Mechanical detection and measurement of the angular momentum of light. *Physical Review A*, 50:115—-125, 1936.

[9] T. A. Birks, J. C. Knight, and P. St. J. Russell. Endlessly single-mode photonic crystal fiber. *Optics Letters*, 22(13):961–963, 1997.

[10] P. Biswas, N. Basumallick, K. Dasgupta, and S. Bandyopadhyay. Response of strongly over-coupled resonant mode of a long period grating to high refractive index ambiance. *Journal of Lightwave Technology*, 32(11):2072–2078, 2014.

[11] J. N. Blake, B. Y. Kim, , and H. J. Shaw Edward. Fiber-optic modal coupler using periodic microbending. *Optics Letters*, 11 (3):177–179, 1986.

[12] M. Born and E. Wolf. *Principles of Optics, 7th ed.* Cambridge University Press, New York, 1999.

[13] N. Bozinovic, Y. Yue, Y. Ren, M. Tur, P.Kristensen, H. Huang, A.E. Willner, and S.Ramachandran. Terabit-scale orbital angular momentum mode division multiplexing in fibers. *Science*, 340: 1545–1548, 2013.

[14] F. Cardano, E. Karimi, L. Marrucci, C. de Lisio, and E. Santamato. Generation and dynamics of optical beams with polarization singularities. *Optics Express*, 21(7):8815–8820, 2013.

[15] J. Carpenter and T. D. Wilkinson. Characterization of multimode fiber by selective mode excitation. *Journal of Lightwave Technology*, 30(10):1386–1392, 2012.

[16] J. Carpenter, B.J. Eggleton, and J.Schröder. Polarization-resolved cross-correlated (C2) imaging of a photonic bandgap fiber. *Optics Express*, 24(24):27785–27790, 2016.

[17] H. Chen, R. G. H. Van Uden, C. M. Okonkwo, Yongmin Jung, N. V. Wheeler, E. N. Fokoua, N. Baddela, M. N. Petrovich, F. Poletti, D. J. Richardson, O. Raz, H. De Waardt, and A. M. J. Koonen. Mode division multiplexing over 19-cell hollow-core photonic bandgap fibre by employing integrated mode multiplexer. *Electron. Lett.*, 50(17):1227–1229, August 2014.

[18] COMSOL. COMSOL Multiphysics. https://www.comsol.dk/comsol-multiphysics/, 2017. [Online; accessed 17-October-2017].

[19] Corning. SMF-28. https://www.corning.com/in/en/products/communication-networks/products/fiber/smf-28-ultra.html/, 2017. [Online; accessed 19-October-2017].

[20] J. Demas and S. Ramachandran. Sub-second mode measurement of fibers using C2 imaging. *Optics Express*, 22(19):23043–23056, 2014.

[21] A. D. Ellis, J. Zhao, and D. Cotter. Approaching the non-linear Shannon limit. *Journal of Lightwave Technology*, 28:423–433, 2010.

[22] T. Erdogan. Fiber grating spectra. *Journal of Lightwave Technology*, 15(8):1277–1294, 1997.

[23] R.J. Essiambre, G. Kramer, P.J. Winzer, G.J. Foschini, and B. Goebel. Capacity limits of optical fiber networks. *Journal of Lightwave Technology*, 28(4):662–701, 2010.

[24] D. Flamm, C. Schulze, D. Naidoo, S. Schröter, A. Forbes, and M. Duparré. All-digital holographic tool for mode excitation and analysis in optical fibers. *Journal of Lightwave Technology*, 31 (7):1023–1032, 2013.

[25] E. N. Fokoua, F. Poletti, and D. J. Richardson. Analysis of light scattering from surface roughness in hollow-core photonic bandgap fiber. *Optics Express*, 20(19):3783–3789, 2012.

[26] E. N. Fokoua, S. R. Sandoghchi, T. Jasion Y. Chen, N. V. Wheeler, N. K. Baddela, J. R. Hayes, M. N. Petrovich, D. J. Richardson, and F. Poletti. Accurate modelling of fabricated hollow-core photonic bandgap fibers. *Optics Express*, 23(18):20980–20991, 2015. URL https://doi.org/10.1364/OE.23.023117.

[27] N.K. Fontaine, R. Ryf, H. Chen, A. V. Benitez, J.E. Antonio Lopez, R. Amezcua Correa, B. Guan, B. Ercan, R.P. Scott, S.J. Ben Yoo, L.G. Nielsen, Yi Sun, and R. J. Lingle. 30x30 MIMO transmission over 15 spatial modes. In *Optical Fiber Communication Conference,OSA Technical Digest*, page Th5C.1, 2015.

[28] D. Franzen. Determining the effective cutoff wavelength of single-mode fibers: An interlaboratory comparison. *Journal of Lightwave Technology*, 3(1):128–134, 1985.

[29] T. Fricke-Begemann and J. Burke. Speckle interferometry: three-dimensional deformation field measurement with a single interferogram. *Applied optics*, 40(28):5011–5022, 2001.

[30] Y. Fu, G. Pedrini, and W. Osten. Vibration measurement by temporal Fourier analyses of a digital hologram sequence. *Applied optics*, 46(23):5719–5727, 2007.

[31] A. Ghatak and K. Thyagarajan. *An Introduction to Fiber Optics*. Cambridge University Press, Cambridge, 1998.

[32] D. Gloge. Weakly guiding fibers. *Applied Optics*, 10(10):2252–2258, 1971.

[33] S. E. Golowich and S. Ramachandran. Impact of fiber design on polarization dependence in microbend gratings. *Optics Express*, 13(18):6870–6877, 2005.

[34] W. Göpel, J. Hesse, and J.N. Zemel. *Sensors*. VCH, Weinheim, Germany, 1992.

[35] D.R. Gray, M.N. Petrovich, S.R. Sandoghchi, N.V. Wheeler, N.K. Baddela, G.T. Jasion, T. Bradley, D.J. Richardson, and F. Poletti. Real-time modal analysis via wavelength-swept spatial and spectral (S2) imaging. *IEEE Photonics Technology*, 28(9):1034–1037, 2016.

[36] P. Gregg, P. Kristensen, and S. Ramachandran. Conservation of orbital angular momentum in air-core optical fibers. *Optica*, 2(3): 267—-270, 2015.

[37] P. Gregg, M. Mirhosseini, A. Rubano, L. Marrucci, E. Karimi, R. W. Boyd, and S. Ramachandran. Q-plates as higher order polarization controllers for orbital angular momentum modes of fiber. *Optics Letters*, 40(8):1729–1732, 2015.

[38] P. Gregg, P.Kristensen, and S. Ramachandran. 13.4km OAM state propagation by recirculating fiber loop. *Optics Epress*, 24(17): 879–888, 2016.

[39] J.C. Guo, Y.S. Yu, X.L. Zhang, C. Chen, R. Yang, C. Wang, R.Z. Yang, Q.D. Chen, and H.B. Sun. Compact long-period fiber gratings with resonance at second-order diffraction. *IEEE Photonics Technology Letters*, 24(16):1393–1395, 2012.

[40] R. Guobin, W. Zhi, L. Shuqin, and J. Shuisheng. Mode classification and degeneracy in photonic crystal fibers. *Optics Express*, 11 (11):1310–1321, 2003.

[41] D. P. Hand and P. St. J. Russell. Photoinduced refractive-index changes in germanosilicate fibers. *Optics Letters*, 15(2):102–104, 1990.

[42] M. Hipp, J. Woisetschlager, P. Reiterer, and T. Neger. Digital evaluation of interferograms. *Measurement*, 36(1):53–66, 2004.

[43] K. Ingerslev, P. Gregg, M. Galili, F. Da Ros, H. Hu, F. Bao, M.A. Usuga Castaneda, P.Kristensen, A. Rubano, L. Marrucci, S. Ramachandran, K.Rottwitt, T. Morioka, and L. Katsuo Oxenløwe. 12 mode, MIMO-free OAM transmission. In *Proceedings of Optical Fiber Communication Conference*, page M2D.1, 2017.

[44] E. Ip, M.-J. Li, K. Bennett, Y.-K. Huang, A. Tanaka, A. Korolev, K. Koreshkov, W. Wood, E. Mateo, J. Hu, and Y. Yano. 146λx6x19-Gbaud wavelength- and mode-division multiplexed transmission over 10x50-km spans of few-mode fiber with a gain-equalized few-mode EDFA. In *Optical Fiber Communication Conference/National Fiber Optic Engineers Conference 2013*, page PDP5A.2, 2013.

[45] S.W. James and R. P. Tatam. Optical fibre long-period grating sensors: characteristics and application. *Measurement science and technology*, 14(5):R49, 2003.

[46] J. Jasapara and A. D. Yablon. Spectrogram approach to S2 fiber mode analysis to distinguish between dispersion and distributed scattering. *Optics Letters*, 37(18):3906–3908, 2012.

[47] C. Jauregui, J. Limpert, and A. Tünnermann. High-power fibre lasers. *Nature Photonics*, 7(11):861–867, 2013.

[48] M. M. Jørgensen, S. Rübner Petersen, M. Laurila, J. Lægsgaard, and T. T. Alkeskjold. Optimizing single mode robustness of the distributed modal filtering rod fiber amplifier. *Optics express*, 20 (7):7263–7263, 2012.

[49] I. Kaminow, T. Li, and A. E. Willner. *Optical Fiber Telecommunications (Sixth Edition). Systems and Networks*. Elsevier, Amsterdam, 2013.

[50] Y. Kawaguchi, Y. Tamura, T. Haruna, Y. Yamamoto, and M. Hirano. Ultra low-loss pure silica core fiber. *SEI TECHNICAL REVIEW*, 80:50–55, 2015.

[51] F. Kong, G. Gu, T. W. Hawkin, J. Parsons, M. Jones, and C. Dunn. Quantitative mode quality characterization of fibers with extremely large mode areas by matched white-light interferometry. *Optics Express*, 22(12):14657–14665, 2014.

[52] M. Laurila, R. Barankov, M. M. Jørgensen, T. T. Alkeskjold, J. Broeng, J. Lægsgaard, and S. Ramachandran. Cross-correlated imaging of single-mode photonic crystal rod fiber with distributed mode filtering. *Optics Express*, 21(8):9215–9229, 2013.

[53] K. S. Lee and T. Erdogan. Transmissive tilted gratings for LP -to-LP mode coupling. *IEEE Photonics Technology Letters*, 10 (11):1286–1288, 1999.

[54] H. Li, G. Ren, Y. Lian, B. Zhu, M. Tang, Y. Zhao, and S. Jian. Broadband orbital angular momentum transmission using a hollow-core photonic bandgap fiber. *Optics Letters*, 41(15):3591–3594, 2016.

[55] H. Li, G. Ren, Y. Gao, B. Zhu, J. Wang, B. Yin, and S. Jian. Hollow-core photonic bandgap fibers for orbital angular momentum applications. *Journal of Optics*, 19(4):045704–10, 2017.

[56] H. Li, G. Ren, B. Zhu, Y. Gao, B. Yin, J. Wang, and S. Jian. Guiding terahertz orbital angular momentum beams in multimode kagome hollow-core fibers. *Optics Letters*, 42(2):179–182, 2017.

[57] N. M. Litchinitser, A. K. Abeeluck, C. Headley, and B. J. Eggleton. Antiresonant reflecting photonic crystal optical waveguides. *Opt. Lett*, 29:1592–1594, 2002.

[58] C. Liu, F. Wang, J. Lv, T. Sun, Q. Liu, H. Mu, and P. K. Chu. Design and theoretical analysis of a photonic crystal fiber based on surface plasmon resonance sensing. *Journal of Nanophotonics*, 9:093050–1–093050–10, 2015.

[59] M. Michieletto. *Hollow core fibers for high power laser applications*. PhD thesis, Technical University of Denmark, 2016.

[60] M. Michieletto, J. K. Lyngsø, C. Jakobsen, J. Lægsgaard, O. Bang, and T. T. Alkeskjold. Hollow-core fibers for high power pulse delivery. *optics Epress*, 24(7):7103–7119, 2016.

[61] F. Mitschke. *Fiber Optics. Physics and Technology*. Springer, Berlin, Heidelberg, 2010.

[62] N. A. Mortensen and M. D. Nielsen. Modeling of realistic cladding structures for air-core photonic band- gap fibers. *Amer. Math. Soc. Transl. (2)*, 29:349–351, 2004.

[63] S. Nakadate and H. Saito. Fringe scanning speckle-pattern interferometry. *Applied optics*, 24(14):2172–2180, 1985.

[64] R. M. Nejad, K. Allahverdyan, P. Vaity, S. Amiralizadeh, C. Brunet, Y. Messaddeq, S. LaRochelle, and L. A. Rusch. Mode division multiplexing using orbital angular momentum modes over 1.4 km ring core fiber. *Journal of Lightwave Technology*, 24 (18):4252–4258, 2016.

[65] J.W. Nicholson, A. D.Yablon, S. Ramachandran, and S. Ghalmi. Spatially and spectrally resolved imaging of modal content in large-mode-area fibers. *Optics Express*, 16(10):7233—7243, 2008.

[66] J.W. Nicholson, L. Meng, J.M. Fini, R.S. Windeler, A. DeSantolo, E. Monberg, F. DiMarcello, Y. Dulashko, M. Hassan, , and R. Ortiz. Measuring higher-order modes in a low-loss, hollow-core, photonic-bandgap fiber. *Optics Express*, 20(18):61–70, 2012.

[67] Nufern. 780-hp. http://www.nufern.com/pam/optical_fibers/883/780-HP/, 2017. [Online; accessed 19-October-2017].

[68] Nufern. 980-hp. http://www.nufern.com/pam/optical_fibers/884/980-HP/, 2017. [Online; accessed 30-October-2017].

[69] K. Okamoto. *Fundamentals of Optical Waveguides , 2nd ed.* Academic Press, Cambridge, 2010.

[70] G. Pedrini, I. Alexeenko, W. Osten, and H. J. Tiziani. Temporal phase unwrapping of digital hologram sequences. *Applied optics*, 42(29):5846–5854, 2003.

[71] NKT Photonics. SuperK SELECT multi-line tunable filter. http://www.nktphotonics.com/lasers-fibers/en/product/superk-select-multi-line-tunable-filter/, 2017. [Online; accessed 24-October-2017].

[72] NKT Photonics. Supercontinuum generation. http://www.nktphotonics.com/lasers-fibers/en/technology/supercontinuum/, 2017. [Online; accessed 24-October-2017].

[73] NKT Photonics. SuperK EXTREME supercontinuum lasers. http://www.nktphotonics.com/lasers-fibers/en/product/superk-extreme-supercontinuum-lasers/, 2017. [Online; accessed 24-October-2017].

[74] NKT Photonics. AeroGAIN ROD. http://www.nktphotonics.com/lasers-fibers/en/product/aerogain-rod-high-power-ytterbium-rod-fiber-gain-modules/, 2017. [Online; accessed 06-November-2017].

[75] J. Plucinski, R. Hypszer, P. Wierzba, M. Strakowski, M. Jedrzejewska-Szczerska, M. Maciejewski, and B. B. Kosmowski. Optical low-coherence interferometry for selected technical applications. *Bulletin of the Polish Academy of Sciences Technical Sciences*, 56(2):155–172, 2008.

[76] PointGray. FL3-GE-03S1M-C. https://www.ptgrey.com/support/downloads/10109/, 2017. [Online; accessed 20-November-2017].

[77] F. Poletti. Hollow-core photonic bandgap fibers: technology and applications. *Nanophotonics*, 2:315–340, 2013.

[78] J.H. Poynting. The wave motion of a revolving shaft, and a suggestion as to the angular momentum in a beam of circularly polarised light. *Proceedings of the Royal Society of London. Series A,*, 82:560—-567, 1909.

[79] S. Ramachandra. *Fiber Based Dispersion Compensation*. Springer, New York, 2007.

[80] S. Ramachandran and P. Kristensen. Optical vortices in fiber. *Nanophotonics*, 2(5-6):455–474, 2013.

[81] S. Ramachandran, J. M. Fini, M. Mermelstein, J. W. Nicholson, S. Ghalmi, and M. F. Yan. Ultra-large effective-area, higher-order mode fibers: a new strategy for high-power lasers. *Laser and Photonics Reviews*, 2(6):429–448, 2008.

[82] D. J. Richardson, J. Nilsson, and W. A. Clarkson. High power fiber lasers: current status and future perspectives [invited]. *Journal of the Optical Society of America B*, 27(11):B63–B92, 2010.

[83] D. J. Richardson, J. M. Fini, and L. E. Nelson. Space-division multiplexing in optical fibres. *Nature Photonics*, 7:354–362, 2013.

[84] P. J. Roberts, F. Couny, H. Sabert, B. J. Mangan, D. P. Williams, L. Farr, M. W. Mason, and A. Tomlinson. Ultimate low loss of hollow-core photonic crystal fibres. *Optics Express*, 13(1): 236–244, 2005.

[85] P. J. Roberts1, D. P. Williams, B. J. Mangan, H. Sabert, F. Couny, W. J. Wadsworth, T. A. Birks, J. C. Knight, and P. St.J. Russell. Realizing low loss air core photonic crystal fibers by exploiting an antiresonant core surround. *Optics Express*, 13(20):8277–8285, 2005.

[86] P. J. Roberts1, D. P. Williams, H. Sabert, B. J. Mangan1, D. M. Bird, T. A. Birks, J. C. Knight, and P. St. J. Russell. Design of low-loss and highly birefringent hollow-core photonic crystal fiber. *Optics Express*, 14(16):1457–1467, 2006.

[87] P. St. J. Russell. Photonic-crystal fibers. *Journal of Lightwave Technology*, 24(12):4729–4749, 2006.

[88] R. Ryf, N.K. Fontaine, M.A. Mestre, S. Randel, X. Palou, C. Bolle, A.H. Gnauck, S. Chandrasekhar, X. Liu, B. Guan, R.J. Essiambre, P. Winzer S.G. Leon-Saval, J. Bland-Hawthorn, R. Delbue, P. Pupalaikis, A. Sureka, Y. Sun, L. Grüner-Nielsen, R.V. Jensen, and R. Lingle. 12×12 MIMO transmission over 130-km few-mode fiber. In *Frontiers in Optics, FIO 2012*, page FW6C.4, 2012.

[89] R. Ryf, S. Randel, A. H. Gnauck, C. Bolle, A. Sierra, S. Mumtaz, M. Esmaeelpour, E. C. Burrows, R.-J. Essiambre, P. J.Winzer, D.W. Peckham, A. H. McCurdy, and R. Lingle. Mode-division multiplexing over 96 km of few-mode fiber using coherent 6x6 MIMO processing. *Journal of Lightwave Technology*, 30(4): 521–531, 2012.

[90] K. Saitoh and M. Koshiba. Leakage loss and group velocity dispersion in air-core photonic bandgap fibers. *Optics Express*, 11 (23):3100–3109, 2003.

[91] B. E. A. Saleh and M. C. Teich. *Fundamentals of Photonics*. Wiley, New York, 2007.

[92] S. Savin, M.J. F. Digonnet, G.S. Kino, and H.J. Shaw. Tunable mechanically induced long-period fiber gratings. *Optics Letters*, 25(10):710–712, 2000.

[93] D. N. Schimpf, R. Barankov, and S. Ramachandran. Cross-correlated (C2) imaging of fiber and waveguide modes. *Optics Express*, 19(14):13008–13019, 2011.

[94] M. Secondini and E. Forestieri. Scope and limitations of the nonlinear Shannon limit. *Journal of Lightwave Technology*, 35 (4):893–902, 2017.

[95] V.A.J.M. Sleiffer, Y. Jung, N.K. Baddela, J.Surof, M.Kuschnerov, V. Veljanovski, J. R. Hayes, N.V. Wheeler, E. R. N. Fokoua, J. P. Wooler, D. R. Gray, N.H.L. Wong, F. R. Parmigiani, S.U. Alam, M. N. Petrovich, F. Poletti, D.J. Richardson, and H. De Waardt. High capacity mode-division multiplexed optical transmission in a novel 37-cell hollow-core photonic bandgap fiber. *J. Lightwave Techol.*, 32(4):854–863, February 2014.

[96] S. Slussarenko, A. Murauski, T. Du, V. Chigrinov, L. Marrucci, and E. Santamato. Tunable liquid crystal Q-plates with arbitrary topological charge. *Optics Letters*, 19(5):4085–4090, 2011.

[97] C.M. Smith, N. Venkataraman, M.T. Gallagher, D. Müller, J.A. West, N.F. Borrelli, D.C. Allan, and K.W. Koch. Low-loss hollow-core silica / air photonic bandgap fibre. *Nature*, 424:657–659, 2003.

[98] E. Snitzer, H. Po, F. Hakimi, R. Tumminelli, and B.C. McCollum. Double clad, offset core Nd fibre laser. In *OSA Technical Digest Series, Optical Fiber Sensors*, page PD5, 1988.

[99] A. W. Snyder. Asymptotic expressions eigenvalues optical of a dielectric or optical waveguide. *IEEE Transactions of Microwave Theory and Techniques*, MIT-17(12):1130–1138, 1969.

[100] G. Stepniak, L. Maksymiuk, and J. Siuzdak. Binary-phase spatial light filters for mode-selective excitation of multimode fibers. *Journal of Lightwave Technology*, 29(13):1980–1987, 2011.

[101] M. Takeda, H. Ina, and S. Kobayashi. Fourier-transform method of fringe-pattern analysis for computer-based topography and interferometry. *Journal of the Optical Society of America B*, 72 (1):156–160, 1982.

[102] T.Grosjean, A.Sabac, and D.Courjon. A versatile and stable device allowing the efficient generation of beams with radial, azimuthal or hybrid polarizations. *Optics Communications*, 252(1-3):12–21, 2005.

[103] Thorlabs. Q-plate. https://www.thorlabs.com/newgrouppage9.cfm?objectgroup_ID=9098/, 2017. [Online; accessed 13-November-2017].

[104] W. Q. Thornburg, B. J. Corrado, and X. D. Zhu. Selective launching of higher-order modes into an optical fiber with an optical phase shifter. *Optics Letters*, 19(7):454–456, 1994.

[105] J. van Howe, J. H. Lee, S. Zhou, F. Wise, C. Xu, S. Ramachandran, S. Ghalmi, and M. F. Yan. Demonstration of soliton self-frequency shift below 1300nm in higher-order mode, solid silica-based fiber. *Optics Letters*, 32(4):340–342, 2007.

[106] A.M. Vengsarkar, P.L. Lemaire, J.B. Judkins, V. Bhatia, T. Erdogan, and J.E. Sipe. Long-period fiber gratings as band-rejection filter. *Journal of Lightwave Technology*, 14(1):58–65, 1996.

[107] J. A. West, C. M. Smith, N. F. Borrelli, D. C. Allan, and K. W. Koch. Surface modes in air-core photonic band-gap fiber. *Optics Express*, 12(8):1485—-1496, 2004.

[108] J. Wildea, C. Schulzea, R. Brüninga, M. Duparréa, and S. Schröter. Selective higher order fiber mode excitation using a monolithic setup of a phase plate at a fiber facet. In *SPIE Proceedings Vol. 9343: Laser Resonators, Microresonators, and Beam Control XVII*, 2015.

[109] Xenics. Xeva-1.7-320. http://www.xenics.com/en/xeva-17-320-0/, 2017. [Online; accessed 06-November-2017].

[110] J. Xu, J. K. Lyngsø, L. Leick, J. Carpenter, T. D. Wilkinson, and C. Peucheret. Mode division multiplexing exploring hollow-core photonic bandgap fibers. In *15th International Conference on Transparent Optical Networks*, page We.B6.2, 2013.

[111] R.C. Youngquist, J.L. Brooks, and H.J. Shaw. Two-mode fiber modal coupler. *Optics Letters*, 9(5):177–179, 1984.

[112] Y. Zhao, Y. Liu, L. Zhang, C. Zhang, J. Wen, and T. Wang. Mode converter based on the long-period fiber gratings written in the two-mode fiber. *Optics letters*, 24(6):6186–6195, 2016.